## *X-ray scattering in giant magneto-resistive multilayers*

Fulthorpe, Brian David

# X-ray Scattering in Giant Magneto-Resistive Multilayers

*by*

**Brian David Fulthorpe**



A thesis submitted in partial fulfilment of the requirements for the degree of Doctor of Philosophy

The University of Durham

1999

# Abstract

The scattering mechanisms responsible for Giant Magneto-Resistance (GMR) in magnetic multilayers are believed to be related to many aspects of the multilayer structure. X-ray scattering techniques provide a powerful method with which to study the bulk and interface morphology in these systems, and are therefore crucial in developing an understanding of the dominant factors influencing the magnitude of the GMR.

Reflectivity measurements performed on a series of Co/Cu multilayers, sputter deposited onto etched silicon, reveal no variation in the interface roughness with etching voltage, the thickness of the individual layers also remaining constant. The observed decrease in the GMR cannot, therefore, be attributed to variations in spacer thickness or interfacial spin-independent scattering. Electron and X-ray Diffraction measurements suggest the reduction in GMR is due to a loss of antiferromagnetic coupling associated with a transformation of the texture from a randomly oriented to well oriented (111) polycrystalline texture, and subsequent reduction in the volume fraction of (100) oriented grains.

Interfaces within Co/Cu are found to propagate with a high degree of conformality with increasing bilayer number, with an out-of-plane correlation length well in excess of 300Å. In contrast, the Co/Pt system exhibits a limiting out-of-plane correlation length of the order of 350Å arising from a columnar growth mode.

X-ray Reflectivity and Diffraction measurements provide no structural interpretation for the 3-fold enhancement in the rate of increase of the saturation conductivity, as a function of spacer thickness, in Fe/Au (100) compared to Fe/Au (111), or why large oscillations in the GMR occur for the (100) orientation only. Such observations are, however, consistent with the existence of a channelling mechanism in Fe/Au (100). Grazing Incidence Fluorescence data indicates that Nb acts as a surfactant in Fe/Au (111) growth on sapphire. The influence of different defect types within multilayers has also been observed.

# Acknowledgements

I would like to take this opportunity to thank all of the people without whom the past three years would not have been possible and would certainly not have been as enjoyable.

Firstly, my deepest thanks to Prof. B.K. Tanner for his continual guidance, encouragement and enthusiasm throughout the course of my studies and for the provision of such excellent facilities and support within the department.

The very nature and scale of the work presented in this study has lead to much of it being performed as part of collaborative ventures with other research groups. I would like to thank Prof. P.J. Grundy, University of Salford and Dr. B.J. Hickey, University of Leeds, and their respective research groups for providing the samples and magneto-transport data relating to the work presented in this thesis. My thanks go to David Joyce, Paul Ryan and David Dekadjevi not only for their help and useful discussions but also for providing many amusing memories from all over the world.

It would not have been possible to obtain any of the data presented here had it not been for the dedication and assistance of the staff at the various Synchrotron sources. I would like to thank Dr. Chiu Tang and Dr. Steve Collins at the Daresbury SRS, Dr. Andy Fitch and Dr. Gavin Vaughan on BM16, ESRF and Dr. Simon Brown and Paul Thompson for the long hours on the XMaS CRG Beamline, ESRF. I must also thank Bede Scientific Instruments Ltd and more specifically Matt Wormington for providing the simulation code used to analyse the majority of the data in this thesis.

I would like to thank the many members of the department who have assisted in various ways during the past three years. Thanks go to Mike Lee, Vicki Greener and Pauline Russell in the audio-visual department and to the secretarial staff, Penny Carse, Rebecca Siddle, Joanne Pallister, Julie Bell and Claire Davies. Also, thanks to Wayne

Dobby for making a demonstrators life a lot easier. Thanks also to Pat the tea lady for still speaking to me when I defected to the vending machine.

I have been lucky enough to have had the opportunity to work with and alongside numerous people over the last 3 years, all of whom have contributed to making the whole experience rewarding and above all else enjoyable. Firstly, my thanks to the x-ray group past, present and future: John Clarke, Tom Hase, Ian Pape, Stuart Wilkins, Andrea (No.1) Li Bassi, Andrea (No. 2) Amici, Amir Rozatian, Luo Guangming, Dr. Peter Hatton, Yixi Su, Caroline Moore, Marco Poli, Sujit Halder, Peter Normile, Rachael Pickford, Tom Moore. Also the greater condensed matter group and beyond: Dan Read, Gwyn Ashcroft, Nigel Leigh, Adrian Sneary, Simon Keys, Nancy-Ann Hackman, Stuart Dailey, Paul Laughlin, Chris Leighton, Alton Horsfall, Ian Daniel, Candid Reig, Nikki Bingham, Dr. Damian Hampshire, Dr. Ian Terry and finally, for his guidance on the art of tactfulness and all things politically incorrect, John Dobson.

I would like to express my thanks to my family for their continual support (not to mention a roof! ) over the years, without which this would not have been possible.

# Publications

The following publications relate to work presented in this thesis:

**Chapter 5**

*Crystallographic texture and interface structure in Co/Cu multilayer films.*

D.E.Joyce, B.D.Fulthorpe, C.A.Faunce, T.P.A.Hase, I.Pape, B.K.Tanner, P.J.Grundy.

Physical Review B Vol. 58, No. 9 (1998)

**Chapter 6**

*The progression of interface structure through sputtered Co/Cu and Co/Pt multilayer films.*

B.D.Fulthorpe, D.E.Joyce, T.P.A.Hase, A.S.H.Rozatian, B.K.Tanner, P.J.Grundy.

Journal of Physics : Condensed Matter (accepted for publication, August 1999)

**Chapter 7**

*Experimental Evidence for Electron Channeling in Fe/Au (100) multilayers.*

P.A.Ryan, B.D.Fulthorpe, D.T.Dekadjevi, B.K.Tanner, B.J.Hickey.

(to be submitted)

# Declaration

I hereby declare that the work contained in this thesis is my own and has not been submitted previously for any other degree. The work of collaborators is acknowledged at the appropriate point. In particular I would like to declare that the magneto-transport and Transmission Electron Microscopy data presented in chapters 5 and 6 were undertaken by D.E.Joyce, University of Salford. Similarly, the magneto-transport measurements presented in chapter 7 were performed by P.A.Ryan and D.T.Dekadjevi, University of Leeds.

The samples used in this study were obtained from the following sources:

| | |
|---|---|
| Chapter 5: | D.E.Joyce, University of Salford. |
| Chapter 6: | D.E.Joyce, University of Salford. |
| Chapter 7: | P.A.Ryan, D.T.Dekadjevi, J.Xu, University of Leeds. |

# Table of Contents

# Chapter 1

# Aim and Outline of Work

## 1.1 Aim

Today, a decade after the initial observation of Giant Magneto-Resistance (GMR) in layered systems, the first commercial devices exploiting the phenomenon are now available in the marketplace. A large field of Condensed Matter research has developed since the original observation of the effect. While it is now widely believed that the scattering mechanisms responsible for GMR are intrinsically related to many aspects of the multilayer structure, a detailed understanding of the dominant factors influencing the magnitude of the GMR remains elusive.

The aim of the work presented in this study was to utilise x-ray scattering techniques to characterise the critical structural factors that control the magnitude of the GMR effect in magnetic multilayers. X-ray scattering techniques provide a powerful, non-destructive, tool with which to measure the intrinsically small, Ångstrom length scale structures within multilayers and, unlike scanning probe techniques, are also sensitive to the many buried interfaces within these systems. X-ray techniques are also able to globally average over micron length scales in the plane of the film, with a sensitivity to correlations both in and out of the plane. Interlayer exchange coupling, combined with spin-dependent and spin-independent scattering mechanisms, define the magneto-resistive behaviour of multilayers and are known to exhibit a strong structural dependence. Crucial factors such as layer thickness, interface morphology and crystalline texture can be determined, to a high degree of accuracy, through Specular and Diffuse X-ray Reflectivity measurements combined with X-ray Diffraction techniques.

## 1.2 Samples

The work presented in this study was undertaken as part of a collaborative venture with research groups at the Universities of Leeds and Salford. The Co/Cu and Co/Pt multilayers discussed in chapters 5 and 6 were grown, by magnetron sputtering, by D.E. Joyce at Salford. The Fe/Au samples in chapter 7 were grown, using molecular beam epitaxy (MBE), by P.A. Ryan and D.T. Dekadjevi at Leeds. The sample growers also performed the respective magnetic and magneto-transport measurements on the samples and I am grateful for their permission to include some of their data in the work presented in this study.

## 1.3 Outline of Thesis

Following the discussion of the aims and structure of the work presented here, chapter 2 moves on to a description of the theoretical treatment of the interaction of x-rays with matter under grazing incidence conditions. The Kinematical theory relating to the scattering of x-rays by electrons and atoms forms the starting point. Discussion proceeds, via the introduction of the concept of reciprocal space, to the scan types used in this work. A description of specular scatter, modified to account for roughness and grading at an interface, develops from the surface and interface behaviour of x-rays via the Fresnel equations. A treatment of diffusely scattered radiation is presented through the introduction of the Born Wave and Distorted Born Wave approximations, with a description of how the fractal nature of interfaces and the correlation between them in a multilayer can be represented.

Chapter 3 moves on to a discussion of the experimental aspects of x-ray scattering relating to the experimental set-up and data collection methodology of the synchrotron sources at which all of the data in this study was collected.

In chapter 4, an overview of the growth and origin of the GMR effect in magnetic multilayers is presented. Starting with a brief description of the two main methods of multilayer fabrication, sputtering and molecular beam epitaxy, discussion proceeds to the origin of the oscillatory exchange coupling and spin-independent scattering processes underlying the GMR effect in these systems. The structural considerations relating to these processes are then discussed.

The first results are presented in chapter 5. A series of Co/Cu multilayers, sputter deposited onto ion beam etched silicon substrates, have been studied. Specular and Diffuse X-ray Reflectivity data and simulations, in addition to High Angle X-ray Diffraction, Neutron Reflectivity and Electron Microscopy measurements, are presented in order to establish the origin of the observed loss of antiferromagnetic coupling and subsequent reduction in the GMR with increasing substrate etching voltage.

Chapter 6 is concerned with the propagation of interface structure as a function of bilayer number in a series of sputter deposited Co/Cu and Co/Pt multilayers. Specular, Transverse Diffuse and Longitudinal Diffuse X-ray scattering measurements have been utilised in order to follow the growth conformality of the interfaces within these systems as the number of bilayers increased. Strong evidence is found for the existence of a columnar growth mode in Co/Pt, not present in Co/Cu. Observations regarding the propagation of the interfaces are then discussed in relation to the magnetic properties of each system.

Chapter 7 relates to a series of (100) and (111) oriented epitaxial Fe/Au multilayers grown, by MBE, on MgO and sapphire respectively. Grazing Incidence Reflectivity, High Angle and Surface X-ray Diffraction measurements have been performed in an attempt to explain the distinct differences in the GMR and saturation conductivity as a function of spacer thickness between the two systems. Evidence points to the first observation of an electron channelling mechanism in Fe/Au (100). Grazing Incidence Fluorescence measurements show that a thin surface layer of Nb is present in Fe/Au (111), most likely due to Nb buffer material acting as a surfactant in Fe/Au (111) growth on sapphire. The chapter then concludes with the first experimental observation of a parabolic variation in the FWHM of rocking curves, taken through the High Angle diffraction satellites of Fe/Au (100), as a function of diffraction order. This observation is entirely consistent with a model proposed for identifying defect types within multilayers.

Finally, a summary and analysis of the important aspects of the work in this study is presented in chapter 8, along with a discussion of potential new and continued avenues of research in this field.

# Chapter 2

# Interactions of X-rays with Matter under Grazing Incidence Conditions

## 2.1 Introduction

In this chapter the theory relating to the interaction of x-rays with matter in the small angle regime will be discussed. Such grazing incidence scattering mechanisms underlie the majority of the experimental work presented in this study. Theoretical considerations relating to the wider field of x-ray diffraction fall largely beyond the scope of this work, although the techniques of High Angle and Grazing Incidence Diffraction will be discussed briefly in section 2.7 with regard to results presented later in this study.

Firstly, the kinematical theory relating to the interaction of x-rays with single electrons and then atoms will be presented. Discussion proceeds, via the introduction of the concepts behind reciprocal space, to the theoretical considerations underlying reflectivity and the type of measurements made throughout this study. The Born Wave and Distorted Born Wave approximations will be introduced prior to a consideration of diffuse scattering in simple single layer and multilayer systems. Finally, the principles behind other grazing incidence and diffraction techniques will be discussed briefly.

## 2.2 The Kinematical Theory

It is possible to consider the scattering of x-rays by electrons from either a classical or quantum mechanical standpoint. As it is only the elastic scattering of electrons that will be considered here, discussion will proceed via the classical formalism. The reader is referred to the articles by Kuriyama [1,2,3] for a review based on quantum mechanical principles. Any charged particle will be accelerated, and set into forced oscillation, by the electromagnetic radiation field associated with an x-ray

incident upon it. The charged particle, for example an electron, will then re-radiate with the same frequency as the incident wave but with a phase shift of $\pi$ upon scattering. This process is known as elastic Thomson scattering [4]. For an incident beam, of intensity $I_0$, the intensity of the scattered beam is given by [5]:

$$I_S = I_0\left(\frac{e^2}{mc^2}\right)^2\left(\frac{P}{R^2}\right) \qquad P = \begin{cases} 1 & \textit{for } \sigma \textit{ polarisation} \\ \cos 2\theta & \textit{for } \pi \textit{ polarisation} \end{cases} \qquad [2.1]$$

where $P$ is a polarisation factor, dependent on whether the incident beam is polarised in the plane, ($\sigma$) or perpendicular to it, ($\pi$), and $R$ is the distance between the particle and the observer. The Thomson scattering length is defined as $\left(e^2/mc^2\right)$ and is equal to $2.82\times10^{-3}$Å.

A typical atom represents a many electron system in which the electrons are spread out, in a continuous distribution, over a considerable volume, leading to differences in the phase of the scattered radiation from different parts of the atom. The atomic number of an atom is therefore the number of electrons per unit volume element, $\rho$, integrated over the entire volume such that:

$$Z = \int_V \rho(r)dV \qquad [2.2]$$

Away from any absorption edges within the material, the atomic scattering factor, $f$, is then defined as the Fourier transform of this electron density [6,7] such that:

$$f = \int_v \rho(r)\exp^{[ik.r]}\,dV \qquad [2.3]$$

Close to an absorption edge the scattering factor is liable to an anomalous dispersion correction as a consequence of the scattering phase change deviating from the value of $\pi$ mentioned earlier. The phenomenon of anomalous dispersion will be discussed in more detail in section 2.4.2.

## 2.3 The Definition of Reciprocal Space

If a series of atoms are held within a periodic crystal lattice, the electron density within that crystal will also be periodic in nature. As we have seen, scattering of x-rays from atoms is proportional to the Fourier transform of the electron density, equation 2.3, and can therefore be expanded as a series over Fourier space. Within this Fourier, or reciprocal, space any periodic function is represented by a single point. All spatial frequencies in real space are converted, via Fourier transform, to points in reciprocal space, the direction of a point corresponding to the direction of propagation of that frequency in real space.

The three primitive vectors describing the reciprocal lattice, $b_1$, $b_2$ and $b_3$, are linked to the three real lattice vectors, $a_1$, $a_2$, $a_3$, via the relations [8]:

$$b_1 = \frac{a_2 \times a_3}{a_1 \cdot a_2 \times a_3} \qquad b_2 = \frac{a_3 \times a_1}{a_1 \cdot a_2 \times a_3} \qquad b_3 = \frac{a_1 \times a_2}{a_1 \cdot a_2 \times a_3} \qquad [2.4]$$

The Ewald construction, shown in figure 2.1, provides a useful geometric method by which to transform between real and reciprocal space.

The angle of the sample with respect to the beam, $\theta$, defines the incident wave vector, $k_{in}$. Similarly the scattering angle, $\phi$, defines the exit wavevector, $k_{out}$. The scattering vector is the difference between these incoming and outgoing vectors. For elastic scattering the magnitude of each of these vectors is the same, such that:

$$|\boldsymbol{k}_{in}| = |\boldsymbol{k}_{out}| = |\boldsymbol{k}| = \left(\frac{1}{\lambda}\right) \qquad [2.5]$$

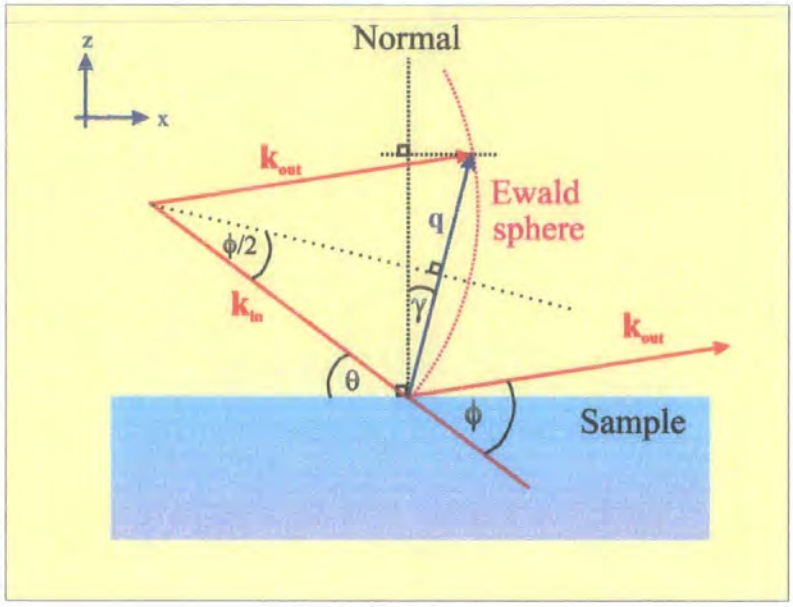


*Figure 2.1. Ewald construction showing the origin of the transforms between real and reciprocal space.*

The scattering vector, $\boldsymbol{q}$, can be expressed solely in terms of the angle $\phi$, such that:

$$\boldsymbol{q} = \left(\frac{2}{\lambda}\right)\sin\left(\frac{\phi}{2}\right) \qquad [2.6]$$

For any scattering vector, the out-of-plane, ($q_z$), and in-plane, ($q_x$), scattering components can then be expressed in terms of an additional angle, $\gamma$, where $\gamma = \theta - \left(\frac{\phi}{2}\right)$. The general transforms for all scattering vectors then become:

$$q_x = \left(\frac{2}{\lambda}\right)\sin\left(\frac{\phi}{2}\right)\sin\gamma \quad \text{and} \quad q_z = \left(\frac{2}{\lambda}\right)\sin\left(\frac{\phi}{2}\right)\cos\gamma \qquad [2.7]$$

An equivalent $q_y$ transform does exist but relates to scans performed within the horizontal plane of the film. All reflectivity measurements made in this study relate to out-of-plane $q_z$ and $q_x$ transforms only.

## 2.4 X-ray Reflectivity

The work presented in this study is primarily concerned with the scattering of x-rays under grazing incidence conditions. A detailed treatment of the principles behind x-ray diffraction measurements will therefore not be discussed here.

### 2.4.1 Scan Types in Reciprocal Space

The characterisation of a sample using grazing incidence techniques will typically lead to the use of three principal types of scan; the Specular, Longitudinal Diffuse and Transverse Diffuse scan. In all of these cases the detector is scanned out of the plane of the sample and probes only two dimensions within reciprocal space. However, there are advantages, in some cases, to scanning within the sample plane and these will be discussed later.

A common factor of $\left(\frac{2}{\lambda}\right)\sin\left(\frac{\phi}{2}\right)$, dependent only upon the detector angle, exists in both the $q_x$ and $q_z$ transform equations. The transforms differ only in the treatment of the $\gamma$ term. In the case of $\gamma = 0$ the $q_x$ term disappears and only $q_z$, the component normal to the surface, is non zero. This occurs whenever the sample angle, $\theta$, is half of the detector angle, $\phi$. A scan in which the detector and sample axes are coupled so that $\phi=2\theta$ at all times, probes the specular scatter as a function of $q_z$ only.

The diffuse scatter close to the specular condition can be measured as a function of $q_z$ by means of a small initial off-set in the sample angle. A coupled scan similar to the specular is then performed, mapping out a straight line in reciprocal space with a small angular off-set to the specular scan, figure 2.2. This type of scan is referred to as a longitudinal diffuse or off-specular.

A scan of the in-plane component of reciprocal space, $q_x$, can be performed by fixing the detector position. This maintains a constant value of $\phi$, while the sample angle, $\theta$, is scanned from 0 to $\phi$. Although the out-of-plane component does vary slightly during this type of scan, as a function of $\cos\gamma$, the variation is small in this low angle regime. This transverse diffuse scan can therefore often be considered as a $q_x$ only scan at fixed $q_z$.

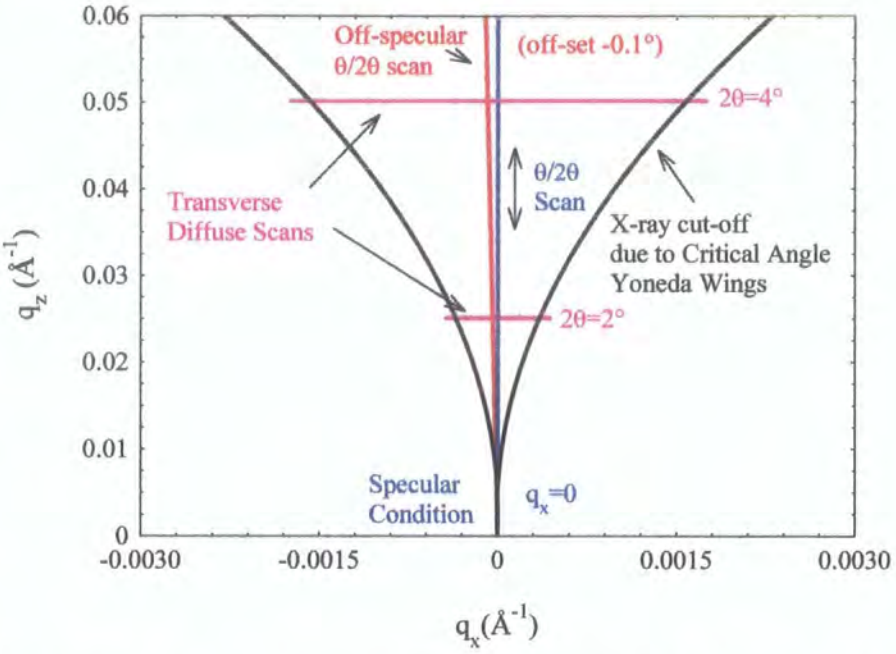


*Figure 2.2. Plan of reciprocal space showing the specular, off-specular and transverse diffuse scan modes. Simulated for a Si layer at $\lambda$=1.3926Å.*

A plan of reciprocal space is shown in figure 2.2, illustrating the various scan types. The arcs that mark the limit of observation are due to the incident and scattered x-rays existing only below the sample surface. A typical data set for a sample would include a specular scan ($q_z$ only), an off-specular scan, which is then subtracted from the specular to obtain the true specular scatter, and two or three diffuse scans.

## 2.4.2 Surface and Interface Behaviour of X-rays

When any form of electromagnetic radiation propagates from one material to another of different refractive index, boundary conditions exist that govern the way in which the x-ray, in this case, behaves. At the interface the amplitude and gradient of the incident and transmitted plane wave must be equal. This condition arises due to the need to match the tangential components of electric and magnetic field at the interface [9], with continuity arguments requiring the field gradient to also remain constant across the interface.

The refractive index, $n$, for a material of element $j$, with atomic number $Z_j$, atomic mass, $A_j$ and density $\rho_j$ is defined to be [10]:

$$n = 1 - \delta - i\beta \qquad [2.8]$$

where

$$\delta = \frac{N_A}{2\pi} r_0 \lambda^2 \sum_j \frac{\rho_j}{A_j} \left( Z_j + f_j' \right) \qquad [2.9]$$

and

$$\beta = \frac{N_A}{2\pi} r_0 \lambda^2 \sum_j \frac{\rho_j}{A_j} f_j'' \qquad [2.10]$$

with $N_A$ equal to Avagadro's number, $r_0$ the classical radius of electron orbit and $\lambda$ the wavelength. The $f'$ and $f''$ terms are the anomalous corrections to the normal atomic scattering factor, $f_0$, such that:

$$f = f_0 + f' + if'' \qquad [2.11]$$

When the frequency of the incident radiation is well away from any absorption edges within the material the absorption and dispersion of x-rays can essentially be neglected and the scattering factor is equal to $f_0$, the Fourier transform of the electron density function.

The anomalous corrections become important when the frequency of the incident radiation is close to an absorption edge. The $f''$ factor can also be important elsewhere in any regime where high absorption occurs. In either of these conditions the scattering factor is then subject to an anomalous correction and becomes complex. The correction terms, $f'$ and $f''$, vary as a function of wavelength, figure 2.3 a), and show large fluctuations close to absorption edges. A detailed treatment of the method by which these correction terms are calculated can be found elsewhere [11].

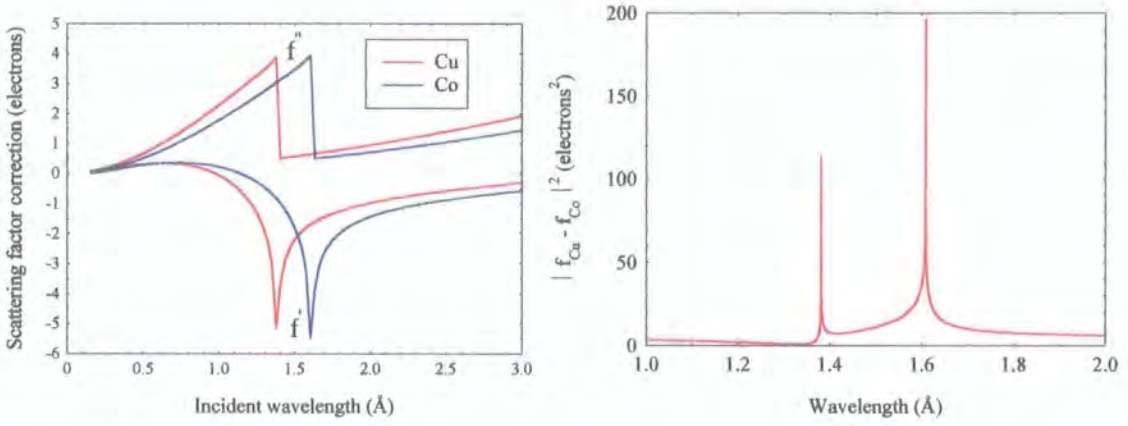


*Figure 2.3. The $f'$ and $f''$ correction terms a) and the variation in the scattering factor difference between Co and Cu, b) as a function of wavelength.*

The variation in the magnitude of the scattering factor difference between cobalt and copper as a function of incident wavelength is shown in figure 2.3 b). Away from the Co and Cu absorption edges the dispersion is not important and the scattering cross section is simply given by the Fourier transform of the electron density function. In this case the difference in the scattering cross section for each element is very small due to their proximity in the periodic table.

The tunability of synchrotron radiation allows the phenomenon of anomalous dispersion to be exploited in systems where the scattering contrast between layers is very small and the x-rays are effectively 'blind' to the interface between the two media. By tuning to an absorption edge it is possible to enhance dramatically the scattering factor difference between layers. The $\delta$ and $\beta$ terms of the refractive index are related to dispersion and absorption respectively. In the x-ray regime these values are both small and positive, of the order of $10^{-6}$ and $10^{-8}$ in each case, giving a refractive index slightly less than unity. As a consequence, x-ray radiation incident, from free space, onto a material interface sees the material as being optically less dense and is refracted away from the surface normal, as illustrated in figure 2.4.

As a consequence of the refractive index in the material being less than one, there exists a critical angle below which all of the incident radiation, minus a small loss

due to absorption, is totally externally reflected from the interface. The value of this critical angle, $\theta_c$, can be derived from Snell's law.

Each of the incident, transmitted and reflected x-rays beams shown in figure 2.4 can be expressed as a plane wave of general form:

$$\psi_j = C_j e^{ik_j.r} \qquad [2.12]$$

with phase, $k_j$ and amplitude, $C_j$ where $j$= $I,R,T$ for the incident, reflected and transmitted waves respectively. The phase of each plane is related via the refractive index of the material through which the wave propagates such that:

$$\frac{|k_I|}{n_{layer1}} = \frac{|k_T|}{n_{layer2}} = \frac{|k_R|}{n_{layer1}} = \frac{|k|}{n_{vacuum}} \qquad [2.13]$$

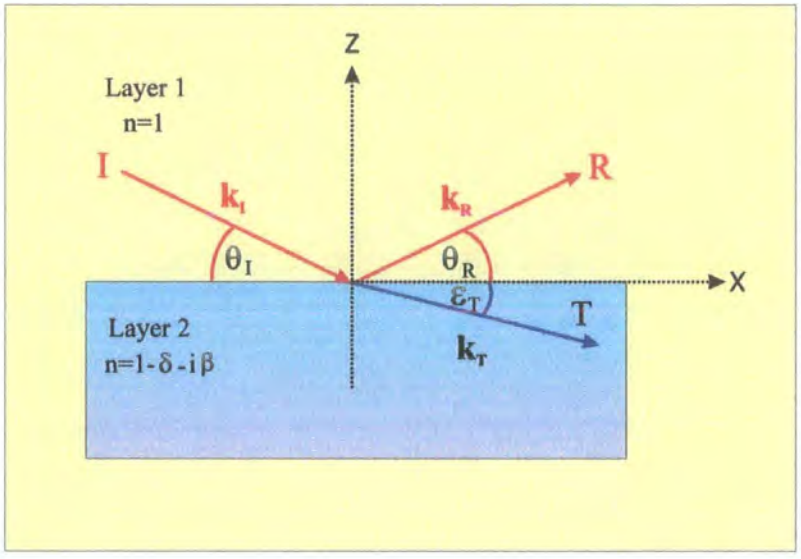


*Figure 2.4. Plane wave, incident at angle $\theta_i$ on an interface between two materials of different refractive index. The incident plane wave is both transmitted and reflected at the interface.*

Continuity arguments require that the amplitude and gradient of $\psi$ match at the interface for each of the plane waves, such that:

$$C_I + C_R = C_T \quad \text{and} \quad C_I \boldsymbol{k}_I + C_R \boldsymbol{k}_R = C_T \boldsymbol{k}_T \qquad [2.14]$$

When the surface component of the plane wave at the boundary is considered explicitly in equations [2.13] and [2.14] the familiar form of Snell's law is obtained:

$$n_{layer1} \cos\theta = n_{layer2} \cos\varepsilon_T \qquad [2.15]$$

At the critical angle condition the transmitted wave can be thought of as making an angle of $\varepsilon = 90°$ to the surface normal and effectively runs along the boundary between the two media. If the wave is incident from vacuum, ie $n_{layer1} = 1$, then the critical angle is defined as :

$$\cos\theta_c = n_{layer2} \approx 1 - \frac{\theta_c^2}{2} ..... \qquad [2.16]$$

If it is assumed that there is no absorption, $\beta = 0$, then a simple re-arrangement yields an expression for the critical angle:

$$n_{layer2} = 1 - \delta = 1 - \frac{\theta_c^2}{2} \qquad \text{therefore} \qquad \theta_c = \sqrt{2\delta} \qquad [2.17]$$

For incident beam angles below the critical angle, where $\varepsilon_T$ is complex, there exists an evanescent wave which penetrates a small distance into the material, even though the x-rays are totally reflected from the interface. The simulated penetration depth as a function of incident beam angle is shown, in figure 2.5, for gold and carbon substrates. The depth penetration of this evanescent wave is primarily dependent on the electron density of the near surface material. This can be seen by the way the incident beam begins to penetrate the carbon layer at a smaller incident angle than in the gold layer due to the lower electron density of carbon.

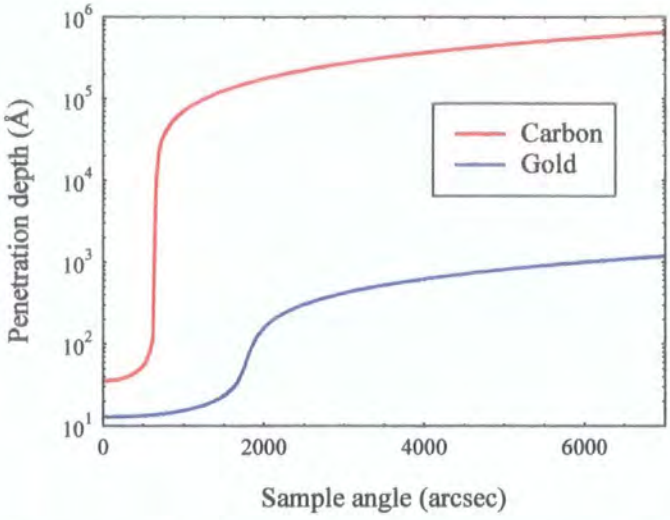


*Figure 2.5. Penetration depth as a function of incident beam angle for a carbon (red) and gold (blue) layer, λ=1.38Å.*

The electric field as a function of beam angle and depth is shown in figure 2.6 for a gold and carbon substrate and illustrates the same point.

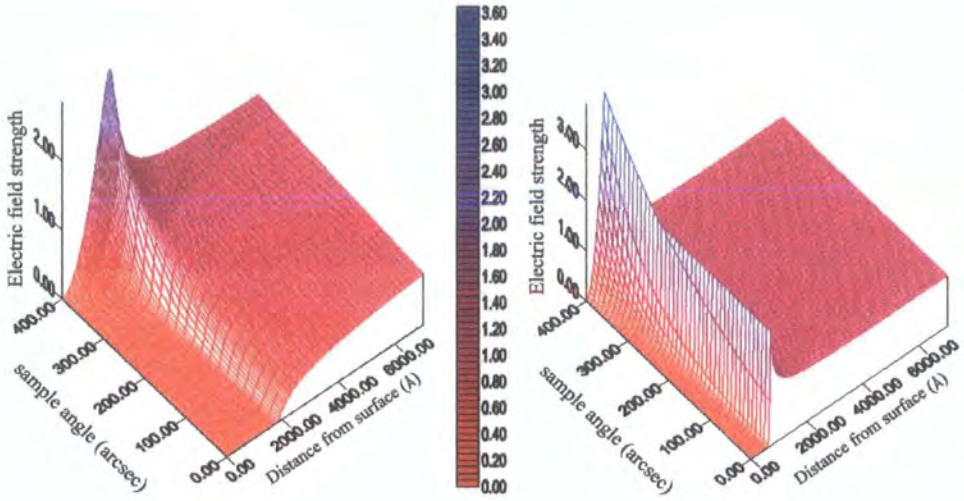


a) Gold b) Carbon

*Figure 2.6. Electric field within the material as a function of sample angle and distance from surface , λ=1.38Å.*

The inherent depth sensitivity of this evanescent wave at angles below the critical angle is exploited in surface sensitive techniques such as Grazing Incidence Fluorescence (GIXF) and Grazing Incidence Diffraction (GIXD) and will be discussed later.

Prior to the critical angle the amplitude of the transmitted radiation decreases exponentially with depth into the material to an extent governed by the absorption coefficient, $\beta$. For incident beam angles greater than the critical angle the x-rays penetrate the bulk of the material. The reflection and transmission coefficients for the incident x-ray beam, $\frac{R}{I}$ and $\frac{T}{I}$ respectively, can be obtained from the fact that at the interface ($z$=0) between the two media, figure 2.4, the tangential components of the electric and magnetic fields must be of equal magnitude and continuous. From this, the well known Fresnel formulas are obtained for the reflection, $F^{R}_{layer1}$ ,and transmission, $F^{T}_{layer1}$ coefficients:

$$F^{R}_{layer1} = \frac{k_{I,Z} - k_{T,Z}}{k_{I,Z} + k_{T,Z}} \qquad F^{T}_{layer1} = \frac{2k_{I,Z}}{k_{I,Z} + k_{T,Z}} \qquad [2.18]$$

with $$k_{I,Z} = -k_{R,Z} = |k_I| \sin\theta_I = kn_{layer1} \sin\theta_I \qquad [2.19]$$

and $$k_{T,Z} = |k_T| \sin\varepsilon_T = kn_{layer2} \sin\varepsilon_T \qquad [2.20]$$

in accordance with Snell's law.

In the small angle limit the Fresnel coefficients can therefore be expressed in terms of the incident and transmitted angles only, such that:

$$F^{R}_{layer1} \approx \frac{\theta - \varepsilon}{\theta + \varepsilon} \qquad \text{and} \qquad F^{T}_{layer1} \approx \frac{2\theta}{\theta + \varepsilon} \qquad [2.21]$$

In general this result will be modified for the two polarisation states of the radiation. However, because the refractive index for x-rays differs from unity by only a small amount, and the scattering angles are small, there is effectively no polarisation dependence.

In reality a system may be comprised of multiple interfaces and not just a simple single surface. The amplitude, *R*, of the specularly reflected wave within each layer of a multi-layered system was first calculated by Abelés [12] who connected the fields at an interface between two layers by means of a transfer matrix. Parratt derived an alternative, equivalent, recursive relation through an extension of the reflection and transmission coefficients for a single surface described by Fresnel's laws [13]. The reflected and transmitted electric fields within a multi-layered system are illustrated schematically in figure 2.7. In this formalism it is assumed that the multilayered system is terminated by a vacuum at the surface and a semi-infinite substrate at the base and that, as before, the interfaces are perfectly smooth.

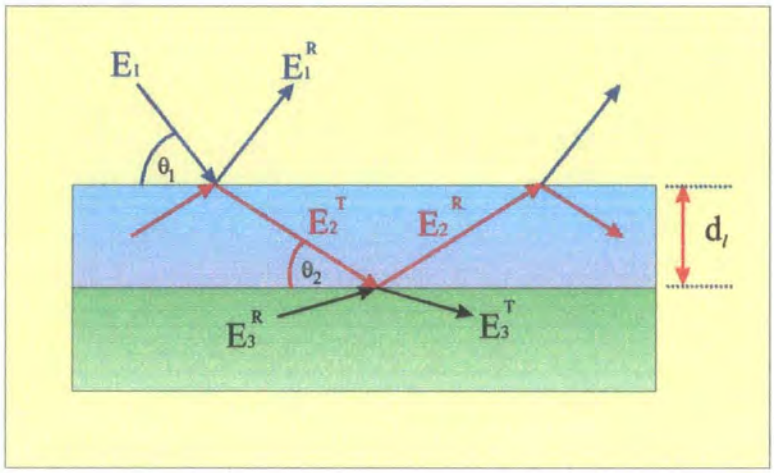


*Figure 2.7. Schematic representation of the reflected and transmitted electric fields within a multilayered system.*

As with the single interface, continuity requirements for the matching of the tangential electric field vectors at each interface still exist. This leads to the continuity relation developed by Parratt:

$$a_{l-1}E_{l-1}^{T} + \frac{E_{l-1}^{R}}{a_{l-1}} = \frac{E_{l}^{T}}{a_{l}} + a_{l}E_{l}^{R} \qquad [2.22]$$

where $E_l^R$ and $E_l^T$ are, respectively, the reflected and transmitted components of the electric field in layer $l$ and $a_l$ is the phase factor relating to half the layer thickness, $d_l$, such that:

$$a_l = \exp\left(-\frac{ikf_l d_l}{2}\right) \qquad [2.23]$$

where $f_l$ is the scattering factor for layer $l$ expressed in terms of the absorption, dispersion and the incident angle, $\theta$, such that:

$$f_l = \left(\theta_1^2 - 2\delta_l - 2i\beta_l\right)^{\frac{1}{2}} \qquad [2.24]$$

The recursive formalism describing the system arises from the solution to equation [2.22], which satisfies the continuity requirements, and gives the reflection amplitude for each interface as:

$$R_{l-1,l} = a_{l-1}^4\left[\frac{R_{l,l+1} + F_{l-1,l}^R}{R_{l,l+1}F_{l-1,l}^R + 1}\right] \qquad [2.25]$$

where the reflection coefficient moving from layer $l$ to $l+1$ is:

$$R_{l,l+1} = a_n^2\left[\frac{E_l^R}{E_l}\right] \qquad [2.26]$$

$F_{l-1,l}^R$ is the Fresnel reflection coefficient between layer $l$-1 and $l$:

$$F_{l-1,l}^R = \frac{(f_{l-1} - f_l)}{(f_{l-1} + f_l)} \qquad [2.27]$$

In a system of $N$ layers terminated by a semi-infinite substrate there is no reflected wave incident from below and therefore $R_{l,l+1} = 0$. This base layer forms the starting point for the recursive formula, working up to the surface. The ratio of the incident to reflected intensity is simply given as:

$$\frac{I_R}{I_0} = \left|\frac{E_1^R}{E_1}\right|^2 = \left|R_{1,2}\right|^2 \qquad [2.28]$$

### 2.4.3 Roughness and Grading at an Interface

The assumption so far that all of the interfaces within a multi-layered system are perfectly smooth is of course unrealistic. An interface will typically possess some form of roughness. This may be a 'true' roughness, in which elements of the surface are misoriented with respect to one another, or a graded variation in the electron density normal to the interface. A rough surface can be modelled as a perfectly flat interface onto which is superimposed a perturbation to that interface and can therefore be thought of as a collection of flat interfaces with a distribution about some average surface position. In this case the Fresnel reflectivity is modified by a Debye-Waller [14] factor. If the distribution of the collection of interfaces describing the surface is Gaussian in nature with a standard deviation, $\sigma$, then $\sigma$ describes the average interface width and is a measure of the roughness amplitude. The modified Fresnel coefficient then becomes:

$$R = F_l^R \exp\left[-(q_z\sigma)^2\right] \qquad [2.29]$$

where the average r.m.s roughness of the interface is defined as $\sigma$ and incorporates both the true roughness and grading components.

Névot and Croce [15] derived a more general form describing the modification to the reflection coefficient between two layers, $l$ and $l$-$1$, caused by a non-ideal interface:

$$R = F_l^R \exp\left(\frac{-k_l k_{l-1}\sigma_l^2}{2}\right) \qquad [2.30]$$

where $k_l$ and $k_{l-1}$ are the wavevectors in the layered media $l$ and $l$-$1$ respectively. When these modified Fresnel coefficients are then incorporated into the recursive formalism of Parratt, equation [2.27] becomes:

$$F_{l-1,l}^R = \frac{(f_{l-1} - f_l)}{(f_{l-1} + f_l)} \exp\left(\frac{-k_l k_{l-1}\sigma_l^2}{2}\right) \qquad [2.31]$$

A schematic representation of a rough and a graded interface is shown in figure 2.8. In both cases it is possible to represent the variation in electron density with distance across the interface with an error function. A rough interface can be replaced by an equivalent graded interface profile (displayed alongside in the figure) represented by this error function, the width of which defines the interface roughness. A purely graded interface, as illustrated by the second diagram of figure 2.8, can be represented by the same error function and could therefore be said to possess the same average 'roughness' as in the first case. The specular reflectivity is therefore insensitive to the nature of the interface perturbation, be it a true roughness or a graded transition from one layer to the next. The ability to distinguish between each type of interface arises from studying the diffusely scattered component of the radiation.

For a truly rough surface, there is a component of the incident radiation that is diffusely scattered out of the specular condition, leading to a reduction in the intensity of the specularly reflected beam. For a purely graded interface the specular intensity is reduced to the same extent, due to destructive interference between radiation reflected from points of differing density across the interface, but there is no diffuse scatter as there is no mechanism by which it can be generated.

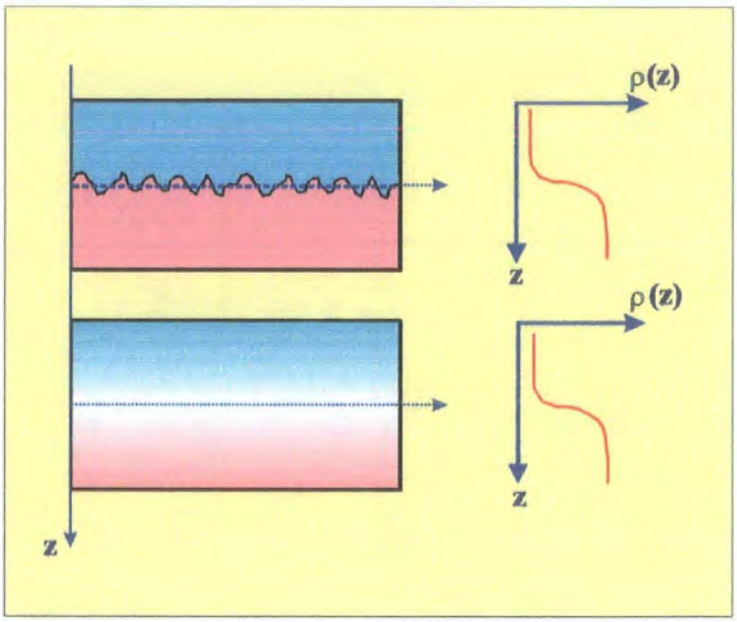


*Figure 2.8. Schematic representation of a rough and a graded interface along with the associated error profile.*

### 2.4.4 Specular Reflectivity

In the specular scattering geometry the scattering vector is directed normal to the sample surface at all times. Specular reflectivity measurements are sensitive principally to near surface electron density, layer thickness and average interface width. The effect of these can be demonstrated by looking at the simulated reflected intensity from simple structures.

The position of the critical angle for total external reflection is governed by the near surface electron density of the material. This is illustrated in figure 2.9 showing the specular reflectivity from a silicon and a gold substrate. The critical angle position, the point at which x-rays begin to penetrate the bulk of the layer, is larger for the gold layer due to the higher electron density.

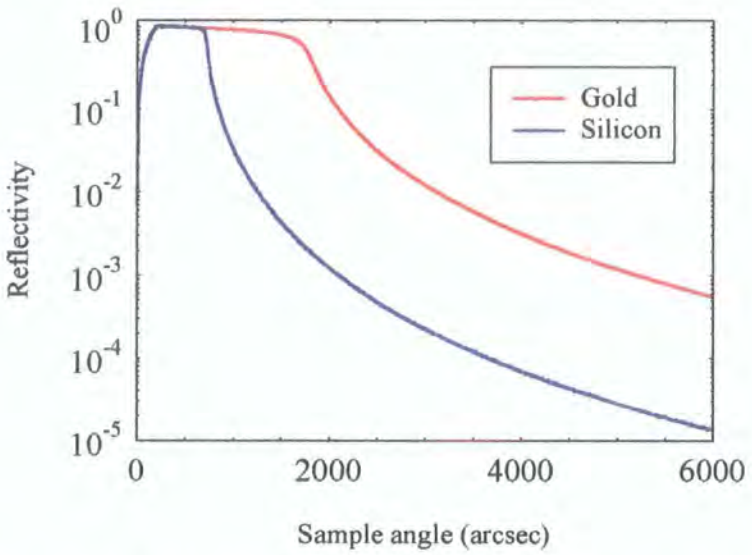


*Figure 2.9. Variation in the critical angle for silicon and gold due to differences in near surface electron density, $\lambda$=1.38Å.*

The simulated reflectivity curve for a silicon substrate is shown in figure 2.10 a). in which the roughness is varied from 0 to 8Å. In all cases in which the sample angle is below the critical angle the incident beam is totally externally reflected from the surface of the sample and there is no difference in the reflectivity. For angles greater than approximately twice the critical angle the reflected intensity falls as the inverse fourth power of the angle, as illustrated in figure 2.10 b) where the reflectivity is multiplied by $\theta^{4}$. Below this angle there is a small deviation due to refraction effects.

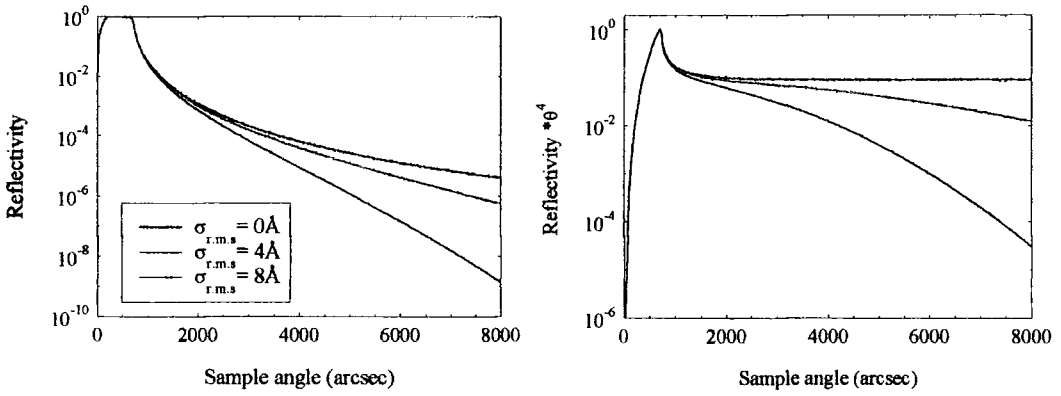


a) b)

*Figure 2.10. Variation in the rate of decrease of the specular intensity as a function of surface roughness, $\lambda$= 1.38Å.*

When roughness is introduced into the substrate surface the effect is to scatter x-rays out of the specular condition and the reflected intensity then decreases at a faster rate than that given by the simple power law.

With the addition of a layer onto the substrate, interference effects between x-rays reflected from the sample surface and the layer/substrate interface become important. Interference fringes, commonly known as Kiessig fringes [16], arise, with a period governed by the layer thickness, following the small angle approximation to Bragg's law:

$$d = \frac{\lambda}{2\Delta\theta} \qquad [2.32]$$

where $\Delta\theta$ is the period, in radians, of the Kiessig fringes at sample angles greater than $\approx 2\theta_c$ so that refraction effects can be neglected. The Kiessig interference fringes for a 250Å layer of gold and aluminium on silicon are shown in the simulations of figure 2.11, which illustrates the way in which the fringe amplitude is dependent on the difference in electron density between the layers.

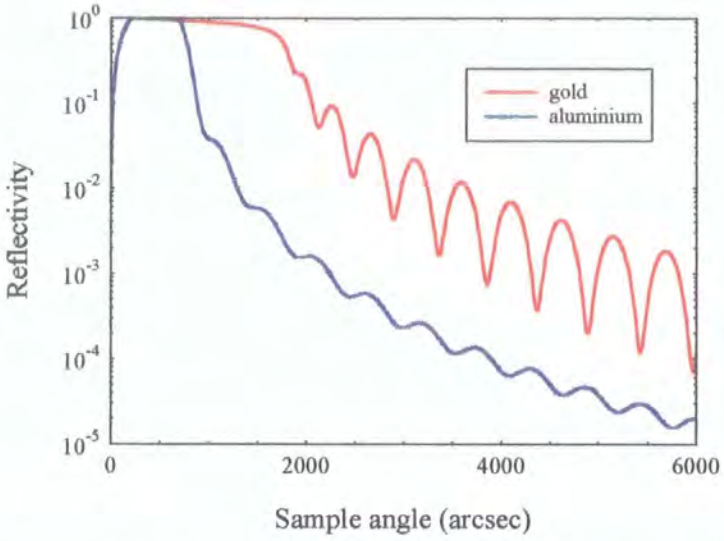


*Figure 2.11. 250Å layer of aluminium and gold on silicon, zero roughness, indicating the differences in fringe amplitude due to size of the electron density difference between the substrate and layer material, λ=1.38Å.*

The location of the roughness has subtle effects on the specular profile. Figure 2.12 shows a series of simulations for a 250Å layer of gold deposited on a silicon substrate. When the substrate roughness remains constant, and only the surface roughness is altered, the variations in the specular scatter occur at all angles, figure 2.12 a). However, when the surface roughness is fixed and only that of the substrate is varied any changes occur mainly at higher angles, figure 2.12 b).

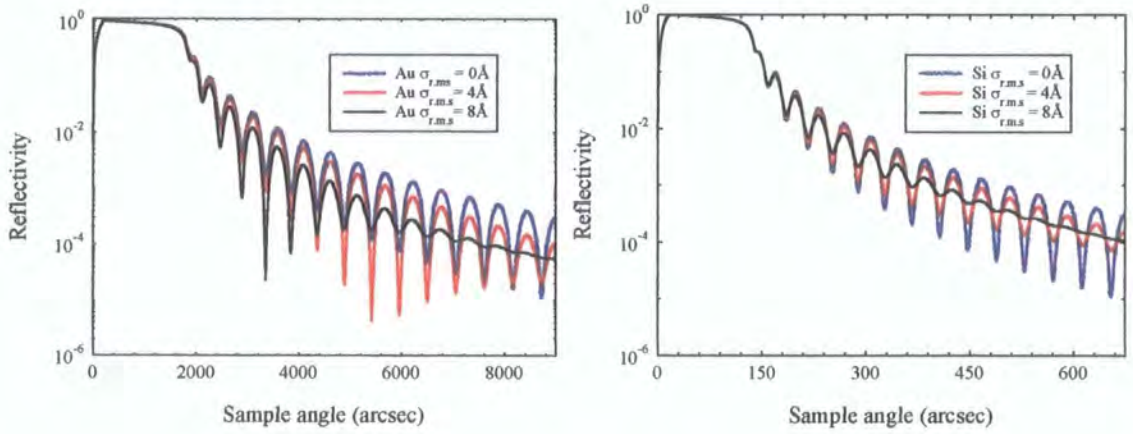


a) b)

*Figure 2.12. 250Å layer of Au on Si with a) varying Au surface roughness and b) varying Si substrate roughness, λ=1.38Å.*

Additional features appear in the reflectivity profile when more layers are added. For a multilayer system, consisting of many individual bilayer repeats, the reflectivity signal can be thought of in two distinct parts. Firstly, high frequency Kiessig, or thickness, fringes arise from interference between x-rays reflected from the top surface and substrate. In addition to this the bilayer repeats act as a pseudo crystal structure with a large lattice spacing out of the plane of the film. At certain scattering vectors this large $d$ spacing gives rise to constructive interference, described once again by Bragg's law

$$n\lambda = 2d\sin\left(\frac{\phi}{2}\right) \qquad [2.33]$$

and produces a specular Bragg peak. In figure 2.13 the reflectivity profile for 10 and 30 repeats of Fe(15Å)/Au(20Å) grown on silicon clearly shows the presence of both Kiessig fringes and Bragg peaks, the position of which is determined by the bilayer thickness. The intensity and sharpness of the Bragg peak depends on the number of bilayers, period dispersion and interface roughness within the structure. The Bragg peak position is not dependent on the crystallinity or long range order.

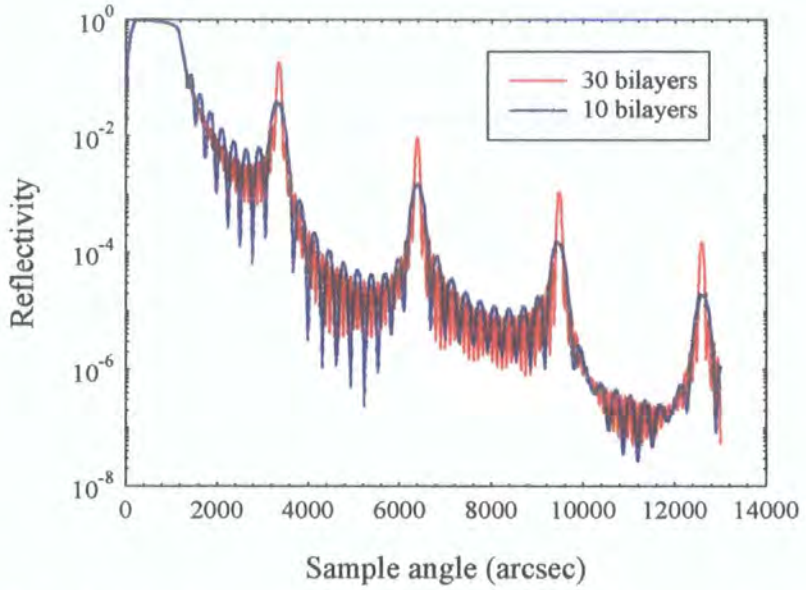


*Figure 2.13. Specular simulation for Fe/Au multilayer on Si showing the Kiessig fringes and Bragg peak for 30 and 10 bilayers, λ=1.062Å.*

## 2.5 Diffuse Scatter

The effect of roughness on the specular scatter can be described, as shown earlier, with the introduction of a Debye-Waller factor which simply acts as an exponential damping term. However, it is not possible to model the entire diffuse scatter in such a simple manner. Modelling of roughness is complicated by the fact that there are several issues that need to be considered as the roughness will most likely exhibit some form of correlation both in and out of the sample plane. The first stage in developing a model of the roughness within a layered system is to define the differential cross section for scattering, described within the Born Wave and Distorted Born Wave approximations.

### 2.5.1 The Born Wave Approximation

The Born wave approximation is a method by which to obtain a differential cross section that describes the way in which electromagnetic radiation interacts with, and is scattered by, a potential, *V(r)*. In this approximation it is assumed that there are two plane waves involved and that all scatterers are point like. Within the medium in which the scattering occurs, the scattering potential is constant and can be described as:

$$V = k_0^2\left(1 - n^2\right) \qquad [2.34]$$

where

$$V(r) = \begin{cases} 0 & \text{for r} > \text{ material dimension} \\ \text{constant} & \text{for r} < \text{ material dimension} \end{cases} \qquad [2.35]$$

again, $n$ is the refractive index of the material and $k$ the wavevector. We can express the differential scattering cross section as [17]:

$$\frac{d\sigma}{d\Omega} = N^2 b^2 \int_V dr \int_V \exp\left[-iq\cdot\left(r - r'\right)\right] dr' \qquad [2.36]$$

where $N$ is the number density of the particles involved in the scattering and $b$ is the scattering length which corresponds to the Thomson scattering length defined earlier in

the case of x-rays. This differential equation can then be expressed as a surface integral, via the application of Stoke's theorem, such that:

$$\frac{d\sigma}{d\Omega} = \frac{N^2 b^2}{q_z^2} \iint_{S_0} dx dy \iint_{S_0} \exp\left(-iq_z\left[z(x,y) - z(x',y')\right]\right) \exp\left(-i\left[q_x\left(x - x'\right) + q_y\left(y - y'\right)\right]\right) dx' dy' \qquad [2.37]$$

where the vector, $\boldsymbol{r} = r\text{-}r'$, in the first equation is now expressed explicitly in terms of the in-plane, (x,y), and out-of-plane, z(x,y), components. By describing this out-of-plane component as a Gaussian random variable, we have:

$$\left\langle \left[z(x',y') - z(x,y)\right]^2 \right\rangle = g(x' - x, y' - y) = g(\boldsymbol{R}) \qquad [2.38]$$

where $\boldsymbol{R} = \left(X^2 + Y^2\right)^{1/2}$. The differential cross section can then be expressed in terms of the area illuminated, $L_x L_y$, by the incident radiation such that:

$$\frac{d\sigma}{d\Omega} = \frac{N^2 b^2}{q_z^2} L_x L_y \iint_{S_0} dX dY \exp\left[-\left(q_z^2 g(\boldsymbol{R})/2\right)\right] \exp\left[-i\left(q_x X + q_y Y\right)\right] \qquad [2.39]$$

With the differential cross section in this form it becomes possible to obtain explicit expressions for the cross section for different models of the height difference function, $g(\boldsymbol{R})$.

## 2.5.2 Fractal Surfaces and the Correlation Function

The idea of incorporating a fractal surface was introduced by Sinha *et al* [17]. The height difference function is modified to introduce a fractal component such that:

$$g(X,Y) = g(\boldsymbol{R}) = A(\boldsymbol{R})^{2h} \qquad [2.40]$$

where $\boldsymbol{R}$ is a vector along the surface with a fractal exponent, $h$, describing the texture of the surface in question such that:

$$h = \begin{cases} 0 & \text{highly jagged} \\ 1 & \text{smooth} \end{cases} \qquad \text{where} \qquad 0 < h < 1 \qquad [2.41]$$

This model becomes unphysical for extreme distances where the roughness tends towards infinity. A cut-off is introduced with a length scale that is, in practise, governed by growth effects within the sample. The cut-off limited height difference function then becomes:

$$g(\boldsymbol{R}) = 2\sigma^2\left[1 - \exp\left\{-\left(\frac{(\boldsymbol{R})}{\xi}\right)^{2h}\right\}\right] \qquad [2.42]$$

and as the distance, $\boldsymbol{R}$, tends towards infinity the relative height between two points described by the height difference function tends to $2\sigma^2$.

In the modelling of the diffuse scatter from interfaces it is preferable to consider a height-height correlation function, $C(\boldsymbol{R})$ rather than the height difference function. This correlation function provides a measure of the degree of knowledge that two points on a surface, separated by a distance, $|R|$, have about one another. The height-height correlation function is defined as:

$$C(\boldsymbol{R}) = \langle z(\boldsymbol{R})z(0,0)\rangle = \sigma^2 - \frac{1}{2}g(\boldsymbol{R}) \qquad [2.43]$$

which can then be expressed, via equation 2.42, as:

$$C(\boldsymbol{R}) = \sigma^2 \exp\left[-\left(\frac{(\boldsymbol{R})}{\xi}\right)^{2h}\right] \qquad [2.44]$$

The height difference function, equation 2.42, and the height-height correlation function, equation 2.44, as a function of the fractal parameter, $h$, are shown graphically in figure 2.14. The common point of the curves for each correlation function corresponds to the surface vector, $\boldsymbol{R}$, that is equal to the length scale across the surface over which the correlation between two designated points is reduced by a factor of $e^{-1}$.

This length scale, 200Å in this case, is defined as the lateral correlation length, $\xi$, and defines the area of the surface that is fractal in nature.

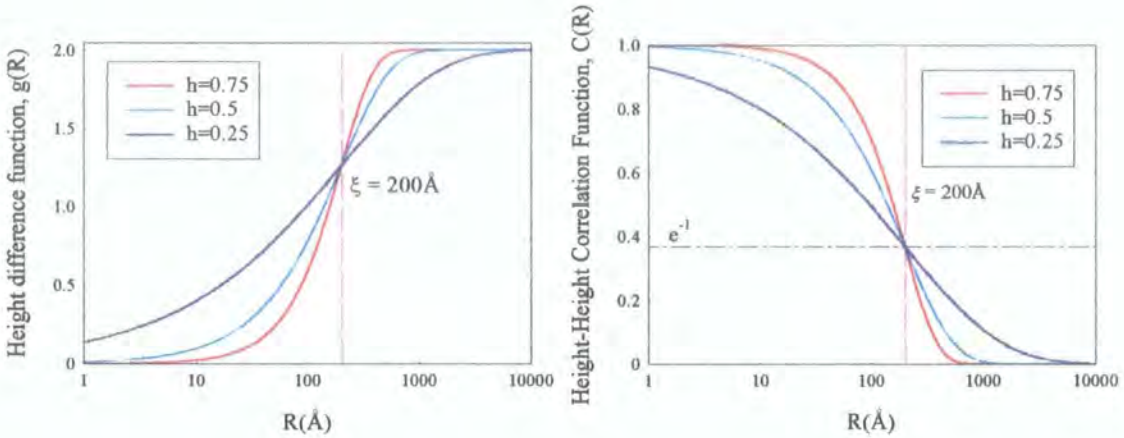


*Figure 2.14. Height difference function a) and height-height correlation function b), for various values of fractal parameter, as a function of the surface vector, **R**, with a single correlation length of 200Å.*

Although other statistical descriptions of interfaces have been proposed [18-20], the correlation function proposed by Sinha *et al.* is straightforward to incorporate into the scattering theory. It corresponds to that used in the commercial simulation code, Bede REFS, written by M.Wormington [21,22] which has been used in the modelling of the data in this study.

When this height-height correlation function is incorporated into equation 2.39 the differential cross section becomes:

$$\frac{d\sigma}{d\Omega} = \frac{N^2 b^2}{q_z^2} L_x L_y \exp\left[-q_z^2\sigma^2\right] \iint_{S_0} dXdY \exp\left[q_z^2 C(\boldsymbol{R})\right] \exp\left[-i\left(q_x X + q_y Y\right)\right] \qquad [2.45]$$

with $\boldsymbol{R} = \left(X^2 + Y^2\right)^{1/2}$. It is possible to subdivide the terms in this expression in order to express the specular and diffuse components explicitly such that:

$$S_{spec}(q) = F_l^R \exp\left(-q_z^2\sigma^2\right) \quad [2.46]$$

$$S_{diff}(q) = \frac{2\pi}{q_z^2}\exp\left(-q_z^2\sigma^2\right)\int_0^\infty \boldsymbol{R}\left[\exp\left(q_z^2\sigma^2 e^{-\left(R/\xi\right)^{2h}}\right) - 1\right]J_0\left(q_{x,y}\boldsymbol{R}\right)d\boldsymbol{R} \quad [2.47]$$

where $S(q)\cdot N^2b^2$ is the differential cross section per unit area, $F_l^R$ is the Fresnel reflection coefficient, as defined in equation 2.21, and $J_0\left(q_{x,y}\boldsymbol{R}\right)$ is a Bessel function of the first kind.

### 2.5.3 The Distorted Wave Born Approximation (DWBA)

The Born approximation assumes that the interaction between the wavefields of the incident radiation and that generated by the point like scatterers is weak. This is clearly not valid at very low grazing incidence angles where the intensity of the scattered radiation is high. It is for this reason that in the modelling of the specular reflectivity and diffuse scatter it is the distorted version of the Born approximation that must be used. In the Born approximation it was assumed that a surface could be treated simply as a perturbation that acted upon the Fresnel solutions to the wave equation. The DWBA differs in the treatment of a rough surface in that it is assumed that it is the actual roughness itself and not the surface that acts as a perturbation to the Fresnel solutions and the approximation applies the perturbation theory directly to the exact solution of the wave equation for an ideal smooth surface. This approach was first applied by Sinha *et al.* in a continuation of the work outlined previously. The reader is referred to this paper [17] for a more detailed derivation of the scattering cross sections obtained from the DWBA, the key aspects of which will be outlined in the rest of this section.

The specular and diffuse scattering cross sections can be obtained, via the DWBA, by separating the scattering potential into two distinct terms:

$$V=V_1+V_2 \quad [2.48]$$

where $V_1$ is the potential of the ideal system and $V_2$ is the potential that acts as a disturbance to this ideal case where:

$$V_1 = \begin{cases} k_0^2\left(1-n^2\right) & -a < z < 0 \\ 0 & z > 0 \end{cases} \quad V_2 = \begin{cases} k_0^2\left(1-n^2\right) & 0 < z < z(x,y) \quad \text{if } z(x,y) > 0 \\ -k_0^2\left(1-n^2\right) & z(x,y) < z < 0 \quad \text{if } z(x,y) < 0 \\ 0 & \text{elsewhere} \end{cases}$$

[2.49]

and it is possible to find the solution to the ideal wave equation:

$$\nabla^2\phi + k_0^2\phi - V_1\phi = 0 \qquad [2.50]$$

Sinha *et al.* define the transition probability [17]:

$$\langle 2|T|1\rangle = \langle \tilde{\psi}_2|V_1|\phi_1\rangle + \langle \tilde{\psi}_2|V_2|\psi_1\rangle \qquad [2.51]$$

in which z(x,y) represents the statistical average of the surface. It is the incident plane wave, represented by the wavefunction $\phi_1$, that is scattered by the potential $V_1$. The ensemble of reflected and transmitted plane waves generated at the interface are then represented by an exact eigenstate, $\psi_1$, produced from the Fresnel theory. It is these plane waves that then experience the perturbation generated by the roughness potential, $V_2$, and the scattering from waves originating from within the sample, represented by the time reversed eigenstate, $\tilde{\psi}_2$, serves to ensure a unique final solution.

The full expression for the specular scatter, in which the roughness is expanded assuming Gaussian statistics, is given by the modification of the Fresnel coefficients discussed earlier:

$$\left|R(k)\right|^2 = F_l^R \exp\left(-q_z q_z' \sigma^2\right) \qquad [2.52]$$

which is similar to the results obtained from the Born wave approximation, equation 2.30, and that obtained using a different method, by Névot and Croce [15]. The DWBA solution proves to be very accurate in modelling the high intensity region of the specular scatter close to the critical angle, where the Born approximation becomes invalid. At higher scattering vectors the DWBA tends to overestimate the amount of

specular scatter but in this regime the conditions pertaining to the Born approximation are valid and circumvent this problem. In each of the regions in which the Born and Distorted Born approximations are valid, equation 2.52 has been shown [23] to produce solutions that are indeed the limiting case of the more general form of the specular scatter.

Further manipulation leads to the DWBA for the differential cross section for diffusely scattered radiation [17]:

$$\left[\frac{d\sigma}{d\Omega}\right]_{diffuse} = L_x L_y \frac{\left|k_0^2\left(1-n^2\right)\right|^2}{16\pi^2} \left|T(k_1)\right|^2 \left|T(k_2)\right|^2 S(q_t) \qquad [2.53]$$

where $\left|T(k_n)\right|^2$ are the Fresnel transmission coefficients for the incident ($n$=1) and scattered ($n$=2) waves and $L_X L_Y$ defines the illuminated area. Work by Weber and Lengeler [24] has shown that it is in fact the modified Fresnel coefficients, including the exponential damping term that accounts for the roughness, equation 2.30, that should be used in the above expression. The $S(q_t)$ term in equation [2.53] contains a Fourier transform which must be calculated numerically as it has no analytical solution. The simulation code used to analyse the data in this study [21,25,26] is based upon the Distorted Wave Born approximation and the height-height correlation function outlined here. The long processing time involved in the numerical calculation of the $S(q_t)$ term is avoided in this code through the use of look up tables. The DWBA model also allows the accurate simulation of the region of specular and diffuse scatter close to the critical angle as the approximation encompasses the necessary Fresnel transmission coefficients.

## 2.6 Diffuse Scatter from Single and Multilayer Interfaces

The main features of the diffusely scattered component of the radiation from a surface or interface can be demonstrated through simulation of transverse diffuse (fixed detector) scans, as described in section 2.4.1. The sensitivity of the diffuse scatter to the magnitude of the roughness and the near surface electron density is shown in figure 2.15 a) and b). As the roughness of the surface or interface is the mechanism by which

the diffuse scatter is generated it is unsurprising to see a pronounced increase in the level of the diffuse scatter as the roughness increases, figure 2.15 a). A sharp, instrument defined, peak is observed in all cases at the $q_x$=0 point corresponding to the relatively high intensity scatter arising at the position of the specular condition. As the diffuse scatter increases with roughness the specular intensity decreases in response as more x-rays are scattered out of the specular condition. Two other peaks, symmetric in position about the specular condition, also exist corresponding to the rise in intensity associated with a beam incident at the critical angle. These are the Yoneda wings and arise from the inclusion of transmission coefficients within the Distorted Wave Born approximation. For a beam incident on an interface at exactly the critical angle for total external reflection, the transmitted component of the incident beam lies along the surface and the amplitude of the electric field is doubled.

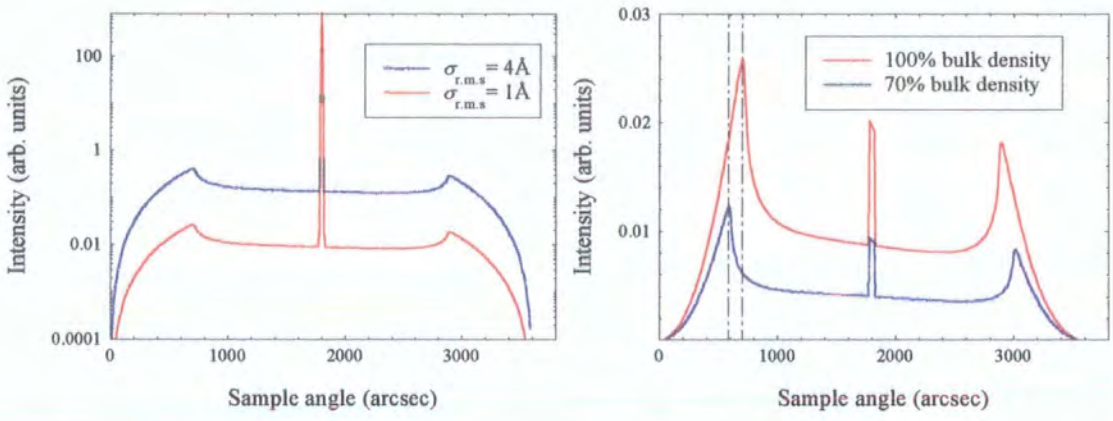


*Figure 2.15. Variation in the diffuse scatter for a Si substrate with a) roughness and b) bulk density.*

The position of the Yoneda wings is sensitive to the near surface electron density at the scattering interface, as illustrated in figure 2.15 b), with the existence of the second Yoneda wing following from reciprocity arguments relating to the geometry of the scattering. The asymmetry in the intensity of the first and second Yoneda wing is due to the change in the size of the beam footprint as a function of sample angle. The diffuse scatter is proportional to the area of the sample illuminated by the incident beam. This asymmetry can be removed with a simple sine correction to compensate for this variation.

In the derivation of the height-height correlation function the concepts of a lateral correlation length, $\xi$, and fractal parameter, $h$, were introduced as a method of describing a surface and the self knowledge of neighbouring points on that surface. The effect of the value of these parameters on the diffuse scatter is shown in figure 2.16 a) and b). The profile of the diffuse scatter is extremely sensitive to the magnitude of the lateral correlation length. As the correlation length increases there is a pronounced increase in the diffuse scatter close to the specular condition at $q_x$=0. The longer the correlation length the longer the surface period of the roughness. Within reciprocal space any lateral periodicity on a surface is translated to a single point in $q_x$. A long surface period represents small values of $q_x$ and the diffuse scatter, proportional to the Fourier transform of the roughness length scale, is therefore concentrated in the small $q_x$ region. At the other extreme of small roughness length scales the diffuse scatter is confined to the high $q_x$ regime which may often be beyond the limit of observation defined by the sample cut off, the sweeping arcs of figure 2.2. From figure 2.2 it is clear that for high values of $q_x$ it is necessary to probe large values of $q_z$ in order to capture all of the diffuse scatter from a short correlation length surface.

However, the amplitude of the diffusely scattered radiation falls as $q_z^{-2}$ which is another problem in studying the diffuse scatter in the high $q_z$ regime. It is possible to overcome this problem using the method proposed by Salditt *et al.* [27-31] in which the detector is scanned out of the scattering plane and is essentially a $q_y$ scan. In such a scan geometry there is no sample cut-off and it is possible to scan the full range of $q_y$ at a fixed value of $q_z$ suitably small enough to maintain a high level of diffuse scatter.

It is clear from figure 2.16 b) that the shape of the diffuse scatter is also sensitive to the fractal parameter. As the fractal parameter is reduced in size the central region close to the specular condition becomes more peaked and the scatter at the higher values of $q_x$ is reduced.

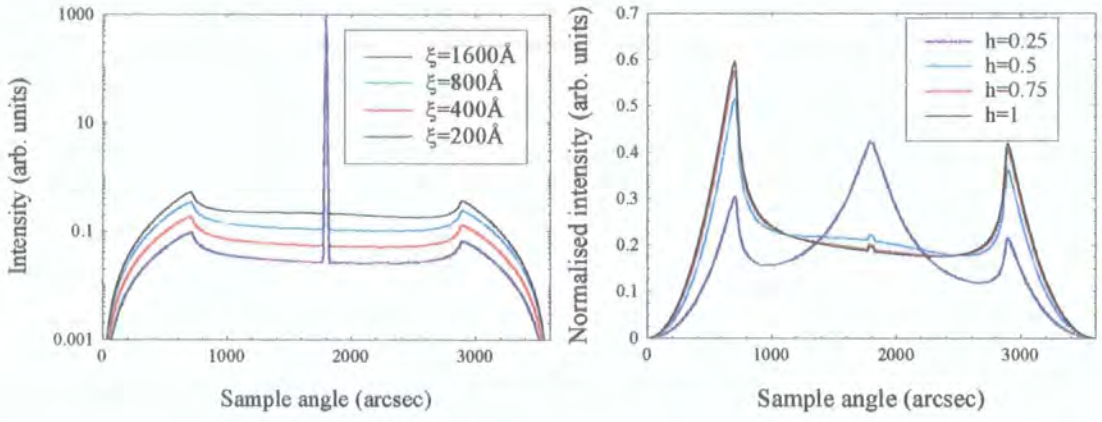


*Figure 2.16. Sensitivity of the diffuse scatter to a) lateral correlation length, $\xi$, h=0.5 and b) fractal parameter, h, with $\xi$=1600Å. Average roughness = 4Å in each case.*

The work of Salditt *et al.* showed that it was also necessary to use high scattering vectors to study the fractal aspect of a surface. Once again the method of scanning the detector out of the scattering plane, outlined above, can be used to facilitate this although no such measurements were used in the work presented in this thesis.

For a multilayer sample possessing many interfaces, the out-of-plane correlation between the roughness at the interfaces becomes important [32-34]. The schematic diagram in figure 2.17 shows the two extremes of the possible roughness profiles. Firstly, completely correlated or conformal roughness in which the spatial frequencies of the roughness at one interface are replicated exactly across successive layers from the substrate to the surface. At the other extreme the roughness may be completely uncorrelated in nature with the roughness at each interface being completely independent of that in the neighbouring layers. In reality it is most likely that a true interface will possess both correlated and uncorrelated regions and may also exhibit a certain degree of grading. It is possible to relate all of these terms such that [35]:

$$\sigma_{r.m.s}^2 = \sigma_{correlated}^2 + \sigma_{uncorrelated}^2 + \Sigma_{grading}^2 \qquad [2.54]$$

where $\sigma_{r.m.s}$ is the average interface width deduced from the rate of decrease of the specular scatter.

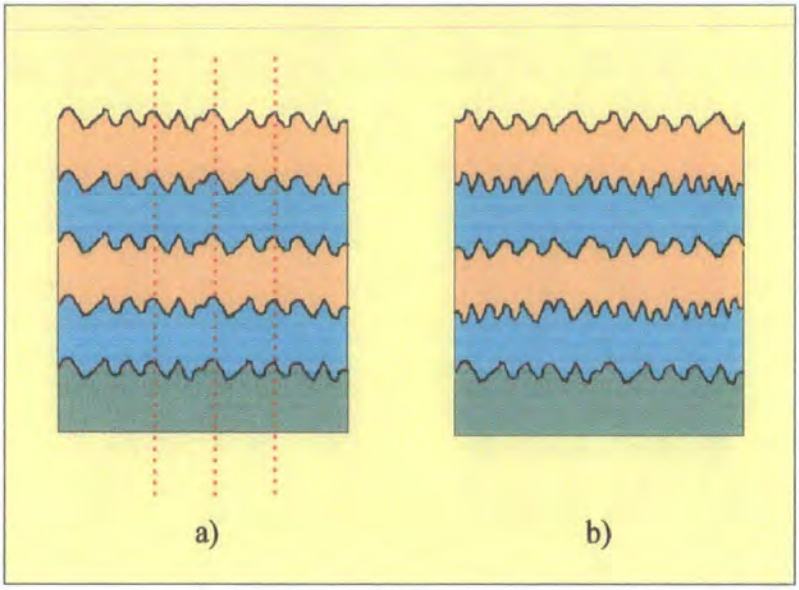


*Figure 2.17. Schematic representation of roughness which is a) totally correlated and b) uncorrelated between successive interfaces.*

The work of Holý *et al.* [36-38] and Schlomka [39] extended the model of the diffuse scatter, proposed by Sinha, to include the behaviour of a multilayered sample. The out-of-plane correlations can be modelled with the use of a covariance function:

$$C_{j,k}(\boldsymbol{R}) = \left\langle \delta z_j(0)\delta z_k(\boldsymbol{R}) \right\rangle \qquad [2.55]$$

where $\delta z_j$ and $\delta z_k$ refer to the local centres of the roughness profile at the $j$-th and $k$-th interface.

There are, in principal, two methods by which to model out-of-plane correlations within a multilayer. In a similar way in which the lateral structure of an interface can be characterised by a correlation length, $\xi$, it is also possible to define an out-of-plane correlation length, $\zeta$, over which the roughness of the substrate is replicated through the stack. This correlation length is defined as the out-of-plane distance over which the correlations between the $j$-th and $k$-th interfaces are damped by a factor of $e^{-1}$. Using this model the covariance function becomes:

$$C_{j,k}(\boldsymbol{R}) = \sigma_{j,k}^2 \exp\left[-\left(\frac{\boldsymbol{R}}{\xi_{j,k}}\right)^{2h}\right]\exp\left[\frac{-|z_j - z_k|}{\zeta}\right] \qquad [2.56]$$

where $\sigma_{j,k}^2 = \sigma_j^2 + \sigma_k^2$ and $\xi_{j,k}^{2h} = \frac{\xi_j^{2h} + \xi_k^{2h}}{2}$. Using this approach a very accurate description of the interface correlations is obtained because the lateral correlation length and roughness are defined for each individual interface. However, a small increase in the number of layers leads to a large increase in the computational time involved in calculating this term which scales with the square of the number of layers.

An alternative form of the covariance function, which has the advantage of a processing time that scales linearly with layer number, involves specifying the correlated or uncorrelated roughness fraction at each interface such that:

$$C_{j,k}(R) = \left(\sigma_{u,j}\sigma_{u,k}\delta_{j,k} + \sigma_{c,j}\sigma_{c,k}\right)\exp\left[-\left(\frac{R}{\xi}\right)^{2h}\right] \qquad [2.57]$$

In this model the roughness at each interface is represented by an intrinsic component, $\sigma_{u,j}$, and an additional component that has originated from the substrate and replicated upwards exactly, the $\sigma_{c,j}$ term. By varying the second term, the amount of roughness that is correlated at any interface can be specified as a proportion of the total interface roughness. In this model the lateral correlation length and fractal parameter are held constant at each interface.

The effect of the nature of the roughness on the diffuse scatter can be seen most clearly in a full reciprocal space map (FRSM). The two FRSM's shown below have been calculated for an Fe/Au multilayer of nominal structure {Fe(15Å)/Au(20Å)}×15 using the second of the two covariance functions described above. The specular scan corresponding to this structure is the same as that shown in figure 2.13. An average interface roughness of 6Å was used which was varied between totally uncorrelated, figure 2.18 a) and totally correlated 2.18 b). The lateral correlation length and fractal parameter were set at 200Å and 0.25 respectively.

For a system in which the interface roughness is completely uncorrelated the diffuse scatter is distributed randomly throughout reciprocal space. This can be seen in figure 2.18 a) in which there is simply a steady reduction in the intensity of the diffuse scatter with no obvious features.

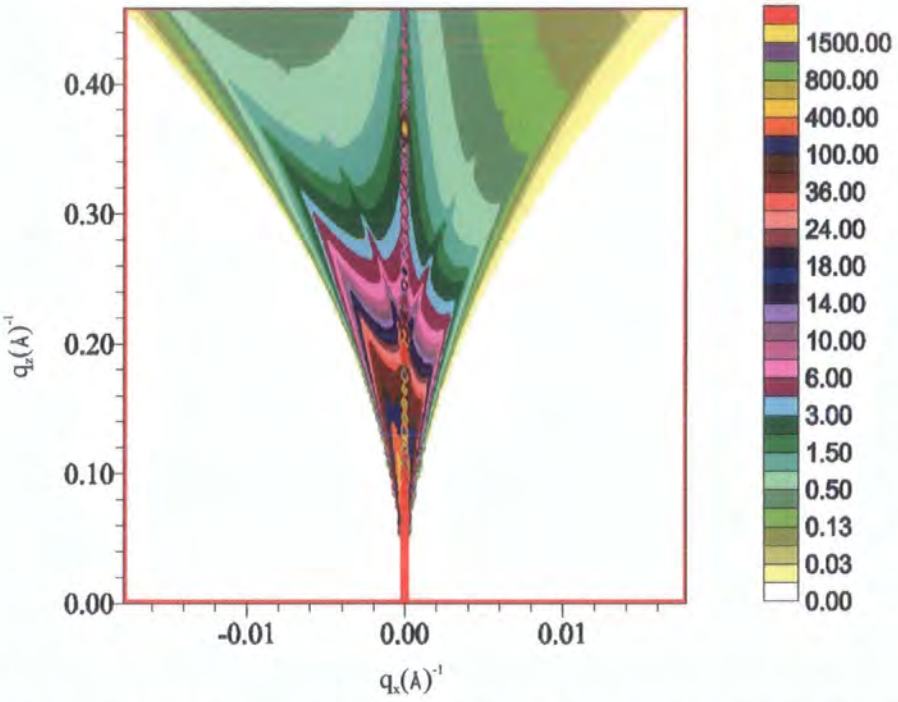


*Figure 2.18 a). Full reciprocal space map for an Fe/Au multilayers in which the interface roughness is uncorrelated.*

The asymmetry in the scatter about $q_x$=0 is due to the inclusion of the variation in the size of the beam footprint with sample angle. It should be noted that in the second of the FRSM's the specular ridge has not been included.

The situation becomes very different when the roughness is completely correlated in nature between the interfaces, figure 2.18 b). Rather than being distributed randomly throughout reciprocal space, the diffuse scatter is now confined into regions termed resonant diffuse sheets (RDS) at the positions of the Bragg peaks, arising from coherent scatter within the bilayers. The curvature of these diffuse sheets, sometimes referred to as Holý bananas [37], arises due to refraction effects. The continuous curved lines stretching out along the Ewald spheres mark the positions of the Bragg like peaks and arise due to dynamical effects, discussed in more detail by Holý *et al.* [37].

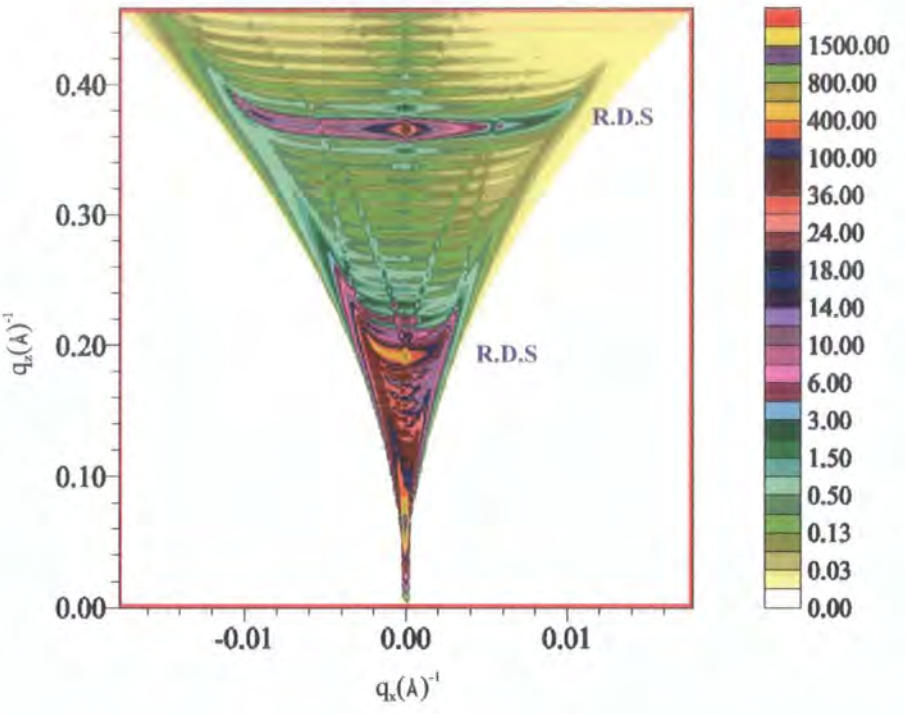


*Figure 2.18 b). Full reciprocal space map for an Fe/Au multilayer in which the interface roughness is totally correlated.*

The localisation of the diffuse scatter at specific values of $q_z$ and the existence of these wide resonant diffuse sheets means that for a system in which the roughness is highly correlated, an off-specular scan possessing a small $q_x$ off-set, will exhibit the same periodic features as the specular scan, namely the Kiessig fringes and Bragg peaks. This extension of the periodicity into $q_x$ depends on the frequency of the roughness that is being replicated [36,40]. As correlated roughness tends to be low frequency in nature and low frequency roughness is most easily replicated, the presence of off-specular Kiessig fringes and Bragg peaks is strongly indicative of a sample in which the roughness is highly correlated in nature. This observation is of specific importance regarding the work discussed in chapter 6.

A series of off-specular simulations, performed using the second covariance function, are shown in figure 2.19 for an Fe/Au multilayer in which the total stack thickness is equal to 350Å and the roughness is highly correlated. When the out-of-plane correlation length, $\zeta$, is in excess of the total stack thickness all of the interfaces are highly correlated and the off-specular scan exhibits Kiessig fringes and Bragg peaks. As the out-of-plane correlation length is reduced below the stack thickness the Kiessig

fringes are lost, as the scatter from the substrate and top surface is no longer coherent, and the Bragg peak broadens due to the reduction in the number of correlated bilayers.

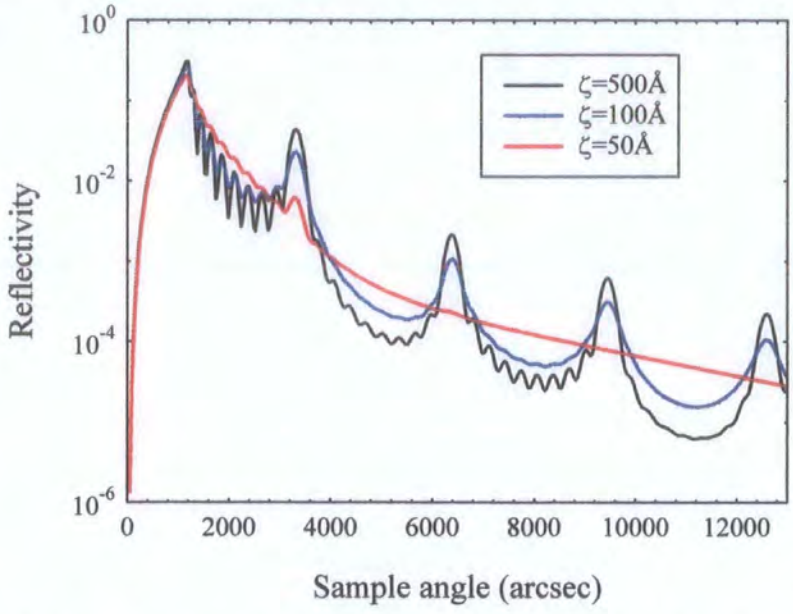


*Figure 2.19. Off-specular simulations, coupled $\theta/2\theta$ with -0.1° off-set, for Fe/Au multilayer for varying vertical (out-of-plane) correlation length, $\zeta$.*

## 2.7 Additional X-ray Techniques

During the course of this study additional x-ray techniques other than those of Grazing Incidence Reflectivity have been used. Such techniques will be summarised below and in each case the reader is referred to more detailed texts for a more comprehensive description.

### 2.7.1 High Angle X-ray Diffraction (HXRD)

A High Angle Diffraction scan is performed in the same way as a low angle coupled θ/2θ scan, with both the sample and detector being scanned out of the plane of the sample. In the symmetric Bragg geometry the scattering planes are parallel to the plane of the sample and measurements are therefore sensitive to bulk out-of-plane layer structure. An example of an HXRD scan is shown in chapter 7, figure 7.9. Zero order multilayer and satellite diffraction peaks arise as a consequence of the bilayer repeats producing a pseudo lattice structure of large out-of-plane *d* spacing. The absolute position of these diffraction peaks can be calculated from the weighted average of the lattice parameters of the constituent layers via Bragg's law. Comparison of the

calculated and observed peak positions therefore gives a measure of the out-of-plane strain within the deposited layers and a method by which to determine the crystalline texture of a layer. The full width at half maximum of the diffraction peaks gives a measure of the grain size within the layers via the Scherrer equation [41]:

$$D = \frac{0.94\lambda}{\eta \cos\theta} \qquad [2.58]$$

where $D$ is the grain size in Å, $\eta$ the FWHM of the diffraction peak in radians and $\theta$ the Bragg angle corresponding to the peak in question.

The sharpness and number of observed satellite diffraction peaks also gives an indication of the quality of the deposited epitaxial layers, with a loss of higher order peaks observed as a consequence of a reduction in the layer quality and abruptness of the interface. The reader is referred to the following articles for a more comprehensive description (HXRD) [41,42].

## 2.7.2 Grazing Incidence Diffraction (GIXD)

The Grazing Incidence Diffraction technique exploits the inherent depth sensitivity of the evanescent wave that exists for incident beam angles below the critical angle. The detector and sample are scanned in the plane of the film with the diffracting planes perpendicular to the sample plane, as illustrated in figure 2.20. Measurements are therefore sensitive to in-plane crystalline structure and layer quality to a depth of the order of 30-50Å from the sample surface.

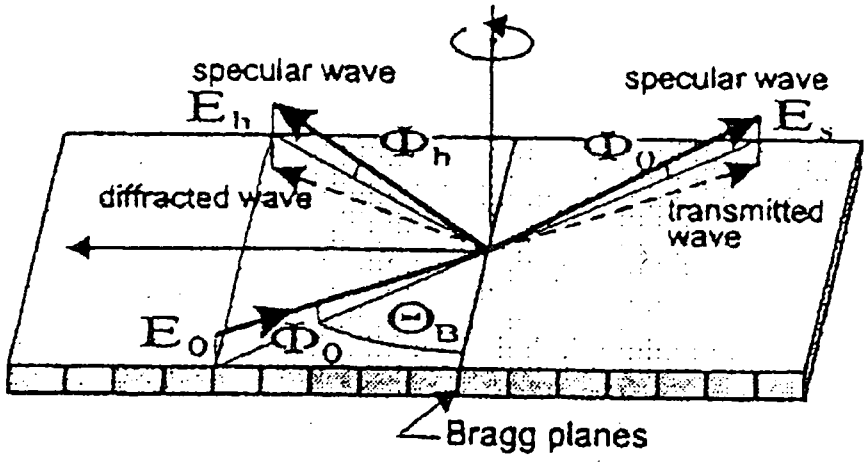


*Figure 2.20. Grazing Incidence Diffraction scan geometry [43].*

An example of a GIXD scan is shown in chapter 7, figure 7.12. In a similar way to the out-of-plane sensitivity of HXRD, it is possible to place an upper limit on the in-plane strain within a system using GIXD by measuring the deviation in position of the diffraction peaks away from the position calculated from the standard bulk lattice parameter. The reader is referred to the following article for a more comprehensive description of (GIXD) [43].

### 2.7.3 Grazing Incidence Fluorescence (GIXF)

Fluorescence measurements detect the photons of characteristic energy that are emitted from an element in which the electrons, initially excited to high energy states by the incident x-ray beam, decay via particular channels, to lower energy states. The depth sensitivity of a beam at grazing incidence combined with the element specific nature of the Fluorescence signal can provide a characteristic elemental depth profile of a system. It is therefore possible to determine the relative quantities of material present, from the associated fluorescence yield, while also being able to retain a sensitivity to where the signal originated. A more detailed description of the use of Grazing Incidence Fluorescence with specific regard to multilayer systems can be found in [44].

## 2.8 Summary and Conclusions

This chapter has presented the theoretical aspects that underpin the interactions of x-rays with matter in low angle regimes. Such processes form the basis of the measurements performed throughout the rest of this study. For a further overview of the discussion presented here the reader is referred to the following review articles [45,46].

## References for Chapter 2


1. M.Kuriyama. Acta. Crystallographica. A 26 56 (1970)

2. M.Kuriyama. Acta. Crystallographica. A 25 588 (1972)

3. M.Kuriyama. Z. Naturforschung 28a 622 (1973)

4. Physics of Atoms and Molecules. B.H.Bransden and C.J.Joachain. Longman (1988)

5. B.K.Tanner. Kinematical Theory of X-ray Diffraction. Lecture notes

6. Theory of X-ray Diffraction in Crystals. W.H.Zachariesen. Dover pub (1994)

7. Neutron and Synchrotron Radiation for Condensed Matter Studies.Vol 1. Eds. J.Baruchel, J.L.Hodeau, M.S.Lehmann, J.R.Regnard, C.Schlenker. Springer-Verlag. (1993)

8. Introduction to Solid State Physics, 6th Edition. C.Kittel, John Wiley & sons (1991)

9. Optics, 2nd Edition. E.Hecht. Addison-Wesley (1990)

10. B.Lengeler. Photoemission and Absorption Spectroscopy in Solids and Interfaces with Synchrotron Radiation. Eds. M.Campagna, R.Rosei. North Holland (1990)

11. The Crystalline State, Vol. 2. The Optical Principles of the Diffraction of X-rays. R.W.James, G.Bell & sons,. (1948)

12. F.Abelès. Ann. Physique (Paris) 5, 596 (1950)

13. L.G.Parratt. Phys. Rev. 95 (2) 359-369 (1954)

14. A.Braslau, M.Deutsch, P.S.Pershan, A.H.Weiss, J.Als-Nielsen, J.Bohr. Phys. Rev. Lett. 54, 114. (1985)

15. L.Névot, P.Croce. Revue Phys. Appl. 15, 761-779 (1980)

16. H.Kiessig. Ann. Phys. (Liepzig) 10 779 (1931)

17. S.K.Sinha, E.B.Sirota, S.Garoff, H.B.Stanley. Phys. Rev. B., 38 (4) 2297-2311 (1988)

18. G.Palasantzas, J.Krim. Phys. Rev.B. 48(5), 2873-2877 (1993)

19. G.Palasantzas, Phys. Rev.B. 48(19), 14472-14478 (1993)

20. G.Palasantzas, Phys. Rev.B. 49(15), 10544-10547 (1994)

21. M.Wormington. Ph.D Thesis, University of Warwick (1999)

22. http://www.bede.com

23. D.K.G.de Boer. Phys. Rev. B 49(9) 5817-5820 (1994)

24. W.Weber, B.Lengeler. Phys. Rev. B. 46(12) 7953-7956 (1992)

25. REFS, Bede Scientific Instruments Ltd (http://www.bede.com)

26. I.Pape, T.P.A.Hase, B.K.Tanner, M.Wormington. Physica B. 253, 278-289 (1998)

27. T.Salditt, T.H.Metzger, J.Peisl. Phys. Rev. Lett. 73(16) 2228-2231 (1994)

28. T.Salditt, T.H.Metzger, J.Peisl, C.H.Morawe, H.Zabel. Mat.Res. Soc. Symp. Proc. 355 269-274 (1995)

29. T.Salditt, T.H.Metzger, G.Goerigk. J. Phys. D. Appl. Phys. 28A 236-240 (1995)

30. T.Salditt, T.H.Metzger, Ch.Brandt, U.Klemradt, J.Peisl. Phys. Rev. B. 51(9) 5617-5627 (1995)

31. T.Salditt, D.Lott,T.H.Metzger, J.Peisl, G.Vignaud, P.Hoghoj, O.Schärpf, P.Hinze, R.Lauer. Phys. Rev. B 54(8) 5860-5872 (1996)

32. Y.H.Phang, D.E.Savage, T.F.Kuech, M.G.Legally, J.S.Park, K.L.Wang. Appl. Phys Lett 60(24) 2986-2988 (1992)

33. E.E.Fullerton, J.Pearson, C.H.Sowers, S.D.Bader, X.Z.Wu, S.K.Sinha. Phys. Rev. B. 48(12) 17432-17444 (1993)

34. A.P.Payne, B.M.Clemens. Phys. Rev. B. 47(4) 2289-2300 (1993)

35. M.Wormington, I.Pape, T.P.A.Hase, B.K.Tanner, D.K.Bowen, Phil. Mag. Lett. 74 211-216 (1996)

36. V.Holý, J.Kubena, I.Ohlidal, K.Lischka, W.Plotz. Phys. Rev. B. 47(23) 15896-15903 (1993)

37. V.Holý, T.Baumbach. Phys. Rev. B. 49(15) 10668-10676 (1994)

38. V.Holý, T.Baumbach, M.Bessière. J. Phys. D. Appl. Phys. 28 A220-226 (1995

39. J.P.Schlomka, M.Tolan, L.Schwalowsky, O.H.Seeck, J.Settner, W.Press. Phys. Rev. B 51(4) 2311-2321 (1995)

40. D.E.Savage, J.Kleiner, N.Schimke, Y.H.Phang, T.Jankowski, J.Jacobs, R.Kariotis, M.G.Legally. J. Appl. Phys. 69(3) 1411-1424 (1991)

41. X-ray Diffraction in Crystals, Imperfect Crystals and Amorphous Bodies. A.Guinier, Dover Pub. (1994)

42. X-ray Diffraction, B.E.Warren. Dover pub (1990)

43. Grazing Incidence X-ray Diffraction. Sergey Stepanov, Autumn School on Synchrotron Radiation, Smolenice (1997)

44. T.P.A.Hase, B.K.Tanner, P.A.Ryan, C.H.Marrows, B.J.Hickey. IEEE Trans. Mag. 34, 831-833.(1998)

45. D.K.G. de Boer, A.J.G.Leenaers, W.W.van den Hoogenhof. X-ray Spectroscopy 24 91-102 (1995)

46. S.K.Sinha. Acta Physica Polonica A. 89 219-234 (1996)

# Chapter 3

# Experimental Aspects of X-ray Scattering and Complementary Structural Characterisation Techniques

## 3.1 Introduction

In this chapter a discussion of the benefits of synchrotron radiation along with a description of the characteristics of the beamlines used in the collection of data discussed in this study will be presented.

All of the data in this study were collected from synchrotron sources at either the SRS, Daresbury or the ESRF, Grenoble. Discussion relating to the use of electron impact devices for the generation of x-rays therefore falls beyond the scope of this thesis and the reader is referred to the following texts for a more detailed description of these types of x-ray sources [1,2].

## 3.2 Synchrotron Radiation

The arrival of large scale synchrotron radiation sources in the 1970's marked a turning point in the use of x-rays as a diagnostic tool in the field of materials science. These large experimental systems have a number of benefits for the user when compared to standard laboratory based electron impact devices such as rotating anodes and sealed tubes. The inherent high photon flux and beam quality, available from synchrotron sources, opened many new avenues of research and made viable experiments that had previously been impossible.

### 3.2.1 Benefits of Synchrotron Radiation

Synchrotron radiation is produced when a charged particle is subjected to a relativistic acceleration. This is achieved in purpose built particle accelerators which all share the same fundamental structure. Charged particles are initially produced and accelerated within a linear accelerator. These particles are then injected into a booster ring where they are accelerated further before final injection into a storage ring. Once injected, the charged particles are confined within this storage ring by means of a series of steering magnets which produce a static magnetic field and control the path of the particle via the Lorentz force [3]. A theoretical discussion relating to the radius of curvature and radiated power of such magnets can be found elsewhere [4,5].

For storage rings designed specifically for the purpose of x-ray production the size of the storage ring is governed by the field strength of the bending magnets and the desired energy of the electrons within the ring. For example, at the Daresbury SRS an energy of 2 GeV is achieved with dipole magnetic fields of 1.2 Tesla, requiring a radius of curvature of 5.56m for the magnets and 15.28m for the entire storage ring [1].

As the electrons orbit the storage ring, under high vacuum conditions, some energy is lost from the beam at each of the bending magnets. This energy is replaced by way of radio frequency, r.f, cavities within the ring with a frequency set to correspond to that of a harmonic frequency of revolution of the charged particles. These r.f cavities operate at a typical frequency of a few hundred MHz with a power of the order of 2MW [2].

The high flux of energetic photons generated by a typical synchrotron source in comparison to an electron impact device is not the sole benefit of using such a facility. An equally important factor is the frequency spectrum and high collimation of the photon beam. In the reference frame of the laboratory the photons generated from the acceleration of the relativistic electrons are Lorentz contracted and confined to an emission cone rather than being emitted into a large solid angle as in the case of a standard dipole. This represents a large increase in the efficiency of synchrotron sources over impact devices as all of the emitted radiation can be utilised due to the excellent vertical collimation. The collimation in the horizontal plane is not as good and depends

primarily on the time the electron is within the confines of the magnetic field generated by the bending magnets [5].

## 3.2.2 The Daresbury SRS

All of the data in chapters 5 and 6 and a large proportion in chapter 7 were obtained from stations 2.3 and 16.3 at the Daresbury Synchrotron Radiation Source. The following section relates specifically to the specification and set up of these beamlines with regard to the data discussed later in this study.

### 3.2.2.1 Station 2.3

Station 2.3 was originally designed as a dedicated Powder Diffraction beamline [6,7] and is equipped with two highly accurate encoded circles. The sample (omega) circle has a resolution of 0.72" and the detector circle a resolution of 0.36" with both axes under independent servo control. It is possible to translate the sample vertically and also to rotate it using a basic chi rotation axis. On a cautionary note the chi and vertical translation motors are not encoded and suffer from a high level of backlash. However, these motors are used only for initial sample alignment, therefore a high degree of positional reproducibility is not essential.

A schematic representation of station 2.3, set up for reflectivity, is shown in figure 3.1. The station is situated 15 metres away, tangentially, from two 1.2 Tesla dipole bending magnets and wavelengths in the range 0.5 to 2.5Å are available. The white x-ray beam is incident onto a water cooled Si(111) monochromator maintained at a temperature of 303±0.1K. This gives a wavelength dispersion of $1.5\times10^{-4}$ at a wavelength of 1.4Å [8]. The post monochromator beam has a typical angular divergence of 7". The x-ray beam is contaminated as a result of the monochromator not being off-set for harmonic suppression, the strongest contaminant arising at $\lambda/3$ from the Si(333) reflection.

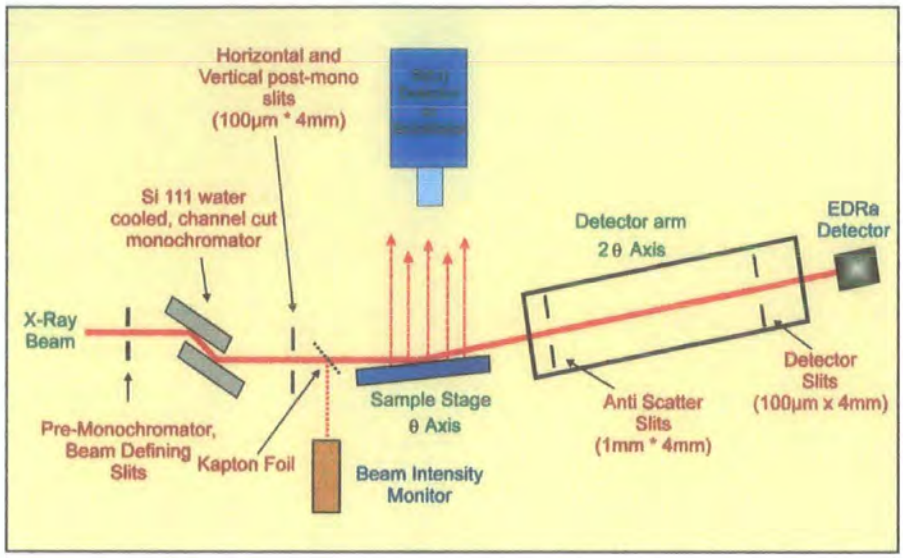


*Figure 3.1. Station 2.3 schematic for reflectivity geometry.*

The beam current immediately after a fill is typically 250mA, decaying to approximately 150mA over an 8 hour period. In order to monitor this beam decay and correct the data, the incident beam intensity is monitored using the scatter from a Kapton™ foil located in the incident beam. The intensity of the incident beam as a function of the wavelength is shown in figure 3.2. Peak flux can be achieved with a wavelength of approximately 1.3Å.

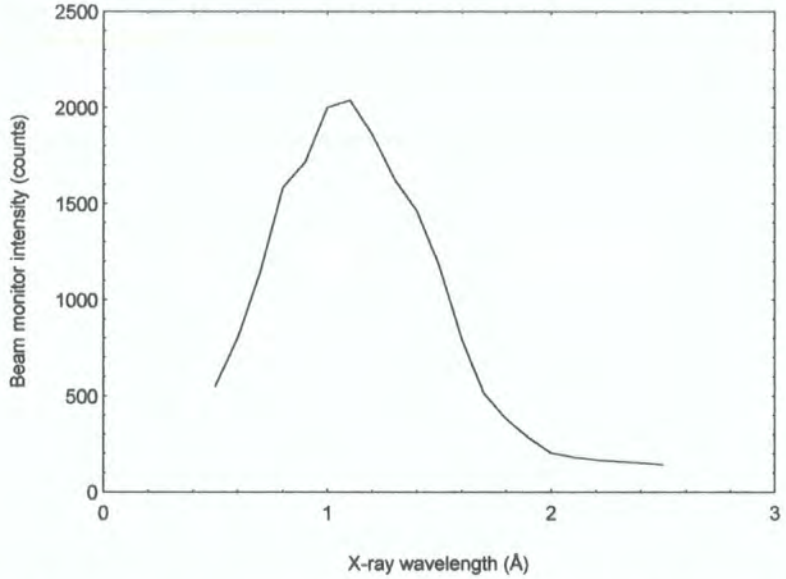


*Figure 3.2. Incident flux as a function of wavelength for station 2.3.*

In order to ensure that any wavelength changes did not effect the position of the incident beam on the sample a set of beam defining slits was positioned after the

monochromator. The instrument resolution is also defined by the geometry of the detector. Analyser slits placed immediately in front of the detector aperture were set to the same height, i.e. out of the plane of the beam, as the incident, beam defining slits. An additional set of 'anti-scatter' slits, typical height of 2mm, were placed on the detector arm close to the sample. Both of these slits on the detector arm were set to a width of 4mm, the consequence of which is very poor resolution in the $q_y$ direction. The slit separation and heights gave a typical angular acceptance of 613" for the detector. To minimise air scatter the beam path between the slits on the detector arm was evacuated. With this experimental arrangement a typical count rate of $10^8$ counts per second was achieved at the sample. A detector scan across the attenuated main beam is shown in figure 3.3. The two sets of slits were set at a height of 100 μm and the incident wavelength set at 1.38Å.

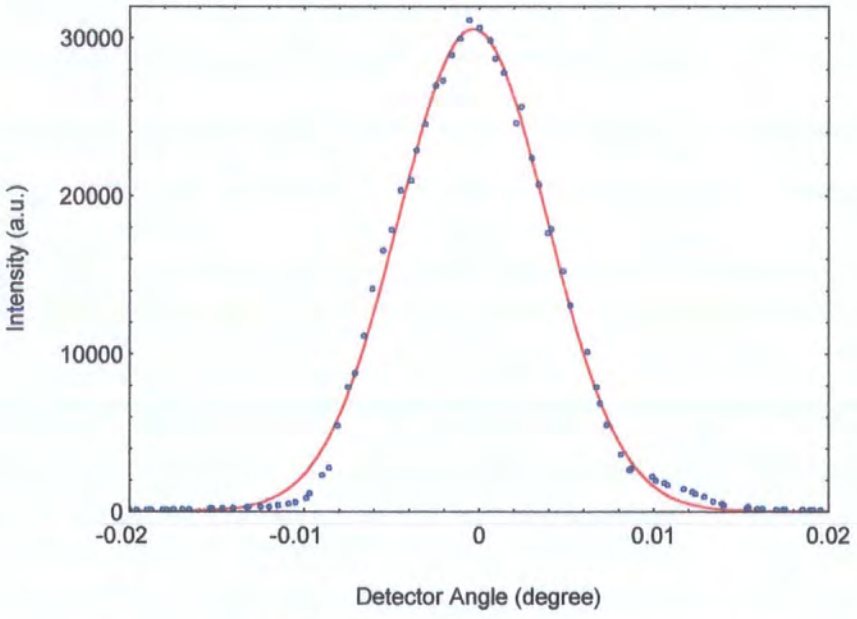


*Figure 3.3. Detector scan through incident beam, λ=1.38Å.*

The beam profile could be fitted to a Gaussian with a full width at half maximum of 43±11" indicating the excellent resolution in this alignment [9].

In order to perform high angle diffraction measurements it can sometimes be advantageous to reduce the instrument resolution. This involves increasing the height of the post monochromator, or analyser, slits or by replacing the two sets of slits that define the acceptance angle with a pair of parallel foils (Soller slits).

One of the most important aspects of synchrotron based measurements is the need for a detector of high dynamic range capable of operating with the high photon flux of a synchrotron source. The most typical choice of detector for such work is the scintillation counter. Scintillation materials, commonly NaI(Tl) is used, produce a pulse of light in response to each x-ray photon absorbed by the scintillation material. This is then amplified and processed via complex electronics. In the high flux regime all paralysable detectors are subject to a dead time correction and follow the relation [10]:

$$R_{measured} = R_{real} \exp(-R_{real} \times \tau) \qquad [3.1]$$

where $\tau$ is the detector dead time. A Bede EDRa detector [11], with a dead time measured to be of the order of 350ns, was used in all of the scattering experiments in this study. The detector has an intrinsic background of 0.15 c.p.s. which was limited experimentally to approximately 1 c.p.s due to air scatter within the experimental hutch. The detector was found to go significantly non-linear for count rates in excess of $4\times10^5$ c.p.s. Even though the dynamic range of this detector is large it was still found to be necessary to attenuate the incident beam when performing measurements at close to zero detector angle. This was achieved by inserting aluminium foils into the beam path. Upon analysis it was found that the attenuated data sets could be scaled accurately to the unattenuated data with no anomalies in the data-set.

In the experiments discussed in chapters 5 and 6 the phenomenon of anomalous dispersion is used to enhance the scattering contrast within the multilayer. In such experiments it was found to be impossible to rely purely on the accuracy of the monochromator calibration when selecting an absorption edge. This accuracy is essential as the variation in the scattering factor difference as a function of wavelength changes rapidly away from an absorption edge, as discussed in chapter 2. In order to locate reproducibly an absorption edge, such as that of copper, it was necessary to record a near edge x-ray absorption fluorescence spectrum (NEXAFS) from a standard sample. Such a spectrum is shown in figure 3.4. The first peak of the spectrum for copper in brass provided a very definite reference point.

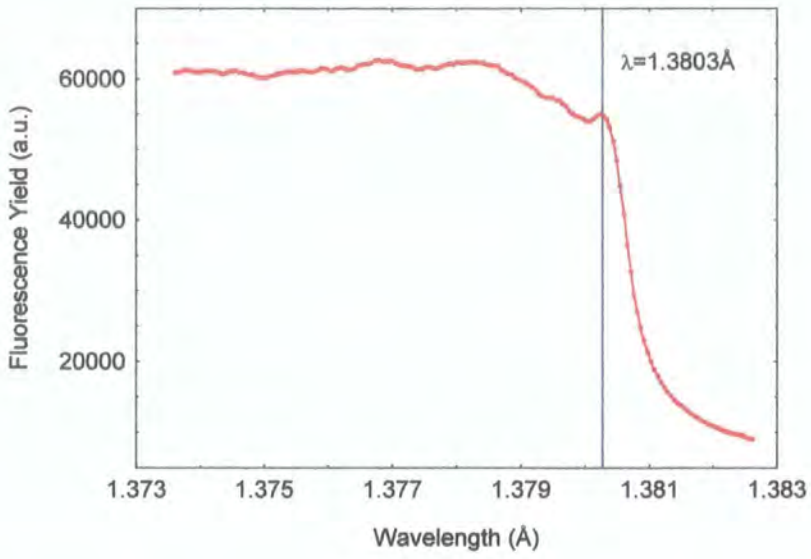


*Figure 3.4. Measured fluorescence yield from Cu in brass as a function of wavelength. The marked line is at λ=1.3803Å [12]*

### 3.2.2.2 Station 16.3

Station 16.3 at the SRS Daresbury is a high energy, high resolution diffraction station equipped with a vertically deflecting, 6 circle diffractometer. The station is situated 32 metres downstream of a wiggler insertion device. A typical photon flux of $10^9$ photons $s^{-1}mm^{-2}$ is available over an energy range of 5 to 25 keV. Double axis diffraction measurements can be performed, as on station 2.3, and can be extended to high resolution triple axis with the addition of a Ge analyser crystal mounted on the detector arm. Station 16.3 also has additional chi/phi rotation circles for the sample stage. A photograph of the diffractometer, showing the chi and phi circles, is shown in figure 3.5.

Initial alignment of the diffractometer and subsequent sample alignment is exactly the same as that for station 2.3 and is outlined in the following section.

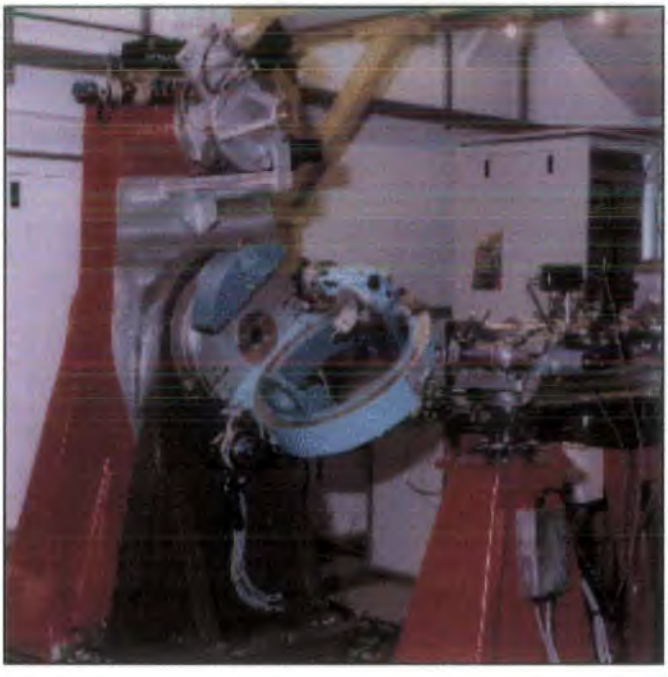

*Figure 3.5. Station 16.3 diffractometer showing the chi and phi circles (blue) [13].*

### 3.2.2.3 Diffractometer and Sample Alignment

The most important factor in aligning the diffractometer is ensure that the sample holder is at the centre of rotation of all of the diffractometer axes that are to be used. By fixing the cross hairs of a telescope on the sample holder and then rotating the omega axis through 180 degrees it is possible to ensure the holder does not move either laterally or vertically. Any adjustments that are required can be made via a goniometer on the sample stage until no observed movement of a reference point on the holder occurs with respect to the telescope cross hairs. This ensures that the alignment is accurate to within approximately 10μm both laterally and vertically. The entire diffractometer is raised or lowered until the sample holder half cuts the incident beam. The position of the diffractometer is then fixed and any further alterations to the sample height are made via the goniometer on the holder until the sample itself half cuts the beam.

Once the diffractometer is aligned it is a relatively trivial process to align the actual sample to the beam. An attenuator is placed in the incident beam and the detector scanned across the beam in order to find the detector zero position. The sample, mounted on the holder is raised into the beam until the beam is half cut. The sample

angle is rocked and the count maximised to ensure that the sample is lying flat to the beam. This position is set as the omega zero point. The detector is driven out to a small angle, typically 2 degrees and any attenuation removed. Small increments to the sample angle are made until the intensity reaches a maximum. At this point the sample angle is set as half of the detector angle. This process is then be repeated at higher scattering angles to verify that the alignment is correct. The entire process assures that the sample is at the centre of rotation of the diffractometer, flat to the beam at zero angle and accurately aligned to the specular condition.

## 3.2.3 The European Synchrotron Radiation Facility, ESRF

The ESRF is a third generation synchrotron radiation source [14] consisting of an 850 metre circumference storage ring fed from a 300 metre circumference booster synchrotron. The booster operates at 6 GeV giving a critical wavelength shorter than that of the Daresbury SRS and more intensity at the higher end of the energy spectrum. The most common mode of operation is that of 2/3 fill with a beam injection current of 200mA. Two beamlines have been used during the course of this study, BM16 and BM28, measurements from which form the bulk of the data discussed in chapter 7.

### 3.2.3.1 Beamline 16 (BM16)

BM16 is similar to station 2.3 in the sense that it is designed as a powder diffraction beamline. However, there are two main differences.

Firstly, at the experimental end of the beamline there is an additional analyser system comprising of nine germanium (111) crystals with a 2 degree separation. This enables true triple axis diffraction measurements to be undertaken although in this study analyser slits were used instead in a high resolution double axis diffraction geometry in order to avoid the loss of intensity associated with an analyser crystal arrangement.

BM16 also differs from station 2.3 in terms of the design of the optical elements. A monochromator, comprising of two Si(111) crystals, is used. One crystal is cooled to dissipate the heat load from the incident beam and the other can be curved to focus sagitally the beam. The focusing is in the horizontal plane of the beam, the vertical angular divergence of which remains unchanged. The beam can be focused vertically to

increase the incident flux at the sample, using a mirror placed further down the line at a cost to the angular resolution. Station BM16 also uses a two circle encoded diffractometer and the diffractometer and sample alignment procedures are identical to those discussed in the previous section.

### 3.2.3.2 X-ray Magnetic Scattering Beamline (XMaS), BM28

The XMaS beamline [15] became operational in the spring of 1998 and was designed to perform magnetic and high resolution experiments with an available energy range of 3 to 15 keV. An optics system consisting of a double crystal monochromator followed by a toroidal focusing mirror is used on the beamline. The monochromator consists of two, plane silicon crystals with a mirror made from a single crystal of silicon with a cylindrical cross section of 116nm, sagital focus. Toroidal focus is obtained with the addition of a small tangential cylindrical curvature, radius 5.5 km, and is produced using a pneumatically driven bending mechanism. The incident beam is focused to a small spot on the sample surface via this toroidal mirror system. A maximum flux of the order of $10^{12}$ c.p.s is possible from a fan of radiation of 3.1 and 0.2 milliradian divergence in the horizontal and vertical plane respectively.

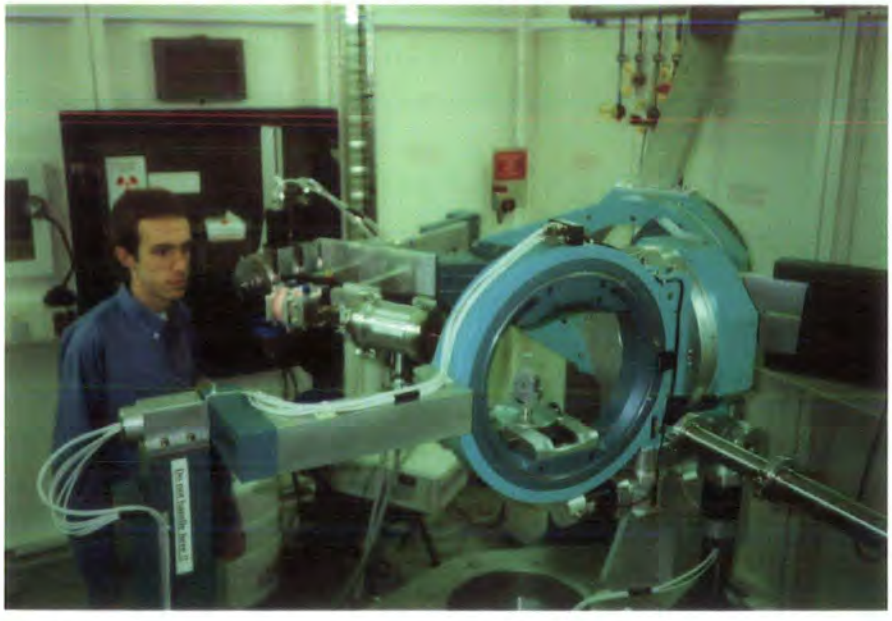

*Figure 3.6. The 11 axis diffractometer on the XMaS beamline set up for scanning in the horizontal plane.*

An 11 axis Huber diffractometer is located within the experimental hutch with computer control that can accept four encoded circles in either the vertical or horizontal plane. The horizontal axes allow grazing incidence diffraction measurements to be performed, in addition to reflectivity and high angle diffraction measurements performed in the vertical plane. Once again, the sample and diffractometer alignment procedures are fundamentally the same as those outlined in section 3.2.2.3 although an initial degree of beam steering is required if full toroidal focusing is to be used. A photograph of the Huber diffractometer is shown in figure 3.6.

## 3.3 Complementary and Additional Techniques

A selection of various experimental techniques have been used, or are discussed, in this study and fall into two main categories. Firstly, although the majority of all of the structural characterisation of these multilayer systems have been carried out using x-ray scattering, other complementary techniques such as High Resolution Transmission electron Microscopy (HR-TEM) and Transmission Electron Diffraction (TED) have also been used by collaborators.

Secondly, the magnetic behaviour of theses sample is of course crucial in any study relating to their GMR properties. The magnetic measurements presented in this work were undertaken by D.E. Joyce (chapters 5 and 6), and P.A. Ryan (chapter 7) and are referenced in the appropriate sections. Polarised Neutron reflectivity (PNR) measurements, undertaken by D.E. Joyce, are sensitive to both structure and magnetisation in multilayer structures and are discussed in relation to Co/Cu in Chapter 5. Magnetic measurements have been made using Alternating Gradient Field (AGFM) or Vibrating Sample (VSM) Magnetometers with all resistivity measurements being made via a standard 4 point probe method.

In this section a very brief overview of the fundamental principles involved in the HR-TEM and PNR techniques will be presented. The reader is referred to the work of Brundle *et al.* [16] for a more detailed description of various characterisation techniques.

### 3.3.1 Transmission Electron Microscopy and Diffraction

HR-TEM measurements are sensitive to the many buried interfaces in a multilayer stack in a similar way to x-ray scattering techniques. It is therefore possible, from a cross sectional HR-TEM image, to study the nature of any interface structure. However, as with any microscopy technique, HR-TEM provides only a very localised picture and it is not possible to globally average over the micron length scales of x-ray measurements. Further to this, TEM measurements differ from those of x-rays in that they are not non-destructive and require time consuming sample preparation. However, HR-TEM measurements are useful in providing an independent method with which to visualise interface structures.

In HR-TEM electrons are generated, typically by a hot filament, and accelerated through a potential difference. The electron beam passes through a series of magnetic lenses, and the condensed and collimated beam projected through a suitably prepared, thin sample. A thin sample is required due to the high scattering and low penetration depth of the electrons. The scattered beam is then magnified and imaged on a screen or photographic plate. The system can be run in defocused mode in order to enhance the phase contrast between adjacent layers of a multilayer system, thereby improving the layer structure definition. The HR-TEM instrument can easily be converted, by suitable positioning of the intermediate lens, to run in diffraction mode (TED). In this mode it is the Fourier transform of the image that is projected onto the screen. These reciprocal space images can be used to determine the microcrystalline structure of the sample.

### 3.3.2 Polarised Neutron Reflectivity (PNR)

Neutron reflectivity measurements differ from those of x-ray reflectivity in two main areas. Firstly the neutron scattering amplitudes of the elements do not vary as a monotonic function of atomic number and instead vary erratically from element to element. Secondly, in the case of neutrons, there is a magnetic contribution to the refractive index of a material in addition to the nuclear one. This means that for materials magnetised in the plane of the sample, neutrons polarised either parallel or antiparallel to the applied field will have a spin-dependent refractive index. Neutron reflectivity can therefore be used as a very sensitive probe of magnetisation with depth.

## References for Chapter 3

1. X-ray Science and Technology, EDS. A.G.Michette and C.J.Buckley, IOP Publishing, (1993)

2. Wen-Jih Lin, Ph.D Thesis, University of Edinburgh (1998)

3. Solid State Physics, International Edition. Ashcroft and Mermin, (1976)

4.Neutron and Synchrotron Radiation for Condensed Matter Studies Vol 1., Eds. J. Baruchel, J-L.Hodeau, M.S.Lehmann, J.R.Ragnard and C.Schlenker, Springer-Verlag (1993)

5. G.Margaritondo, Journal of Synchrotron Radiation, 2, 148-154, (1995)

6. C.C.Tang, M.Miller, D.Laundy. Station 2.3 User Manual, CLRC Daresbury

7. C.C.Tang, S.P.Collins, B.M.Murphy, N.D.Telling, R.A Wogelius, S.J.Teat. Review of Scientific Instruments. Vol.69, No. 3

8. R.J.Cernik, P.K.Murray, P.Pattison, A.N.Fitch. J. Appl. Cryst. 23. 292-296 (1990)

9. B.K.Tanner, D.E.Joyce, T.P.A.Hase, I.Pape, P.J.Grundy. Adv. X-ray Analysis, 41 (1997)

10. D.R.Beaman, J.A.Isasi, H.K.Birnbaum, R.Lewis. J. Phys. E: Sci. Inst 1, 5, 767-776 (1972)

11. S.Cockerton, B.K.Tanner. Advances in X-ray analysis, Vol. 38, (1995)

12. B.K.Tanner, D.E.Joyce, T.P.A.Hase, I.Pape P.J.Grundy. Adv. X-ray Analysis 40 (1997)

13. http://www.dl.ac.uk/SRS/XRD/16.3.dir/

14. http://www.esrf.fr

15. http://www.esrf.fr/cgi-bin/Beamline

16. C.R.Brundle, C.A.Evans Jr., S.Wilson, Encyclopedia of Materials Characterisation: Surfaces, Interfaces and Thin Films. Butterworth- Heinemann

# Chapter 4

# Magnetic Multilayer Systems

## 4.1 Introduction

After the experimental observation of the phenomenon of giant magneto-resistance (GMR) [1,2] in layered systems, magnetic multilayer structures became a rapidly developing area of solid state research in the late 1980's. These structures, typically consisting of very thin, alternating layers of magnetic and non-magnetic material, can exhibit very different magnetic properties from those of their bulk constituents and have come to provide many novel applications in the field of magnetic sensors and data storage [3].

The aim of this chapter is to give the reader an overview of magnetic multilayer structures and the processes behind the Giant Magneto-Resistance effect. Firstly, the two principle methods of multilayer growth will be discussed briefly. The fundamental aspects regarding the mechanism behind the GMR effect will then be presented with particular regard to oscillatory exchange coupling and bulk and interface scattering.

## 4.2 Multilayer Fabrication

The two main methods of multilayer growth, corresponding to the two methods by which samples discussed in this study were grown, are Sputtering and Molecular Beam Epitaxy (MBE).

### 4.2.1 Growth by Sputtering

In the sputter deposition process, near surface atoms are ejected from a selected target material due to the bombardment of that target by energetic ions, as illustrated schematically in figure 4.1. The actual deposition of the target atom onto a selected substrate is a three stage process. Atoms, incident from the sputtering target onto the

substrate or layer, transfer their kinetic energy to the lattice and become loosely bonded to it. These atoms then diffuse across the surface to an extent determined by their surface mobility, which is dependent upon the ratio of the surface temperature to the melting point of the atomic species involved. This process continues until the atom is either removed from the surface, by evaporation or further sputtering, or becomes trapped in a low energy lattice site and is incorporated into the surface. In the final stage, the atoms rearrange their position in the lattice through bulk diffusion.

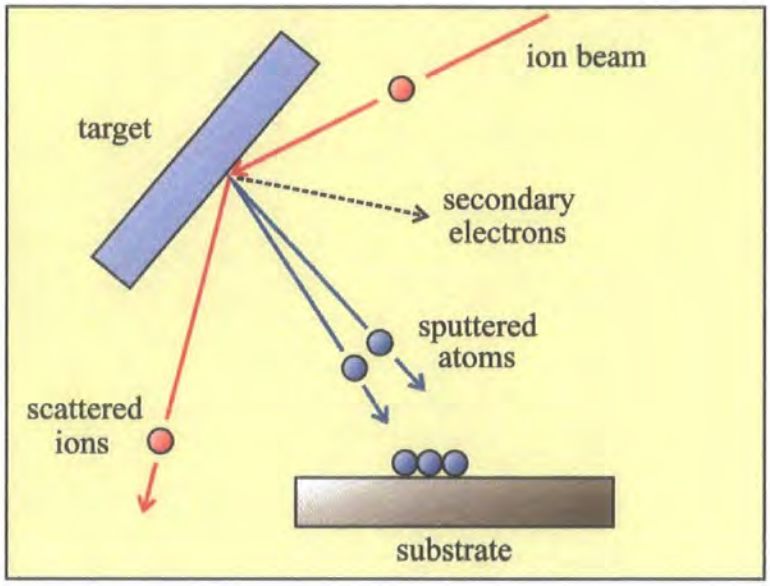


*Figure 4.1. Schematic representation of the sputter deposition process.*

The sputtering yield, the rate at which the target material is deposited onto the substrate, is dependent upon the energy of the sputtering beam and the binding energy of the target material. Typically the deposition process occurs under an argon atmosphere. The sputtering pressure of the argon in the chamber, along with the surface temperature of deposition, can have a profound effect on the morphology of the deposited film. All factors relating to sample deposition are described in various structural models to which the reader is referred for more specific details [4-7].

It is possible that the sputtering process can reduce the roughness of a surface due to erosion effects, especially if the sputtered ions are incident at oblique angles. Roughness features with an enhanced profile on the surface are preferentially removed leading to a general smoothing of the surface. However, it is also possible to roughen an

already smooth surface due to fluctuations in the incident flux and this can also reduce the sputtering yield. In general, sputter deposited layers tend to have high values of fractal dimension, typically $h \approx 0.6$ to 1 [8].

### 4.2.2 Molecular Beam Epitaxy

Molecular Beam Epitaxy involves the condensation of a vapour beam, produced from a Knudsen cell [9], of one material onto another under ultra high vacuum conditions. The use of UHV minimises the amount of background impurities that are incorporated into the film and also allows the use of in-situ electron beam characterisation techniques to monitor the deposited film. Vapour flux from thermal sources, typically crucible sources or electron beam heated metal charges, provides the source of atoms for deposition.

The principle advantage of MBE over sputtering is that it allows materials to be deposited in such a way that retains high levels of atomic registration between adjacent layers. This routinely allows the growth of very thin layers of high epitaxial quality with inherently smooth interfaces of low fractal dimension, typically $h \approx 0.2$ to 0.3 [8]. When depositing a selected material onto a substrate a high degree of lattice match is required for successful epitaxial deposition. In some cases, such as Fe/Au grown on sapphire, it is necessary to deposit a buffer layer onto the substrate, in this case niobium, prior to the deposition of the multilayer itself. A more detailed description of the MBE system at the University of Leeds, used to grow the samples discussed in chapter 7, can be found in recent Ph.D theses [10,11]. The reader is also referred to the following review article for a discussion of the contribution of MBE grown materials to the study of GMR [12].

## 4.3 Giant Magneto-Resistance (GMR)

The first experimental observation of the processes involved in the GMR effect were made in a series of Fe-Cr-Fe trilayers. Binasch *et al.* [1] and Baibich *et al.* [2] noted that for a Cr layer thickness of the order of 10 Å the two magnetic moments in the Fe layers were aligned in opposite directions, an antiferromagnetic (AF) coupling arrangement. This Cr thickness corresponded to that found in earlier work by Grunberg *et al.* [13] in which it was found that AF coupling only occurred for specific Cr layer thicknesses.

It was already known that in many ferromagnetic materials an anisotropic effect occurred, on the application of a magnetic field, due to the different resistance experienced by a current flowing parallel or perpendicular to a magnetisation direction. However, a standard anisotropic magneto-resistance (AMR) effect alone was not of sufficient magnitude to explain the resistance change in these Fe-Cr-Fe trilayers. The large change in the multilayer resistance was termed 'Giant' Magneto-Resistance and was thought to be related to the observed antiferromagnetic alignment of the magnetic moments in the two Fe layers. It was proposed [1,2] that spin flip scattering due to the antiferromagnetic coupling was responsible for the effect, although the origin of this coupling remained unclear.

The observation of antiferromagnetic exchange coupling with an associated GMR effect triggered a huge increase in the study of these thin layer magnetic systems. Baibich [2] observed that in the Fe/Cr system the resistivity was reduced by a factor of 2 when the coupling was changed from AF to F by the application of a large external field.

The suggestion of spin-dependent scattering processes was supported by the theoretical work of Camley and Barnas [14]. A model, an extension of the Fuchs-Sondheimer theory [15,16], was proposed that introduced spin-dependent coefficients for the scattering in a multilayer. Camley and Barnas were able to address the observations that the resistance in Fe/Cr multilayers decreased when the coupling changed from antiferromagnetic to ferromagnetic and that the structures containing many thin Fe films had a much larger magneto-resistance effect than a single Fe-Cr-Fe sandwich.

In the original work by Baibich [2] is was reported that the magneto-resistance in the Fe/Cr multilayer would decrease monotonically with increasing Cr thickness. In 1990, Parkin *et al.* [17] found that this was not the case and that, although there was a general decrease, the MR did in fact oscillate as a function of Cr thickness. In the same work it was reported that two other systems, Co/Cr and Co/Ru, exhibited similar oscillatory behaviour. As more research was carried out into viable multilayer systems it was found that Co/Cu [18-20], Fe/Ag and Fe/Al [21,22] also exhibited oscillatory MR and saturation field characteristics. In 1991 oscillatory exchange coupling in multilayer

systems was found to be widespread for all transition metal spacer layers [23], the main prerequisite being that for a material to be suitable for use as a spacer layer the mean free path of an electron in that layer must be considerably larger than the layer thickness

### 4.3.1 Oscillatory Exchange Coupling

The oscillatory exchange coupling observed in magnetic multilayer systems arises as a consequence of an indirect exchange interaction. This type of interaction was originally developed to explain the interaction between the nuclear spins of impurities contained within a metallic host.

It is possible to extend this idea to a multilayer system in which the non-magnetic spacer layer becomes the host and the interfaces in the structure are the perturbation within that host. Conduction electrons within the non magnetic spacer re-arrange their position in order to screen out the impurity, or in this case the interface generated perturbation.

This type of interaction was predicted by Rudderman, Kittel, Kasuya and Yosida (RKKY) [24-26]. For a magnetic atom in a non magnetic host, for example a Co atom in a Cu spacer, the magnetic moment on the atom induces a polarisation in the nearby conduction electrons. The net result is an oscillation in the spin density of the electrons. A second magnetic atom will then experience either a positive or negative polarisation leading to either a ferromagnetic or antiferromagnetic interaction between neighbouring magnetic layers. The strength of the RKKY interaction is proportional to $d^{-3}$, where $d$ is distance between the magnetic atoms. In the multilayer case the thickness dependence of the coupling between neighbouring magnetic layers exhibits a $d^{-2}$ dependence due to the effectively one-dimensional nature of the multilayer.

Although the RKKY interaction does indeed predict the oscillatory exchange observed experimentally, it was found that the period of oscillation predicted from the RKKY model [27] was too short. When an aliasing term was introduced into the model, [28] to account for the periodic nature of the lattice structure, this discrepancy could be accounted for as short period oscillations between lattice points generated a beating effect of a longer period.

Bruno and Chappert [29] developed the model further and found a method by which to calculate accurately the long period oscillations for many different spacer thicknesses, all in good agreement with experimental observation. An example of the oscillatory nature of the exchange coupling is shown in figure 4.3. The inset hysteresis loops show the coupling to vary from ferromagnetic (upright curves) to antiferromagnetic as the spacer thickness changes. It should be noted that close to a coupling maximum a large change in coupling strength can occur for only small variations in spacer thickness, illustrating the need for accurate film deposition techniques.

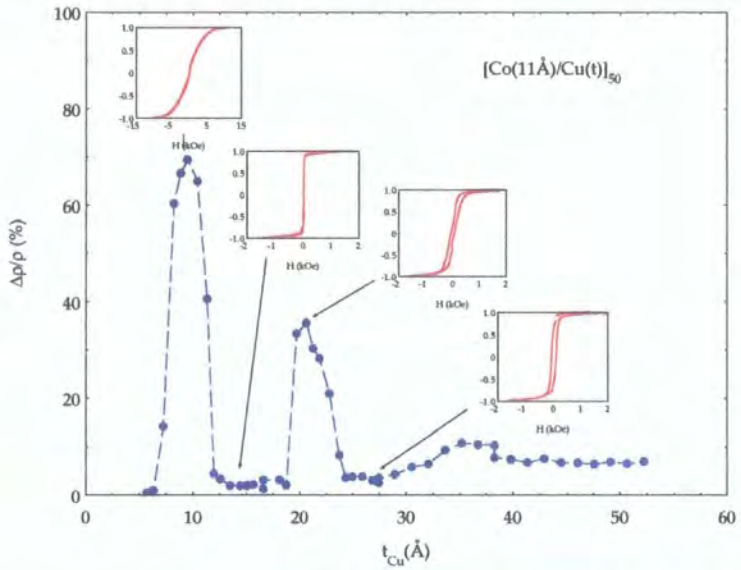


*Figure 4.3. Oscillations in GMR as a function of Cu spacer thickness due to variations in the coupling [30].*

The thickness of the magnetic layer is also important as this effects the relative fraction of bulk and interface scattering and is discussed in chapter 5 with regard to Co/Cu.

### 4.3.2 Spin-dependent Scattering Processes

Any disorder within a system will lead to an increase in the electrical resistance of that system purely due to the scattering, and subsequent reduction in the mean free path, of the conduction electrons. In magnetic multilayers this scattering can be of a spin-dependent nature and this is what gives rise to the GMR effect.

Within a multilayer the current can be thought of as being carried in two, independent 'spin channels', one for spin up electrons (spin parallel to magnetisation direction) and one for spin down electrons (spin antiparallel to magnetisation direction). In a ferromagnet, which is assumed to be below the temperature of spontaneous magnetic ordering, the spin flip scattering process can be assumed to be negligible and the spin of the electron is conserved after each scattering event. The sp-electron band is broad in nature, and therefore has a low effective mass [31], so it is these, more mobile, electrons that are the main charge carriers. The d-bands have a much higher density of states and are of higher effective mass. These d bands states are still crucial to the GMR effect because they provide the necessary empty states for the electrons to scatter into. Conservation of electron spin means that spin up electrons can only scatter into spin up s and d states, and of course the converse situation applies. The actual resistance of the material is primarily dependent on the density of states in the d-band because the scattering is principally s-d scattering due to the much higher density of states in the d band. The spin dependent nature of the density of states in a ferromagnetic metal is illustrated in figure 4.4.

In the ferromagnetically coupled case the spin up electron band is below the Fermi energy, $E_f$, in both magnetic layers and is therefore completely filled. The spin down band, however, is only partially below the Fermi energy. In the antiferromagnetic case the spin up band is completely filled in one magnetic layer but only partially filled in the other and vice versa.

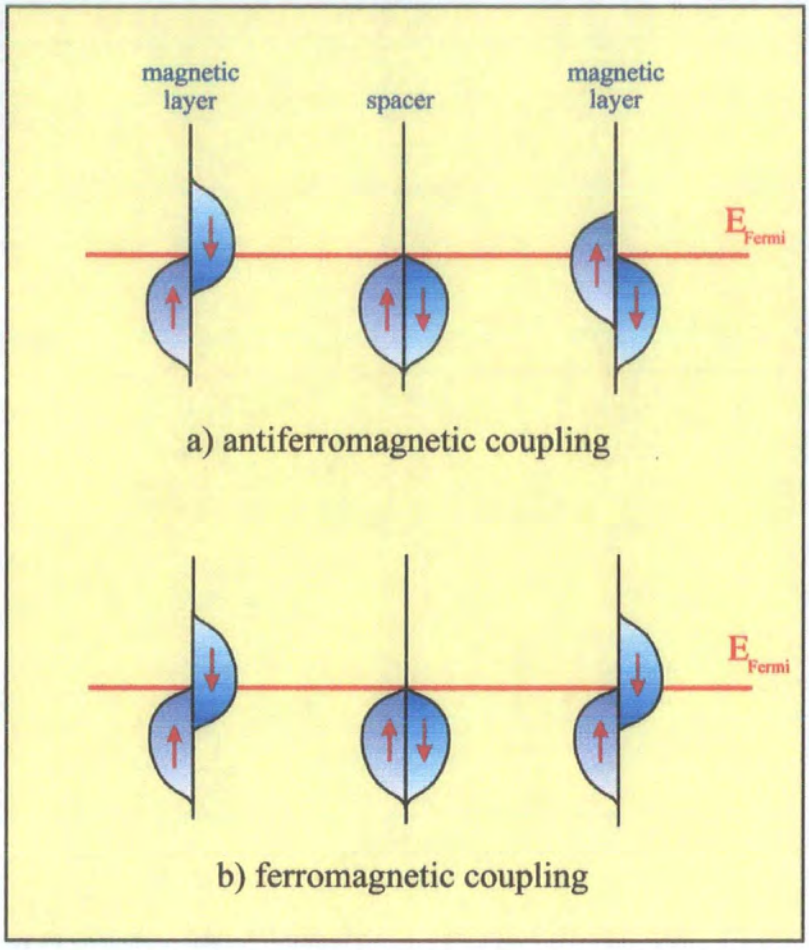


*Figure 4.4. Representation of the density of states in an antiferromagnetically and ferromagnetically coupled sample.*

Within the non-magnetic spacer layer the density of states does not depend on the electron spin, the resistivity of each spin channel is equal and both bands are below the Fermi level. It is only once the electron is within the magnetic layer that spin-dependent scattering becomes important.

A spin up electron will experience little spin dependent scatter in layers where it is the majority spin electron, and will have a consequently larger mean free path, than in layers where it is the minority spin carrier. The spin dependent scattering process is illustrated schematically in figure 4.5.

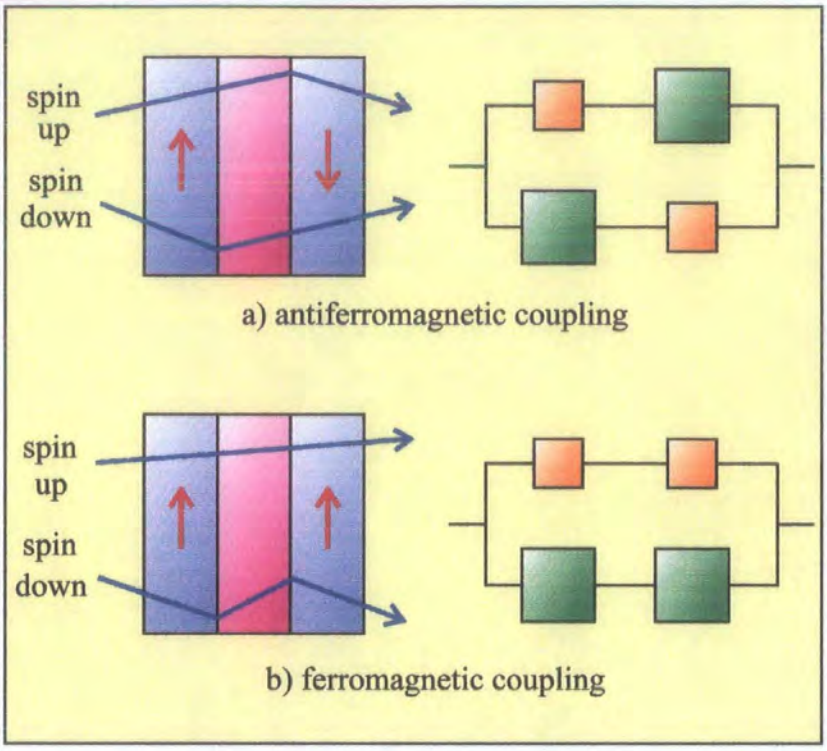


*Figure 4.5. Spin dependent scattering for spin up and down electrons in an antiferromagnetically a) and ferromagnetically b) coupled sample. The equivalent resistor model is shown alongside.*

In the ferromagnetically coupled state one spin orientation, spin down in the diagram, will always be the minority carrier and will scatter strongly whenever it crosses a layer boundary as a consequence of the high scattering potential generated by the energy shift of the spin down band shown in figure 4.4. In contrast to this, the spin up electron will always be majority spin carrier in all magnetic layers and therefore possesses a much larger mean free path. For antiferromagnetic alignment one particular electron spin will alternate between minority and majority spin carrier as it traverses the multilayer. The equivalent resistor model for the AF and F coupled multilayers [32] is also presented in figure 4.5, clearly showing that the net resistance of the system will be lower for ferromagnetic alignment of adjacent magnetic layers.

### 4.3.3 Structural Considerations

The above argument was formulated from an assumption that the difference in the resistivity arose from differences in the bulk scattering in the ferromagnetic layers. However, the GMR effect can be explained from the same argument regardless of

where the spin-dependent scattering occurs. In Fe based systems there is very little difference in the density of states at the Fermi energy for the two types of carrier, and it is therefore valid to assume that in these types of systems the GMR effect does not depend on bulk scattering to any great extent. Spin-dependent scattering processes can occur both within the bulk of a ferromagnetic layer and at the interface between this layer and the non-magnetic spacer. Indeed it is known that interface scattering is also a very important factor in the GMR process [33]. Recent studies [34] have shown that even when only the bulk scattering in a system is considered, the minority spin electrons are mainly scattered within a very thin layer close to the interface with the non-magnetic layer. This means that in some structures, the GMR can be largely influenced by the interface structure. The importance of the region close to the magnetic/non-magnetic interface was also demonstrated by Parkin [35] who illustrated the potentially large effect on GMR of inserting additional thin magnetic layers at the interfaces of the multilayer structure.

The crystallographic orientation of the system can also play an important role as this influences the density of states and oscillatory coupling. Theoretical studies with regard to the oscillatory dependence of the GMR on the spacer thickness [36] suggest that the effect should be stronger for films oriented away from the {111} direction. In agreement with this, Egelhoff *et al.* [37] found that multilayers, grown by MBE on Cu (111), exhibited no oscillatory coupling while those grown on Cu (100) did and suggested that the coupling observed in sputter deposited multilayers grown on Cu (111) was due to a (100) oriented component. However, other studies have contradicted this [38] with strong arguments coming from the disparity between samples grown by sputtering and MBE.

In summary, it is clear that the GMR effect is dependent upon the nature of the coupling between adjacent magnetic layers in a multilayer. The coupling is determined by the RKKY exchange interaction and oscillates as a function of the thickness of the non magnetic layer. Giant Magneto-Resistance arises from the spin-dependent scattering of electrons in two distinct spin channels with the magnitude of the effect determined by the amount of bulk and interface scattering. The dependence of the GMR on crystallographic and structural perturbations and imperfections in multilayers is also clear.

## References for Chapter 4


1. G.Binasch, P.Grunberg, F.Saurenbach, W.Zinn. Phys. Rev. B. Vol 39, No.7 (1989)

2. M.N.Baibich, J.M.Broto, A.Fert, F.Nguyen Van Dau, F.Petroff, P.Etienne, G.Creuzet, A.Friedrich, J.Chazelas. Phys. Rev. Lett. 61, 2472 (1998)

3. http://www.research.ibm.com/research/gmr.html

4. B.A.Movchan, A.V.Demchishin. Phys. Met. Metal. USSR 28 (4) (1969)

5. J.A.Thornton, Ann. Rev. Mater. Sci. 7. (1977)

6. D.W.Hoffman and J.A.Thornton. Thin Solid Films 45, (1977)

7. R.A.Roy and R.Messier. J.Vac. Sci. Technol. A2, page 312 (1984)

8. Fractal Concepts in Surface Growth. A.L.Barabasi, H.E.Stanley. Cambridge Press (1995)

9. Mike Wells. Thin Films - MBE. IOP Conference Seminar (1998)

10. M.J.Hall, Ph.D Thesis, University of Leeds (1993)

11. N.J.Flynn, Ph.D Thesis, University of Leeds (1996)

12. R.F.C.Farrow. IBM, J. Res. Development. Vol 42, No.1 (1998)

13. P.Grunberg, R.Schreiber, Y.Pang, M.B.Brodski, H.Sowers. Phys. Rev. Lett. 57. 2442 (1986)

14. R.E.Camley, J.Barnas. Phys. Rev. Lett. (63) 6, 664 (1989)

15. K.Fuchs. Proc. Cambridge Philos. Soc. 34, 100 (1938)

16. E.H.Sondheimer, Adv. Phys 1, 1-42 (1952)

17. S.S.P.Parkin, N.More, K.P.Roche. Phys. Rev. Lett (64) 19 2304 (1990)

18. S.S.P.Parkin, R.Bhadra, K.P.Roche. Phys. Rev. Lett (66) 2152 (1991)

19. S.S.P.Parkin, Z.G.Li, D.J.Smith. Appl. Phys. Lett. 58, 2710 (1991)

20. D.H.Mosca, F.Petroff, A.Fert, P.A.Schroeder, W.P.Pratt Jr, R.Laloee. J.Magn. Magn. Mater. 94, L1, (1991)

21. J.J.de Miguel, A.Cebolada, J.M.Gallego, R.Miranda, C.M.Schneider, P.Schuster, J.Kirschner. J.Magn.Magn.Mater, 93, 1-9 (1991)

22. A.Fub, S.Demokritov, P.Grunberg, W.Zinn. J.Magn.Magn.Mater, 103, L221-277 (1992)

23. S.S.P.Parkin, Phys. Rev. Lett. 67 (25) 3598-3601, (1991)

24. M.A.Rudderman and C.Kittel, Phys. Rev. 96, 99 (1954)

25. T.Kasuya, Prog. Theoret. Phys. (Kyoto) 16, 45 (1956)

26. K.Yosida, Phys. Rev. 106, 893 (1957)

27. Y.Yafet. Phys. Rev. B. 36, 3948 (1987)

28. R.Coehoorn, Phys. Rev. B. 44, 9331 (1919)

29. P.Bruno, C.Chappert. Phys. Rev. B. 46 Vol 1. 261 (1992)

30. C.H.Marrows, N.Wiser, B.J.Hickey, T.P.A.Hase, B.K.Tanner. J.Phys. C. 11 81-88 (1999)

31. Introduction to Solid State Physics. C. Kittel. 6th edition. Wiley (1991)

32. J.Mathon, Contemporary Physics. Vol. 32, No.3 pages 143-156 (1991)

33. R.Q.Hood, L.M.Falicov, D.R.Penn. Phys. Rev. B. Vol. 49 1 (1994)

34. C.Prados, D.V.Dimitrov, G.C.Hadjipanayis. J. Magn. Magn. Mater. 192 19-26 (1999)

35. S.S.P.Parkin, Phys Rev. Lett. 71 (10) (1993) 1641

36. P.Bruno, C.Chappert. Phys. Rev. Lett. 67, p1602 (1991)

37. W.F.Egelhoff, M.T.Kief. IEEE Trans. Magn. 28, p 2742 (1992)

38. D.Greig, M.J.Hall, C.Hammond, B.J.Hickey, H.P.Ho, M.A.Howson, M.J.Walker, N.Weiser, D.G.Wright. J. Magn. Magn. Mater 110 L239 (1992)

# Chapter 5

# Structure, Texture and GMR in Sputtered Co/Cu Multilayers grown on Etched Silicon

## 5.1 Introduction

Multilayers grown from cobalt and copper formed one of the first magnetic systems in which the phenomenon of Giant Magneto-Resistance (GMR) was observed [1-3]. From the initial discovery of GMR [4] the aim of researchers has been to maximise the GMR effect by establishing a detailed understanding of the dominant factors that drive the process. In chapter 4 the way in which GMR arises due to spin-dependent scattering processes within a multilayer structure was described, along with a description of how these scattering events are influenced by the structure and crystallographic texture of the multilayer system.

This chapter is concerned with extensive work performed, on a series of Co/Cu multilayers grown on etched silicon, in collaboration with the University of Salford. The aim has been to study the effect of substrate etching voltage on the magnetic, crystalline and interfacial properties of the subsequently modified polycrystalline sputter deposited Co/Cu multilayers.

Grazing incidence x-ray scattering has been used to characterise fully the structure and growth morphology of these systems. This technique has the added advantage of being able to probe the many buried interfaces within a multilayer stack. High angle diffraction techniques have also been used in order to study the bulk crystallographic texture of the multilayers.

X-ray scattering data has been consolidated with that from other techniques, such as Polarised Neutron Reflectivity (PNR) and Transmission Electron Microscopy (HR-TEM), in order to relate the multilayer structure to the magneto-transport

processes in these etched Co/Cu systems, in an attempt to determine the overriding factors controlling the size of the GMR effect in such systems.

## 5.2 The Samples

Films with a nominal structure of 16 x {10Å Co / $X$ Å Cu} + 10Å Pt were grown, by D.E. Joyce, on ion beam etched silicon (100) wafers using the d.c magnetron sputtering technique described in chapter 4. Two types of sample were grown with $X$ = 10Å for type A samples and $X$ = 20Å for type B samples. The thinner, type A, samples are advantageous in TEM studies and were also used in the x-ray scattering measurements. The thicker, type B, samples were used in the PNR studies, due to their lower saturation fields, and in the GMR measurements where the reproducibility of the Cu thickness across the series is crucial. The Cu spacer layer thicknesses were chosen to sit at the first (type A) and second (type B) antiferromagnetic (AF) coupling peak in the GMR versus spacer thickness curve [5,6], an example of which is shown in figure 4.3.

Although the coupling at the second maximum is weaker than at the first the thicker Cu layer allows a greater degree of reproducibility when growing the samples, especially in samples which may possess rough interfaces. Selecting a thicker Cu layer also reduces the likelihood of ferromagnetic bridging [7-10] across the Cu layer, due to defects such as pinholes, which can occur in systems with thin Cu layers of the order of 8Å or less, and would in turn reduce the degree of AF coupling. Although the likelihood of pinhole defect formation is reduced in sputter deposited samples due to the high surface temperature of deposition and increased surface mobility of the deposited atoms, thereby reducing the possibility of defect formation, it is still advantageous from a precautionary standpoint to grow a Cu layer of thickness greater than 8Å.

The base pressure in the sputtering chamber was better than $10^{-5}$ Pa [11]. The deposition rates at room temperature and under an Argon pressure of 0.4 Pa were 0.4Å, 0.7Å, and 0.8Å per second for Co, Cu and Pt respectively. Before deposition the substrates were etched for 2 minutes using a Kaufman type ion source under a 0.1 Pa Argon pressure at varying beam voltages up to 1 kV. All substrates were known to have

a native $SiO_2$ layer and for reference the multilayer grown directly, without etching, onto this oxide layer will be called "unetched". For further details on the etching process the reader is referred to the thesis of D.E. Joyce [12].

## 5.3 Substrate Etching

The etching of silicon substrates prior to the deposition of the multilayer is known to be a very effective method by which to control the crystalline orientation of sputter deposited samples [6]. Other methods for controlling texture involve varying the argon gas pressure within the sputtering chamber, however at low argon pressures neutral particles possessing energies of several hundred electron volts can also bombard the sputtered film. The high energy of the neutral particles impinging on the surface is a consequence of the energy loss due to scattering in the sputtering gas being weak in this low pressure regime. The net effect of a low Ar pressure is to roughen the interfaces within the stack [13-17]. For this reason previous studies [18,19], in which the sputtering pressure has been altered to vary the crystallinity, have observed changes in the measured GMR but it has been difficult to determine whether this is the true driving force behind the variation in GMR as the interface roughness has changed simultaneously with the crystallinity. This is a common problem and explains the often contradictory results reported. The position of the AF coupling peak with respect to the Cu spacer thickness has also been observed to move in response to changes in the sputtering pressure [6,20]. This in turn makes it intrinsically difficult to know at what thickness to grow the Cu spacer layer during deposition in order to maximise the AF coupling between the magnetic layers and hence maximise the GMR.

The effect of the substrate etch depends entirely on the energy of the ion beam. In the low energy case the ion beam begins to remove the native oxide layer from the surface of the substrate. At a higher energy, the ion beam begins to sputter into the silicon itself. This is thought to cause the nucleation and growth, upon deposition, of samples with less and less AF coupling caused by a change in the crystalline orientation of the multilayer. This dependence of coupling on texture is related to the Fermi surface effects already discussed in chapter 4.

## 5.4 Structure and Texture Dependence of GMR in Co/Cu

In the previous chapter the crucial role played by multilayer structure and texture with regard to coupling, scattering and GMR was discussed. It is worth taking a moment to relate this more specifically to the Co/Cu system in order to understand the need for a comprehensive characterisation of all aspects of these structures, concentrating predominantly on layer thickness, crystallographic texture, interface roughness and layer growth.

### 5.4.1 Thickness of the Cu Layer

In multilayers with a constant Co layer thickness the GMR ratio and saturation field, $H_s$, oscillate as the thickness of the Cu spacer layer is altered. Three maxima for the GMR ratio are found for Cu thickness of approximately 9, 19 and 30Å [18,21,27]. It can be seen from section 4.3.1 that the GMR can decrease dramatically to either side of this optimum spacer thickness. It is therefore essential to be able to measure accurately the thickness of this Cu layer across a series of samples in order to ensure that GMR changes are not simply due to a sample being grown with a thickness away from the selected AF coupling maxima.

### 5.4.2 Thickness of the Co Layer

The thickness of the magnetic Co layer is also very important in terms of studying the effect of bulk scattering on the magnetoresistance. In experiments performed by Shukh *et al.* [21] multilayers were grown with a constant Cu layer thickness corresponding to the second maxima of the magnetoresistance observed at $t_{Cu}$ = 19Å. This GMR ratio ($\Delta\rho/\rho_s$) was found to reach a maximum for a Co layer thickness of around 11Å, giving a GMR of 25% at room temperature. The ratio then decreased as the thickness of the Co layer increased. The GMR ratio is dependent upon on $\Delta\rho$, the change in resistance upon application of a saturation field, as well as the actual saturation resistance. The value of $\Delta\rho$ is solely due to the difference in the resistance of the multilayer system when the magnetic layers are in either parallel (saturation field) or antiparallel (zero field) alignment and is therefore a consequence only of the

differences in the degree of spin-dependent scattering due to orientation of the magnetisation.

At the point of magnetic saturation the magnetic moment of all single Co films within the multilayer are aligned parallel to one another due to the applied external field. The value of the resistance at this point, the saturation resistance, $R_s$, decreases as the Co layer thickness is increased. In this case it is not necessary to separate the spin-dependent part of the scattering and the application of a parallel resistor type model [18,21] allows a value for the total conductance, $1/R_s$, to be obtained. This leads to the relationship described by Youssef *et al.* [18], amongst others [21,22], in which

$$\frac{1}{R_s} = A + B(t_{Co})^2 \qquad [5.1]$$

where $A$ is a constant corresponding to any buffer or capping layers and $B$ is a constant depending on the geometric and electrical factors of the Co layers. This refers to parameters such as sample length, electron mean free path and the Co bulk resistivity. A plot of the inverse resistance versus the square of the Co thickness is shown in figure 5.1.

For Co layer thicknesses in the range 20Å < $t_{Co}$ < 70Å the inverse resistance is proportional to the square of the Co layer thickness, as shown in figure 5.1.

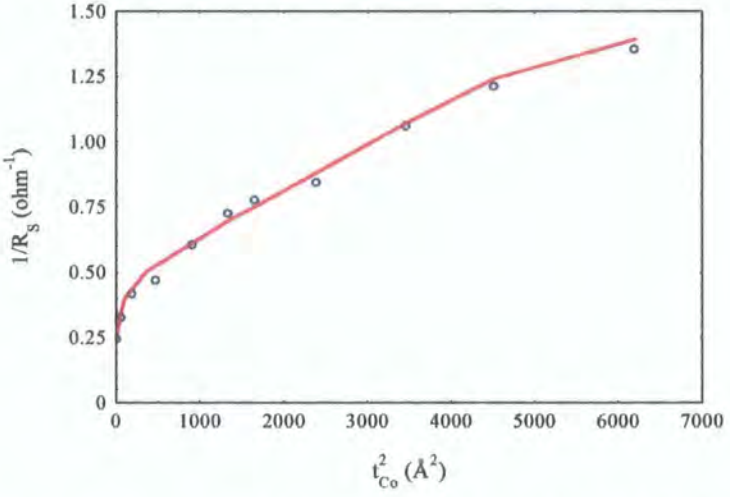


*Figure 5.1. Inverse resistance as a function of the square of the Co layer thickness, Shukh et al. [21]*

However for thin Co layers, in which the electron mean free path is of the same order or greater than the Co thickness, interface roughness causes surface scattering which adds a contribution to the resistivity and, on a mesoscopic scale, leads to a fluctuation in the layer thickness.

In summary, in the regime of thick Co layers the inverse resistance of the multilayer displays a linear dependence on the square of the Co thickness and arises because of the spin-dependent scattering in the multilayer. As the Co layers become thinner an increasing contribution to the resistivity arises from scattering processes at the interfaces. It is therefore important to be able to characterise the thickness of the Co layers within a multilayer when studying such systems in order to be able to estimate the effect that spin-dependent and interface scattering is having on the GMR. For the thickness of Co used in this particular study, nominally 10Å, it is possible that interface scattering due to roughness may contribute to the resistivity in addition to any bulk scattering effects and this is something that must be considered when studying the effect of the etching voltage on the magnitude of the measured GMR.

### 5.4.3 Interface Roughness

The effect of interface roughness within multilayer systems is important for two main reasons. Firstly, roughness at an interface causes spin-independent scattering of electrons that are moving through the multilayer. This in turn leads to an increase in the resistivity of the multilayer and hence a reduction in the GMR. There has been much debate as to the importance of interface scattering [18,27], and it is known to play an important role in some systems [22]. The variation of GMR with interface roughness has been studied extensively [18,23] and results suggest that in sputtered Co/Cu multilayers the MR decreases as the surface roughness, and associated spin-independent scattering, increases. However, in other studies in which Zr or Au has been included to deliberately damage and roughen the interfaces [24,25] results suggest that the GMR is proportional to the roughness and underpins all other observations. This illustrates the point that while the roughness is an important factor there are clearly other processes occurring that can influence the GMR.

Theoretical studies by Barnas *et al.* [26] suggest that the statistical nature of the interfaces, namely the fractal parameter, can also effect the GMR. The dependence of the GMR on the fractal nature of the interface could possibly explain why the GMR in samples grown by MBE, with a typical $h$ of 0.2, is generally lower than in those grown by sputtering, typical $h$ of 0.8, even though, in such studies the interfaces are, on average, smoother for MBE grown samples [28].

The second point to note is best illustrated in figure 5.2. In a system in which some of the layer thickness are relatively small, of the order of 5Å, and the interface roughness large, with little correlation between layers, one layer can penetrate into another to an appreciable degree.

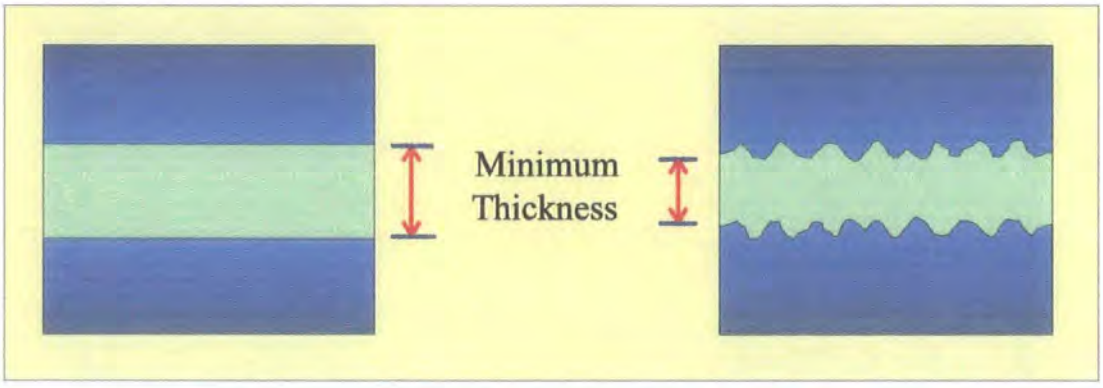


*Figure 5.2. Effective reduction of layer thickness due to interface roughness.*

This effectively reduces the layer thickness intended by the grower and can severely reduce the GMR by shifting the spacer thickness away from that of the AF coupling maximum.

### 5.4.4 Texture and Growth

The dependence of the GMR on the crystallographic texture and Fermi surface effects that give rise to spin-dependent scattering in magnetic multilayers is crucial. The need to retain constant layer thicknesses within magnetic multilayer systems leads inevitably to the need to be able to grow systems in which the individual layers are well defined. In figure 5.3 a uniform growth model is contrasted with a non uniform model, illustrating the way in which layer thickness and hence coupling can be lost.

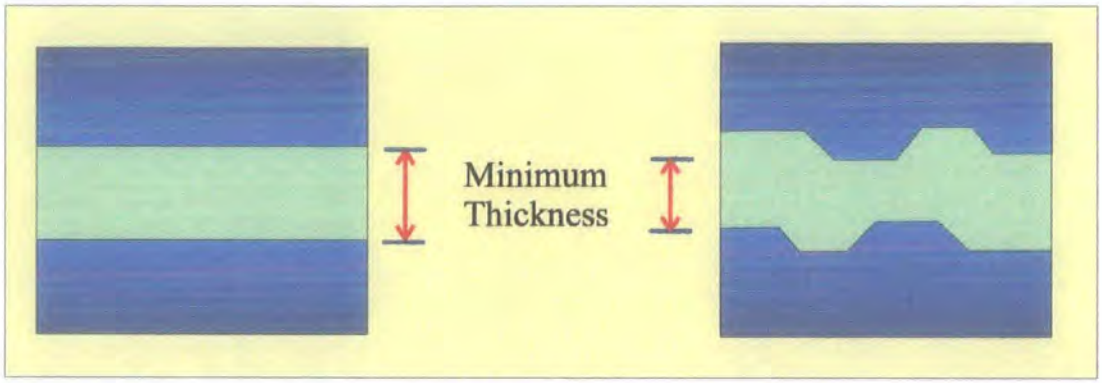


*Figure 5.3. Diagram to illustrate the effect of non ideal layer growth on the film thickness.*

In the sputter deposition process the immiscibility of the Co and Cu species generally leads to the formation of sharp interfaces between layers and promotes well defined layer growth within the system [29].

The crystallographic texture of a multilayer is known to have an effect on the size of the GMR. Theoretical studies [30] have suggested that the magnitude of the Fermi surface effects that give rise to the oscillations in GMR, should be greater in systems with a strong (100) or (110) orientation. However, as mentioned in chapter 4, studies have both supported [31] and contradicted [28] this view. It is for this reason that in this study a characterisation of the texture of the multilayers is taken as being of equal fundamental importance as the characterisation of layer thickness and interface roughness if any firm conclusions are to be reached as to the driving force behind the GMR.

## 5.5 GMR as a Function of the Etching Voltage.

The giant magnetoresistance (GMR) of the samples was measured, by D.E. Joyce at Salford, at room temperature using a standard d.c 4 point probe method with the current and magnetic field orthogonal and in the plane of the film. The magnitude of the GMR effect is defined in the standard way such that:

$$GMR(H) = 100 \times \left( \frac{\Delta\rho(H)}{\rho_S} \right) \qquad [5.2]$$

where $\rho_s$ is the resistivity measured in a saturation field and $\Delta\rho$ is the absolute difference between the saturation and zero field resistivity. The maximum GMR, the value quoted throughout this chapter, corresponds to the difference between $H$=0 and $H$=$H_S$. Magnetic hysteresis loops for the type B multilayers were measured, again at room temperature, using a laboratory AGFM. Although care was taken to minimise the effect of the gradient field on the magnetic state of the sample the measurements near zero field are inherently unreliable.

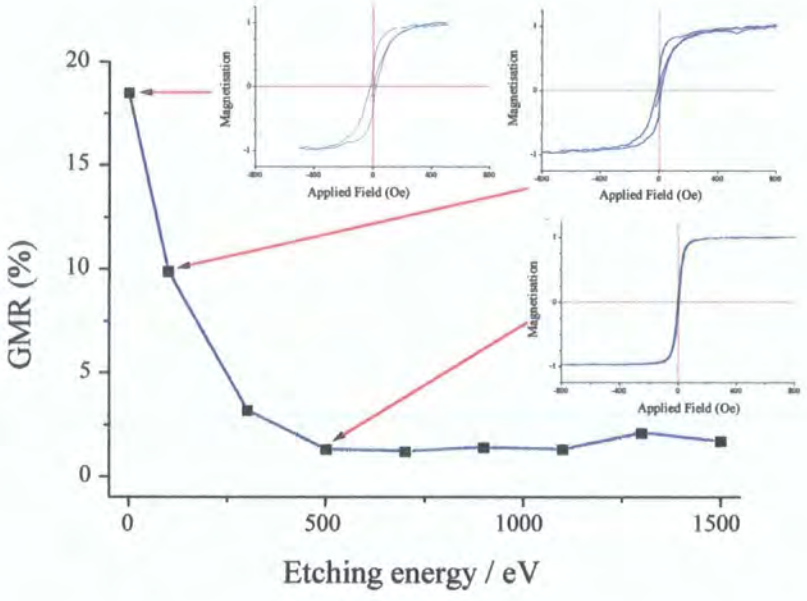


*Figure 5.4. Variation in magnetic and magnetotransport behaviour caused by substrate etching.*

The GMR values and associated hysteresis loops for these samples are shown in figure 5.4. There is a dramatic drop in the GMR as the etching voltage is increased. This trend was repeated in several other sets of identically prepared, type B, samples and in a series of the thinner, type A, samples. This trend was also observed in work by Pollard *et al.* [6]. The shape of the hysteresis loops indicate the degree of antiferromagnetic coupling within a sample and this also changes markedly across the series. As the

etching voltage is increased the loops become noticeably more upright and ferromagnetic in nature as the contribution from the antiferromagnetically (AF) coupled regions of the sample is lost. The remanance changes little across the series as the AF component reduces due to the change being masked by the regions of ferromagnetic coupling. The coercivity and the saturation field both clearly decrease with increasing etching energy. This indicates an easier switching of the magnetisation state as the antiferromagnetic component is reduced. It has been suggested [32] that the fraction of coupling that is ferromagnetic in nature may increase with the order of the antiferromagnetic coupling maximum and may completely mask the higher order AF maximum. This is certainly consistent with the magnetic results discussed here. The multilayer prepared on the unetched substrate gives a credible room temperature GMR of approximately 18%. The GMR eventually saturates on average at around 2% as the etching energy is increased.

## 5.6 Polarised Neutron Reflectivity (PNR)

The change in the magnetic coupling observed in the magnetic hysteresis loops was studied further, by D.E. Joyce, using polarised neutron reflectivity. The measurements were carried out on the ISIS pulsed neutron source at the Rutherford Appeleton laboratory. A more detailed description of the instrumentation, and a discussion of the theory can be found elsewhere [33-35]. Discussion relating to the experimental aspects of these measurements can be found in the published work [36]. Evidence of antiferromagnetic coupling between the magnetic layers within this system was expected, due to the Cu layer being grown at the second AF coupling peak as discussed earlier. Therefore, the neutron reflectivity curve should exhibit a definite dependence on the applied field as the magnetic profile of the multilayer changes upon application of a saturation field to the sample.

The neutron reflectivity scan for the unetched sample exhibits a 'half order' peak corresponding to a magnetic super-structure with a period twice that of the chemical structure and is indicative of a significant degree of antiferromagnetic coupling in the samples. The origin of this peak is confirmed when, upon application of a saturation field to change the magnetic structure from antiferromagnetic to ferromagnetic coupling,

the peak at the $Q_{mag}$ position disappears as the magnetic and chemical unit cell are now of the same dimension. The intensity of the multilayer Bragg peak is seen to increase as a consequence of the increase in magnetic order.

When a similar study of one of the heavily etched samples was performed no magnetic half order peak was observed and there was no change in the reflectivity profile upon application of a saturation field, except for the slight increase in the Bragg peak intensity. This in itself can be attributed to the improvement in magnetic order between the remanent and saturated states. These results corroborate the conclusions drawn from the magnetic hysteresis loops, namely the loss of the antiferromagnetic coupling component as the etching energy is increased.

## 5.7 Structural Characterisation

The dramatic reduction in the GMR, shown in figure 5.4, could simply be explained by a reduction in coupling due to a variation in the thickness of the Cu spacer layer across the series of samples. Such variations in the GMR could also be explained by a change in the amount of spin-independent scatter generated by differing amounts of interface roughness.

For this reason extensive grazing incidence x-ray reflectivity measurements and simulations have been performed in order to characterise the structure of all of the multilayer systems. X-ray reflectivity provides the ideal non destructive tool with which to characterise such systems as the technique is sensitive to the many buried interfaces within such a system. Only when the magnetotransport data already discussed is studied in conjunction with accurate structural information is it possible to reach conclusions regarding the processes driving the GMR effect.

### 5.7.1 X-ray Reflectivity Measurements.

The three specific types of x-ray reflectivity scans were performed, namely the specular, longitudinal diffuse and transverse diffuse. These are discussed extensively in chapter 2 and the reader is referred to this section for more details. All of the data in this section were taken, for type A samples, on Station 2.3, SRS Daresbury.

A specular and off-specular scan taken for the 100 volt etch sample are shown in figure 5.5. There are several characteristic features to note. Firstly, in the specular data there is a Bragg peak at a sample angle of approximately 7000". The high frequency Kiessig fringes, present in the off-specular scan, indicate that a high proportion of the interface roughness is correlated throughout the sample. These off-specular features were observed in measurements made on all 4 samples.

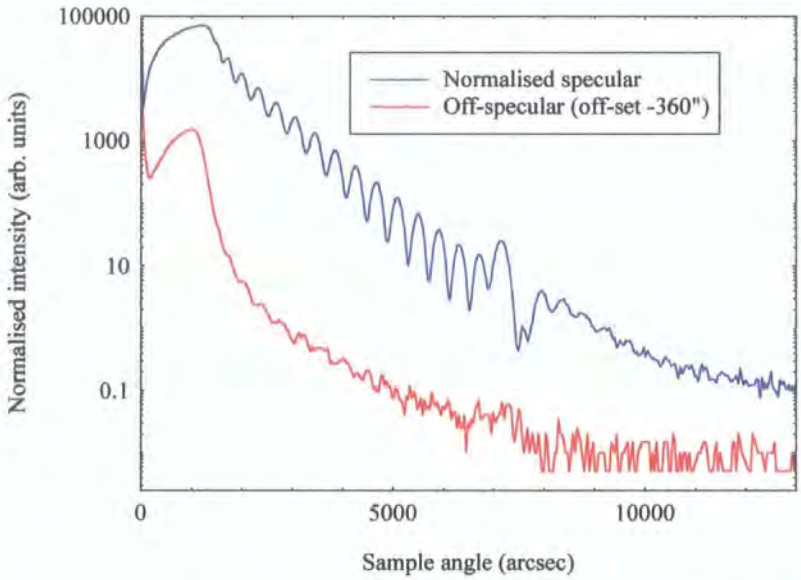


*Figure 5.5. Specular and off-specular scan for 100V etch sample, Co edge λ=1.608Å.*

The tunability of synchrotron radiation allows the measurements to be performed at the Co and Cu absorption edges. This in turn allows the phenomenon of anomalous dispersion, discussed in chapter 2, to be exploited in order to enhance the scattering contrast between the buried Co and Cu layers [13]. The effect of the anomalous dispersion correction to the scattering factor described earlier can clearly be seen in the specular and transverse diffuse measurements taken for the Co/Cu system.

Figure 5.6 shows a specular scan taken for the 0V etch sample at and away from the Cu edge. A specular scan taken for the 500V etch sample at and away from the Cu edge is shown in figure 5.7. By taking scans at and away from either the Co or Cu absorption edge it is possible to distinguish between scatter originating from the multilayer as opposed to the capping layer.

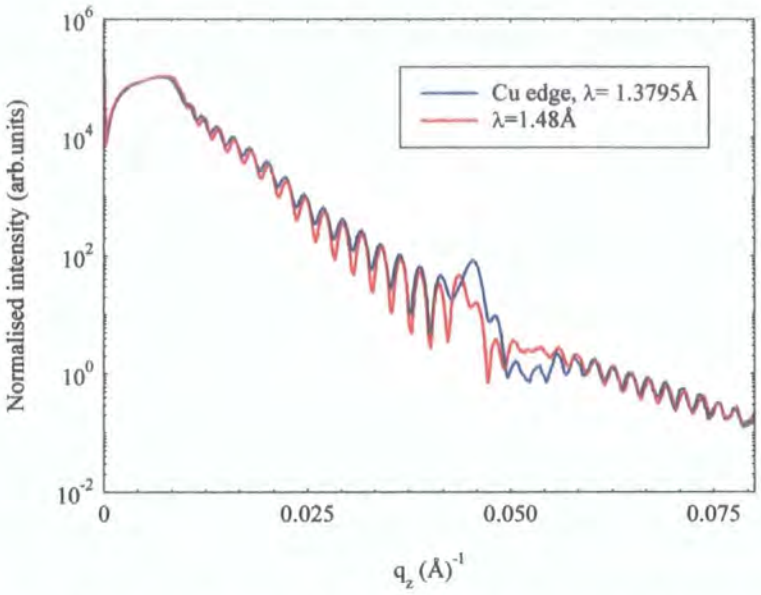


*Figure 5.6. Specular scan for the unetched sample taken at and away from the Cu absorption edge.*

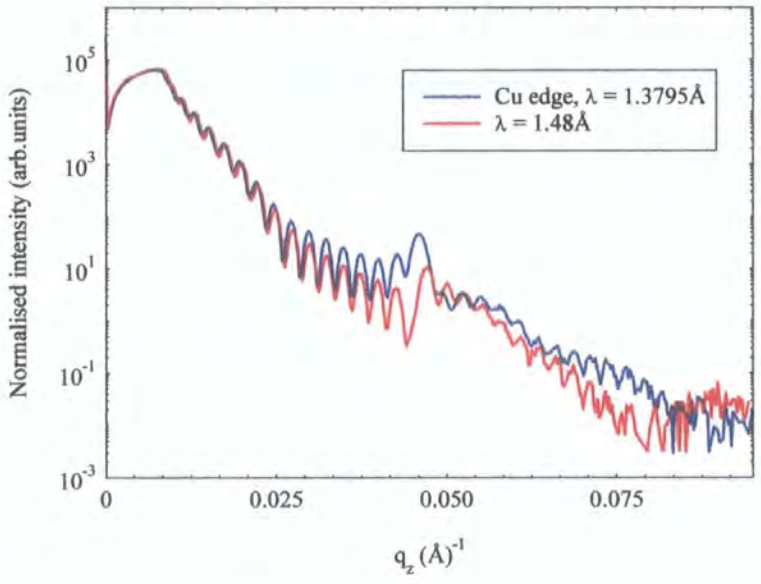


*Figure 5.7. Specular scan for the 500V etch sample taken at and away from the Cu absorption edge.*

By tuning to Cu absorption edge there is noticeable increase in the specular Bragg peak intensity, figures 5.6 and 5.7. This increase occurs predominantly at the Bragg condition due to an enhancement in the definition of the Co/Cu interfaces as a consequence of the anomalous dispersion correction increasing the scattering factor difference between the layers. Transverse diffuse scans taken both at and away from the Co and Cu absorption edges for the 100 volt and 500 volt etch samples are shown in figures 5.8 and 5.9. These scans taken through the Bragg peak position show almost a two fold increase in diffuse scatter by tuning to the Co and Cu absorption edges.

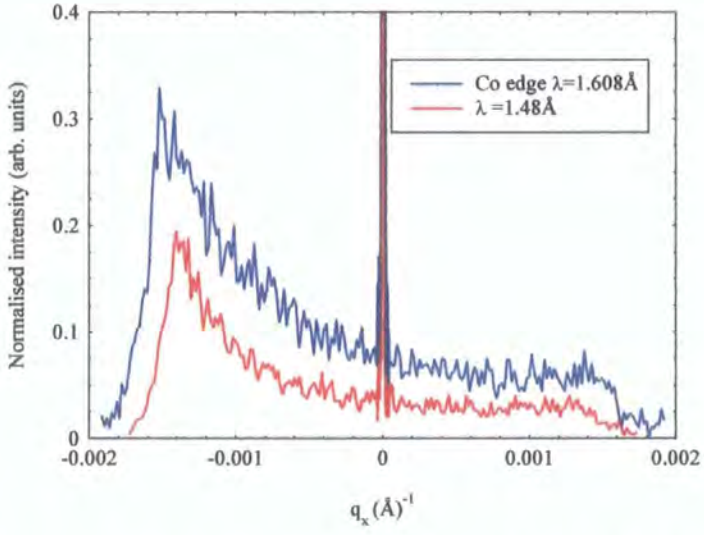


*Figure 5.8. Transverse diffuse scans taken through the Bragg peak position, at and away from the Co edge for the 100V etch sample.*

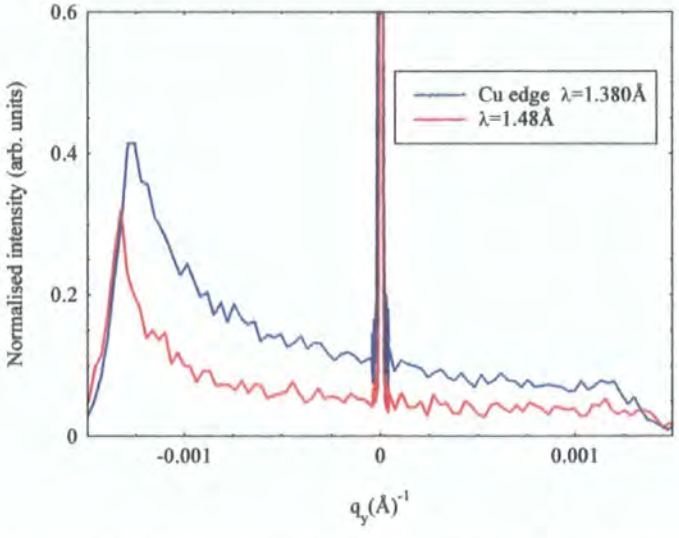


*Figure 5.9. Transverse diffuse scans taken through the Bragg peak position, at and away from the Cu edge for the 500V etch sample.*

However, in transverse diffuse scans taken away from this Bragg condition, figures 5.10 and 5.11, there is virtually no observed difference in the diffuse scattering at and away from the edge.

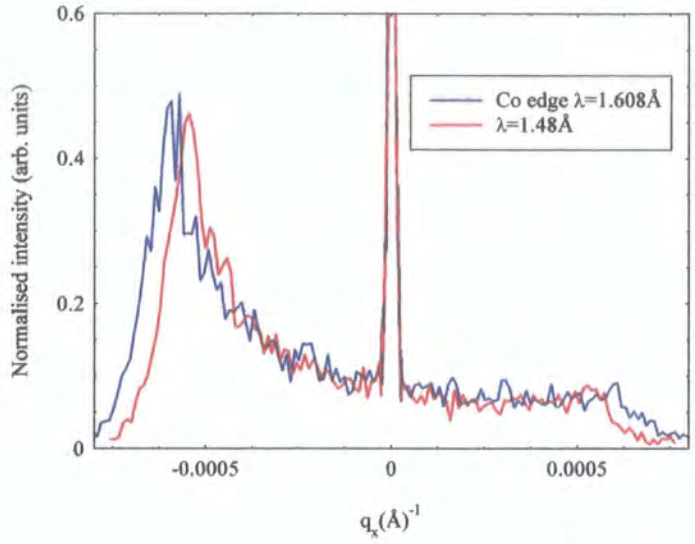


*Figure 5.10. Transverse diffuse scans taken away from the Bragg peak position, at and away from the Co edge for the 100V etch sample.*

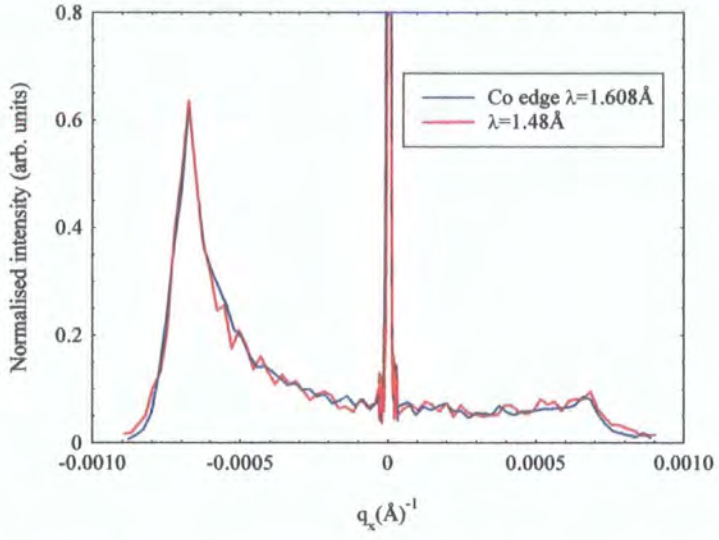


*Figure 5.11. Transverse diffuse scans taken away from the Bragg peak position, at and away from the Co edge for the 500V etch sample.*

Diffuse scatter confined to the Bragg angle originates from coherent scatter from the Co and Cu bilayer interfaces generated by a high degree of correlated roughness at these interfaces [37]. The observation that the diffuse scatter is enhanced by anomalous dispersion at the Bragg condition but not away from it therefore gives a further indication that the majority of roughness within the multilayer is conformal in nature with spatial frequencies replicated from layer to layer.

Figures 5.12 a) to d) show a series of best fit simulations to the specular data for samples of different etching energy. The simulations are performed using the GIXA code developed by M.Wormington [38,39] and is discussed in chapter 2.

The simulations allow bilayer and total stack thickness to be determined. The fit at the critical angle is dependent upon the near surface electron density and the rate of reduction in intensity with angle is controlled predominantly by the interface roughness.

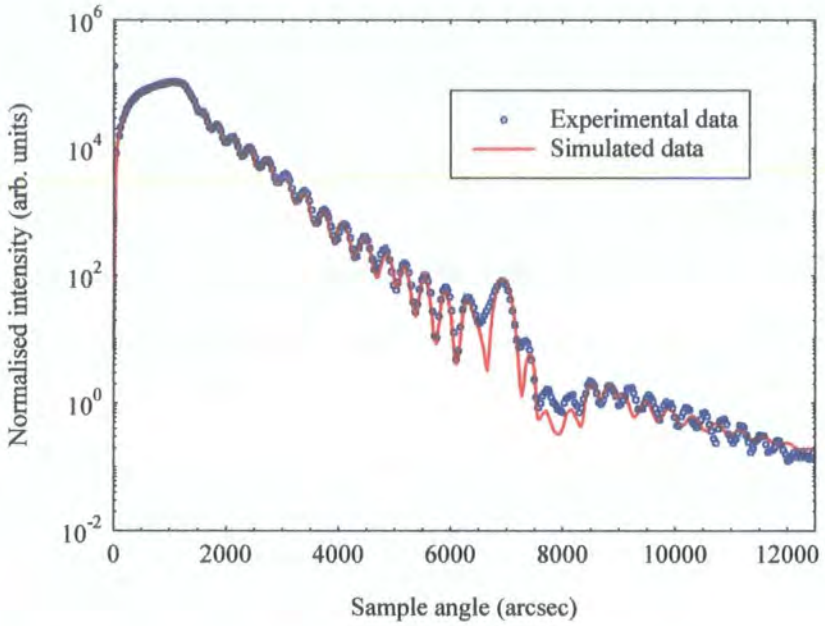


*Figure 5.12 a). Specular data and best fit simulation for the unetched sample, λ=1.38Å.*

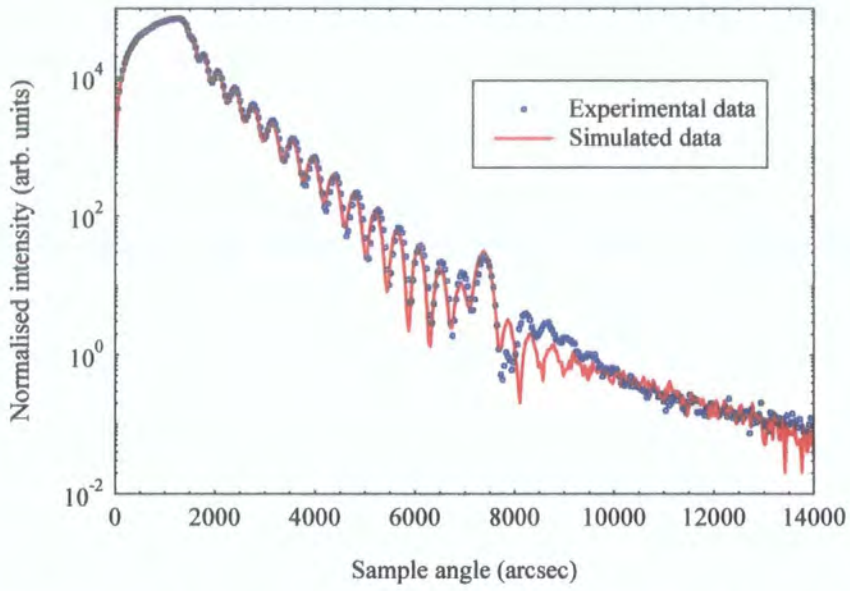


*Figure 5.12 b). Specular data and best fit simulation for 100V etch sample, λ= 1.48Å.*

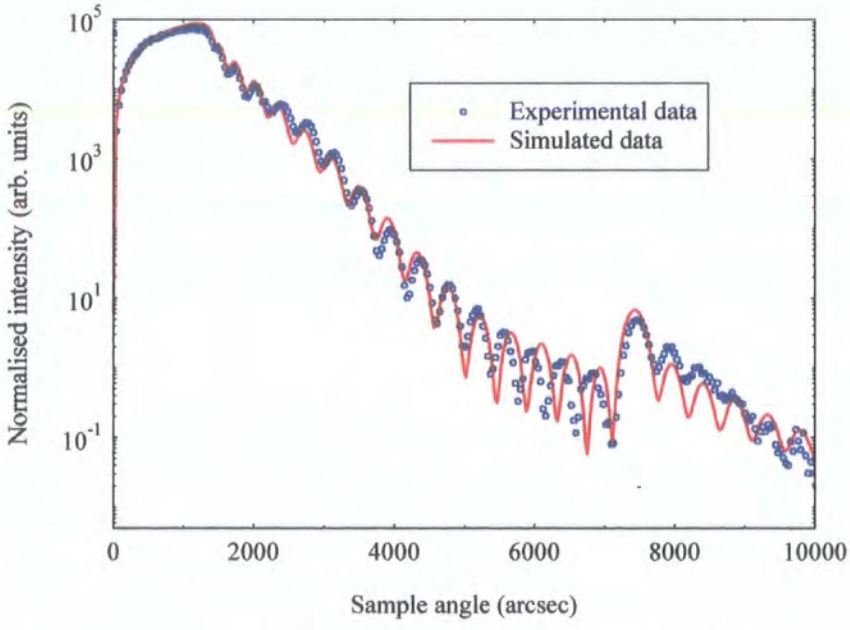


*Figure 5.12 c). Specular data and best fit simulation for 300V etch sample, λ= 1.48Å*

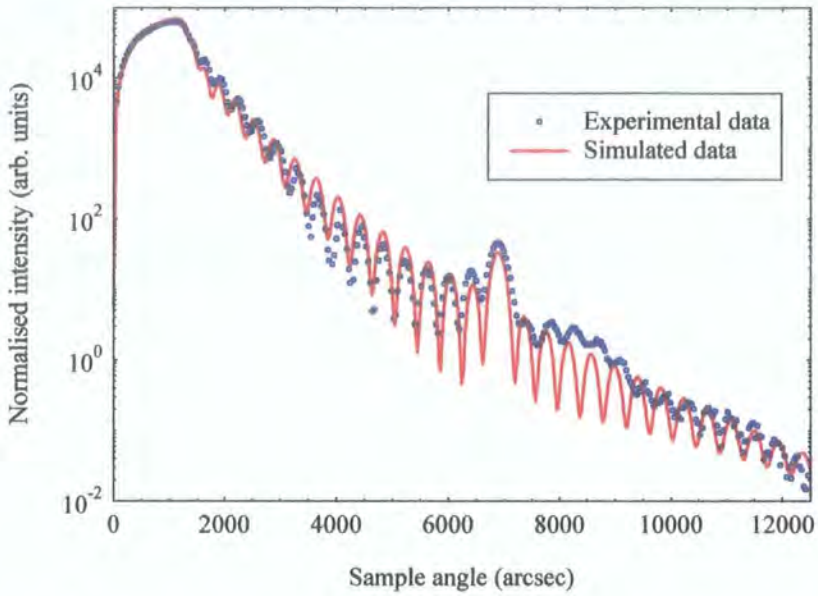


*Figure 5.12 d).Specular data and best fit simulation for 500V etch sample, λ=1.38Å.*

There was a common problem in simulating accurately the region just beyond the Bragg peak in most cases. In common with a study by Gu *et al.* [29], in which the same problem was encountered, it was found that this region of the simulation is primarily sensitive to the structure of the bottom layer. The modelling code assumes an error function profile for the electron density variation across an interface and the deviation from an ideal fit in this region may be due to the code not modelling the effect of the sputter damage to the silicon and native oxide layer perfectly. Due to the poor contrast between silicon and silicon oxide, the x-rays were found to be insensitive to the thin native oxide layer. However, it was possible to observe this oxide layer through TEM measurements discussed later in this chapter. All of the simulations are of a sufficiently high accuracy to determine confidently layer thickness and average effective roughness as well as confirming that the near surface layers had deposited at standard bulk density.

The transverse diffuse data was then simulated, using the same code, with the parameters determined from the specular simulations being used to help reduce the large number of free parameters in the diffuse fitting. Transverse diffuse measurements are sensitive to the exact nature of the interface disorder, be it conformal or uncorrelated roughness or an electron density gradient normal to the interface.

Such measurements also allow the characterisation of the interface morphology by determining the lateral correlation length, $\xi$, and the fractal Hurst parameter, $h$. Transverse diffuse scans are typically taken at and away from the Bragg condition so as to be able to determine the degree of correlated and uncorrelated roughness more accurately.

A series of transverse diffuse scans taken at multiple scattering vectors at and away from the Bragg condition, and at different wavelengths, for the series of samples are shown in figure 5.13 a) to p) along with their respective best fit simulations.

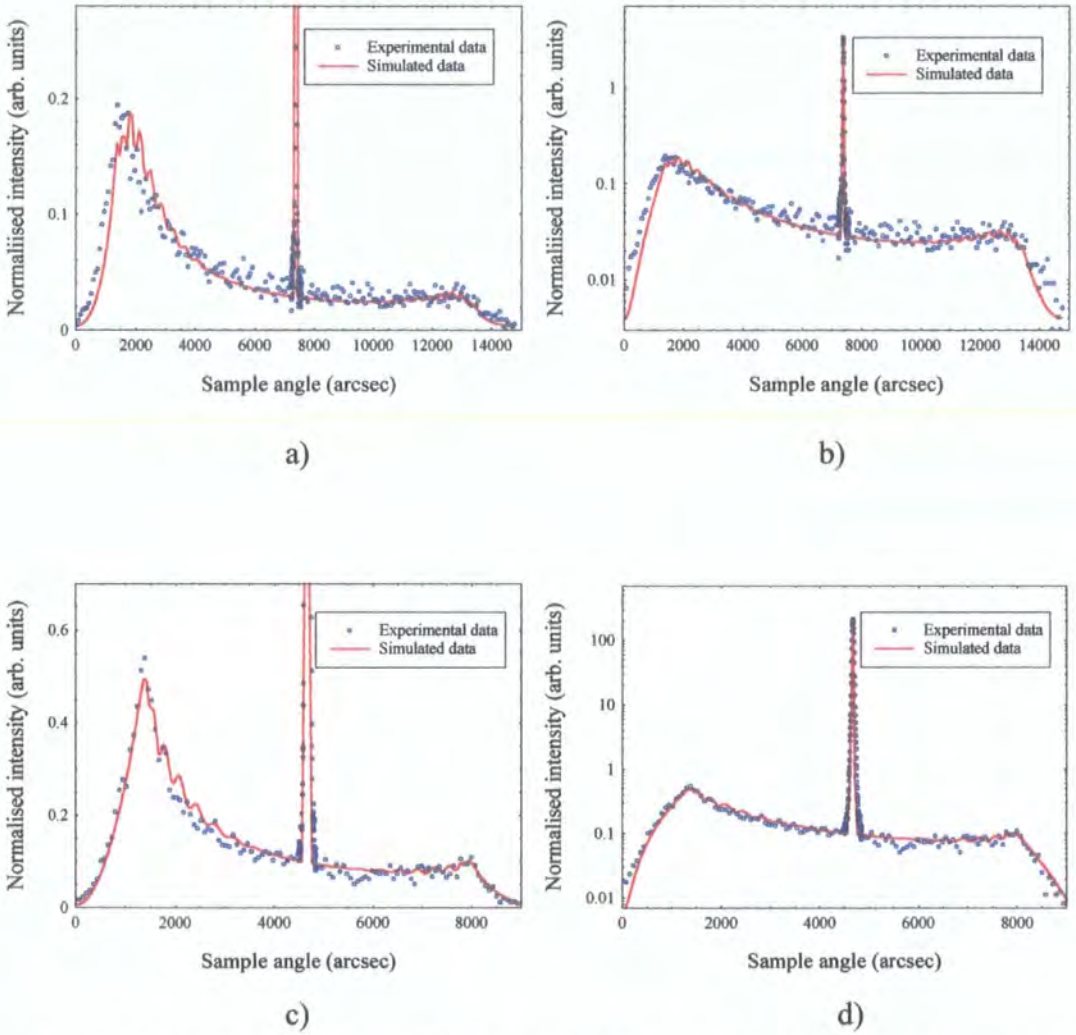


*Figure 5.13 a) 100V etch sample, Bragg peak, λ= 1.48Å. b) log scale c) 100V etch sample, Kiessig maximum, λ= 1.48Å d) log scale.*

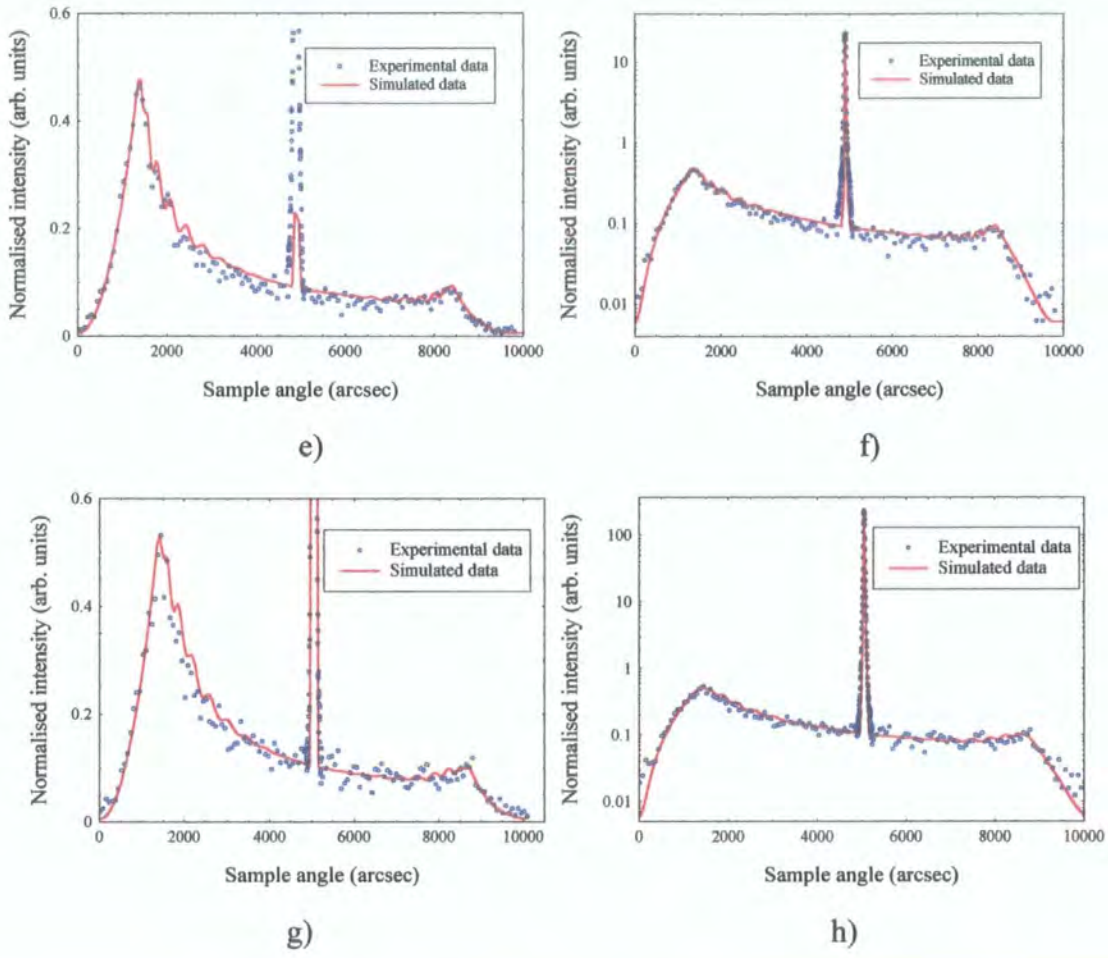


*Figure 5.13 e) 100V etch sample, Kiessig minimum, λ= 1.48Å. f) log scale g) 100V etch sample, Kiessig maximum, λ= 1.608Å h) log scale.*

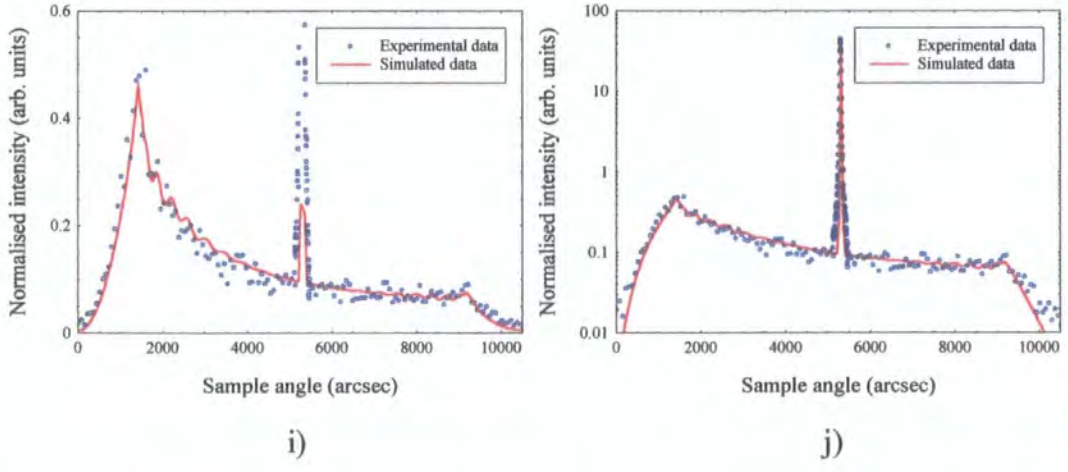

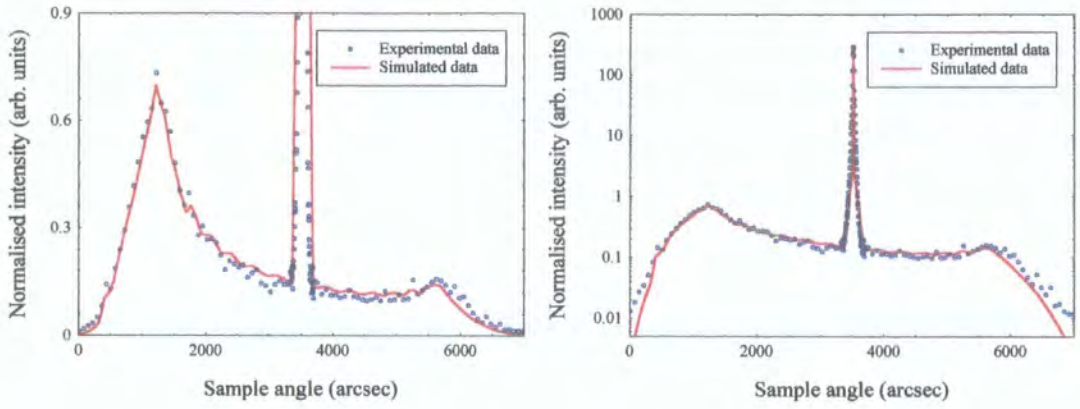


*Figure 5.13 i) 100V etch sample, Kiessig minimum, λ= 1.608Å. j) log scale k) 500V etch sample, Bragg peak, λ= 1.308Å l) log scale.*

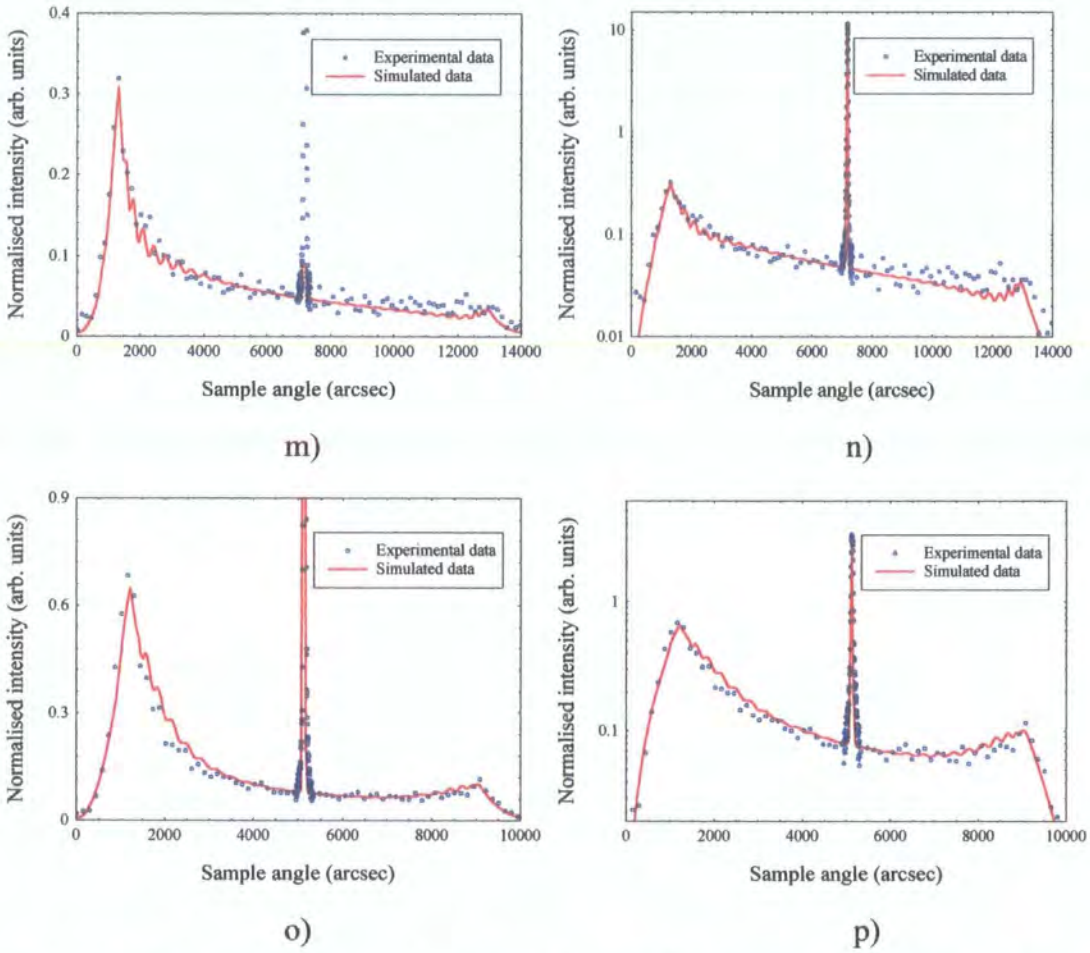


*Figure 5.13 m) 500V etch sample, Bragg, λ= 1.48Å. n) log scale o) 500V etch sample, Kiessig minimum, λ= 1.308Å p) log scale.*

From these simulations it is possible to obtain a full structural model of each of the multilayers. A summary of the structural parameters determined from the x-ray scattering simulations is given in table 5.1.

| Etch (V) | Cu thickness (Å) | Co thickness (Å) | Average Roughness σ (Å) | Correlation length ξ (Å) | Fractal parameter, *h* | uncorrelated /conformal roughness |
|---|---|---|---|---|---|---|
| 0 | 10.5 ± 0.5 | 10.1 ± 0.5 | 5.4 ± 0.5 | 85 ± 5 | 0.9 ± 0.1 | 0.29 ± 0.02 |
| 100 | 10.7 ± 0.5 | 10.1 ± 0.5 | 5.2 ± 0.5 | 85 ± 5 | 0.9 ± 0.1 | 0.29 ± 0.02 |
| 300 | 10.2 ± 0.5 | 10.3 ± 0.5 | 5.4 ± 0.5 | 100 ± 5 | 0.9 ± 0.1 | 0.29 ± 0.02 |
| 500 | 10.5 ± 0.5 | 10.2 ± 0.5 | 5.1 ± 0.5 | 118 ± 5 | 1.0 ± 0.1 | 0.29 ± 0.02 |

*Table 5.1 Multilayer structure parameters determined from x-ray scattering simulation.*

There are several important features to note. Firstly the thickness of the copper spacer layer remains constant, within the accuracy of the simulation, across the series of samples and does indeed correspond to the intended growth thickness selected to match that of the first AF coupling maximum discussed earlier. The ability of modern sputtering systems to grow Cu layers accurately and with a high degree of reproducibility is indicated by these results. More importantly, this means that the loss of antiferromagnetic coupling as the etching energy is increased cannot be caused by the growth thickness of the copper layer varying across the series of samples. The thickness of the cobalt layer is also found to remain constant which in turn means that with regard to the discussion in section 5.4.2 the degree of spin-dependent scattering and relative contribution to the resistivity arising from interface roughness scattering is the same in all samples

Secondly the interface roughness is indeed highly correlated in nature between adjacent layers within the stack, as indicated qualitatively in the off-specular data, with no evidence of any compositional grading. This conformality is retained throughout the entire stack from the substrate upwards. The average roughness across the series of samples is determined to be 5.3 ± 0.5Å and varies from this by no more than 0.2Å for any one sample in the series. In all cases the ratio of uncorrelated to conformal

roughness is found to be 0.29 ± 0.02. The observation that the interface roughness is constant in both magnitude and nature across the sample series is of great importance. Provided the roughness is largely conformal through the stack the separation between adjacent magnetic and non magnetic layers is preserved, thus maintaining one of the most important prerequisites for GMR. The spin-independent scattering at the interfaces, which can contribute to the resistivity of the multilayer and therefore effect the GMR, must be of the same magnitude for each of the multilayers studied as a consequence of the roughness being the same for all samples. Furthermore, the interpenetration of one layer into another as a consequence of this roughness, as discussed in section 5.4.3, is also of the same magnitude so any effective reduction in layer thickness due to this is the same for all samples.

The interface morphology of the sample can be characterised further in terms of the lateral correlation length and the fractal Hirst parameter. Calculations performed by Gu *et al.* [29] based on the 2% lattice mismatch of Co and Cu and a lattice constant of around 3.5Å suggest that for systems in which there is an appreciable degree of epitaxial growth the lateral correlation length should be of the order of 150Å. In this series of films the lateral correlation length is found to be slightly shorter than this. This difference is most likely due to the surface mobility of the Co and Cu species on deposition being slightly lower than normal due to either a lower than optimal deposition temperature or the restricted mobility of deposited material due to the etching of the substrate. This could lead to a lateral correlation length which is shorter than that calculated for the initially deposited layers which would then be replicated to the surface due to the high degree of conformality in the system. In a similar way to the interface roughness, the lateral correlation length, $\xi$ , and fractal parameter, $h$, also remain constant across the series of samples.

### 5.7.2 Transmission Electron Microscopy and Diffraction.

Cross section transmission electron micrographs, performed by D.E. Joyce, provide a more intuitive, if localised, view of the interface structures and their propagation within the multilayer. Figure 5.14 a) and b) show a pair of defocussed micrographs taken for an unetched and heavily etched sample with a 10Å Cu spacer.

The microscope is defocused in order to enhance the phase contrast between the Co and Cu layers, thereby revealing the layer structure.

In each case the Si substrate is at the bottom of the micrograph. The native $SiO_2$ layer between the unetched substrate and multilayer is clearly visible in figure 5.14 a). Even though the substrate has been etched heavily in figure 5.14 b) there would still appear to be an amorphous layer between the substrate and the multilayer indicating that not all of the native oxide layer has been removed by the etch.

The similarity between the images is very apparent and in very good agreement with the x-ray modelling results, although direct comparison is difficult due to the increased strain contrast in the heavily etched film. The images show in figure 5.14 a) and figure 5.14 b) show the lateral correlation length of the surface roughness and quantitative measurements show this to be the order of that determined from the x-ray simulations. It is also possible to see from these TEM measurements that the interfaces between the Co and Cu are sharp suggesting that it is more of a long length scale rippling, consistent with the observed high $h$ values, that contributes to the average roughness measured in the x-ray reflectivity, illustrating the importance of growth conformality in the stack.

TEM and transmission electron diffraction (TED) measurements performed, for the type A samples, with a Cu thickness of 10Å are shown in figure 5.15. It is not possible to see any layer contrast in either of these images due to the similar scattering factors of Co and Cu. The changes in bulk texture with substrate etching are very clear. Figure 5.15 a) shows an unetched sample in which the electron diffraction pattern contains the silicon spots, on the [110] zone axis, from the substrate and the first diffraction orders from a random polycrystalline f.c.c microstructure in the multilayer. The small diffraction aperture used means that the rings are not completely continuous as only a restricted number of grains are being probed by the electron beam.

The native silicon oxide layer is also visible in the micrograph as are the resolved Si {111} lattice fringes. The etched sample in figure 5.15 b) is very different in nature. In this case the diffraction by the film is limited to short {111} arcs along the [001] silicon direction, in other words diffraction from {111} Co/Cu planes parallel to

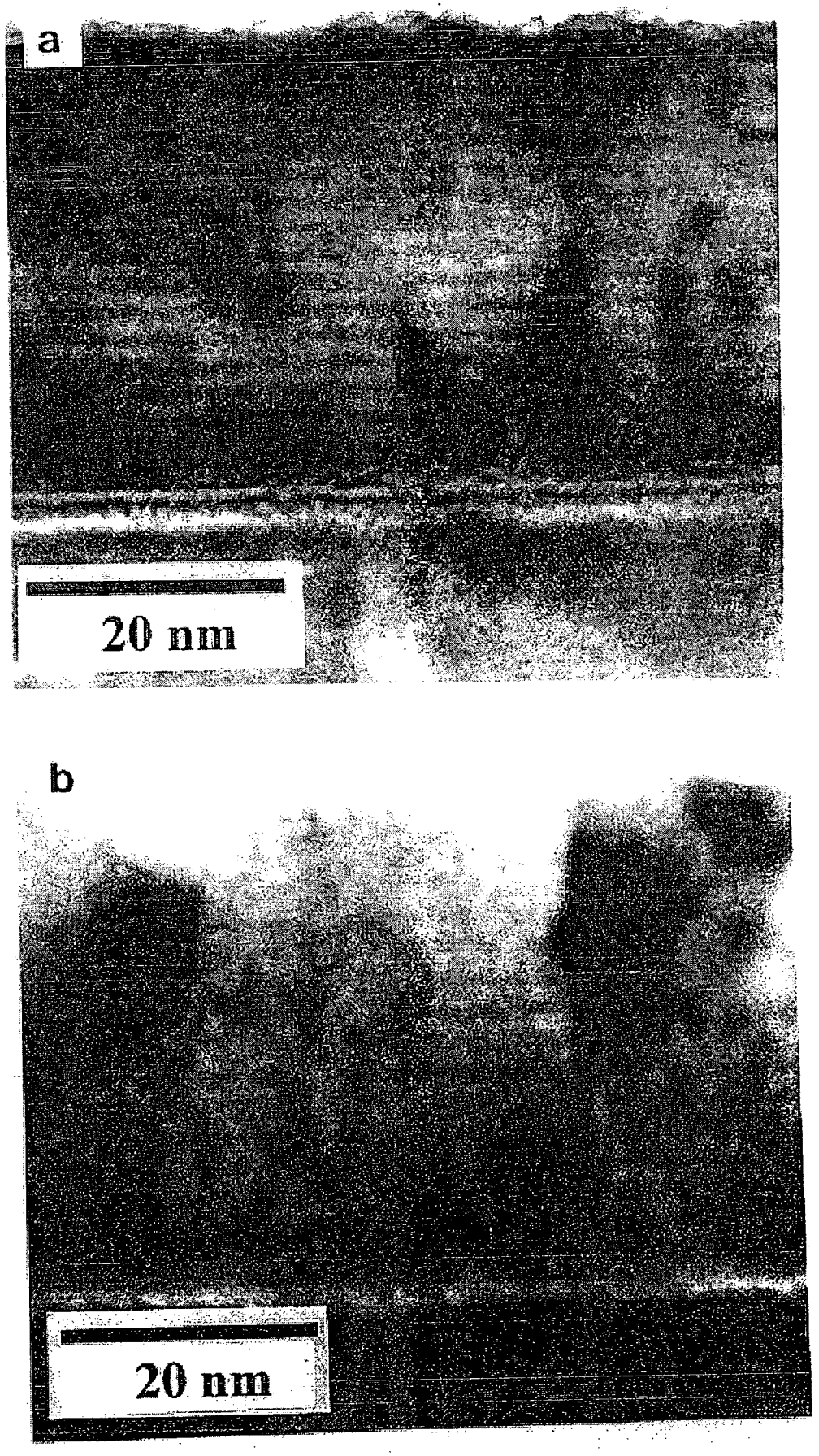


*Figure 5.14 Defocussed TEM images for an a) unetched and b) heavily etched sample [36].*

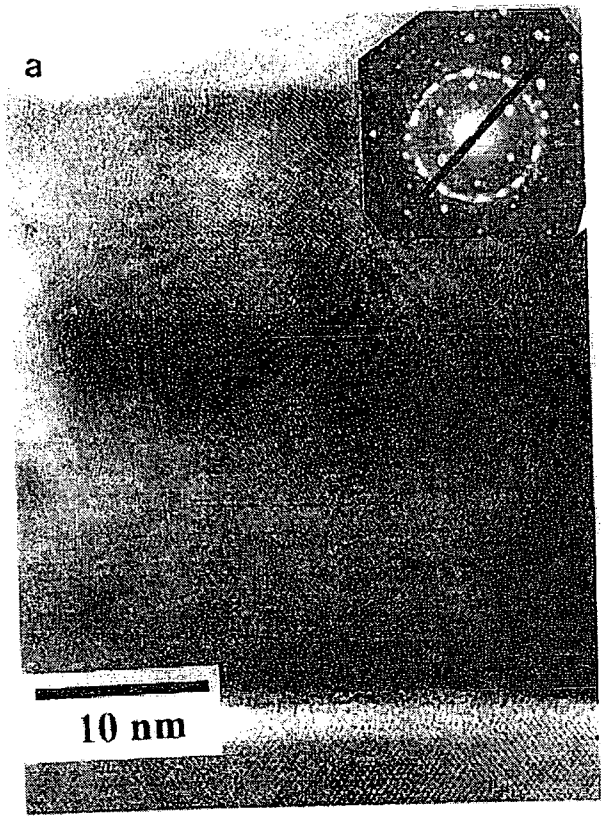


*Figure 5.15 a). Cross section TEM micrograph of an unetched sample with TED pattern (inset) [36].*

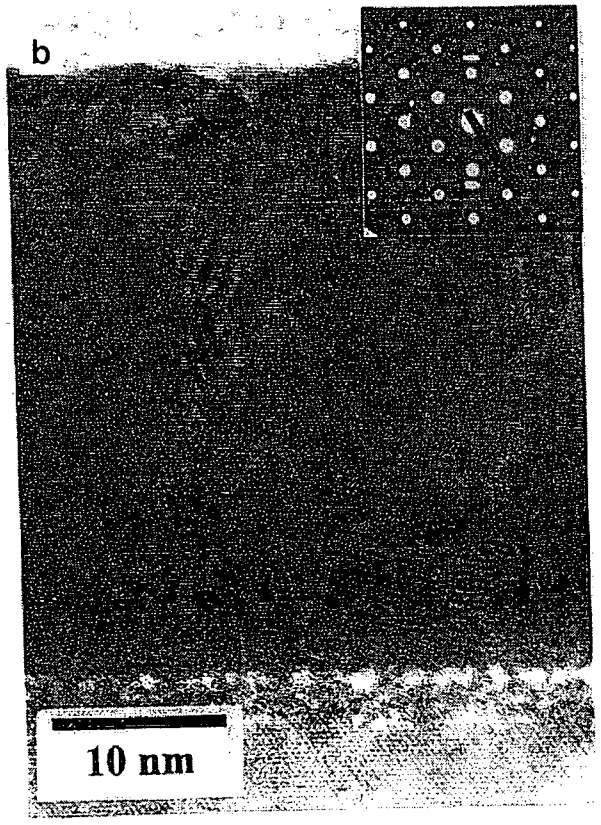


*Figure 5.15 b) Cross section TEM micrograph of a heavily etched sample with TED pattern (inset) [36].*

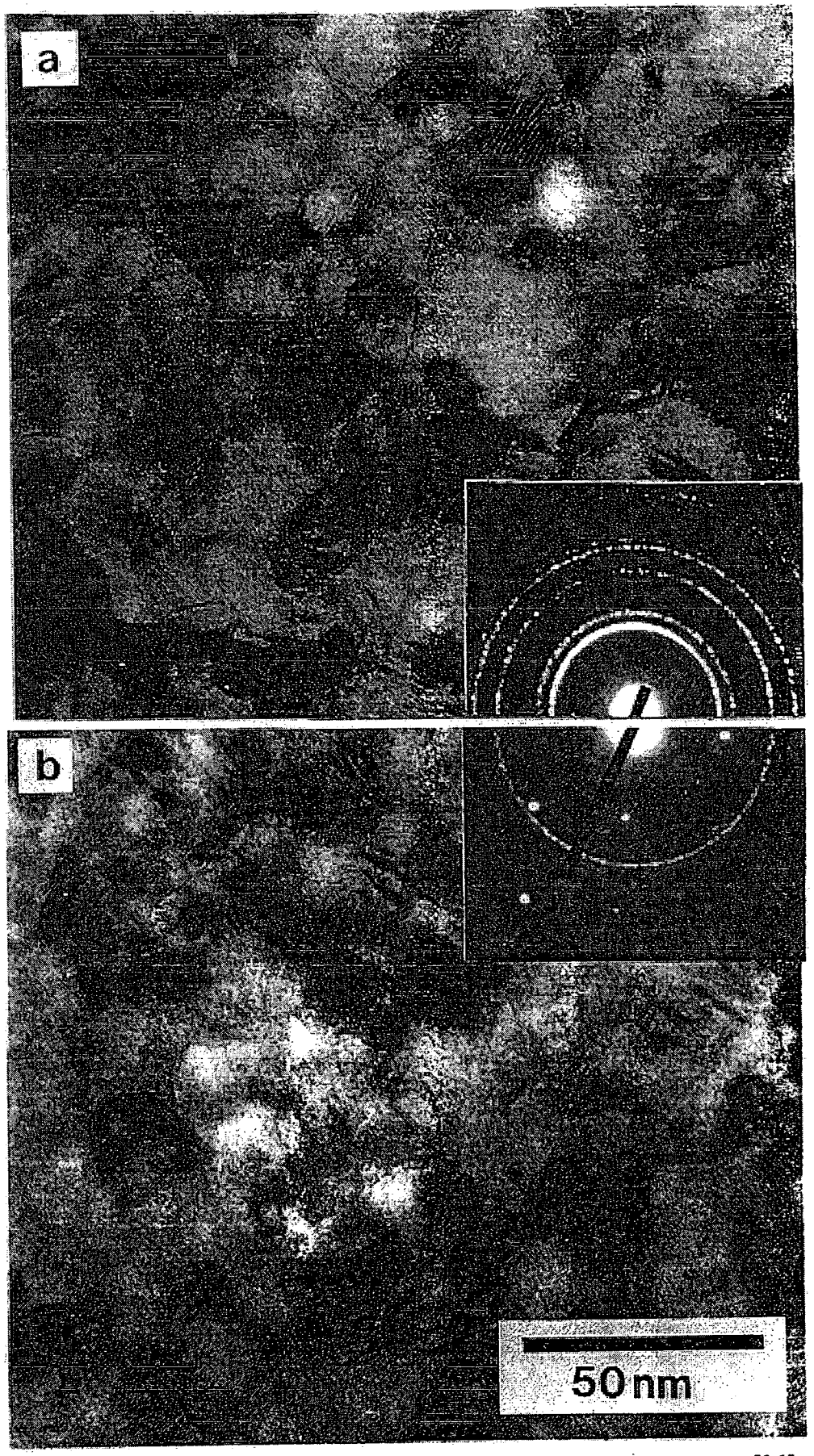


*Figure 5.16 In-plane TEM micrographs and associated TED patterns [36].*

the film plane of the multilayer. From examining the lattice fringe contrast from the multilayer in the micrograph it is found that although the texture does not correspond exclusively to {111} grains oriented parallel to the substrate and the interfaces of the multilayer a significant fraction of the sample is growing with a strong <111> axis. In plane micrographs, performed with most of the substrate removed, are shown in figure 5.16 a) and b).

These micrographs show the grain size in the multilayer to be of the order of 200 -300Å, comparable to the lateral correlation length determined from the diffuse scatter, and roughly the same in both the etched and unetched samples. They also show a transition from a random polycrystalline structure, figure 5.16 a), to a mosaic structure with a preferred growth direction along the <111> direction, figure 5.16 b). The intensities of the rings in the diffraction pattern inset into figure 5.16 a) are typical of a randomly oriented f.c.c microstructure whilst the noticeable increase in intensity of the {220} ring and the much reduced intensity of the other reflections in figure 5.16 b) is consistent with a very strong <111> texture.

The structural observations from the x-ray scattering and TEM measurements are crucial to understanding the mechanism behind the loss of the GMR with increasing etching voltage. The two most obvious mechanisms for the loss of GMR are a change in the interfacial scattering contribution, due to roughness changes, or a change in the coupling due to spacer thickness changes. Both of these mechanisms can be ruled out, through the x-ray structural characterisation supported by TEM observations, as both the interface roughness and spacer thickness are seen to remain constant, within error, across the series. The most likely driving force behind the GMR changes is, therefore, a change in the volume contribution to the GMR, dependent on the crystal structure.

### 5.7.3 High Angle X-ray Diffraction (HXRD)

The change in texture indicated in the TED measurements was confirmed by High Angle X-ray Diffraction measurements, performed by D.E. Joyce. Figure 5.17 shows high angle diffraction data for both the unetched and a heavily etched, type B, samples.

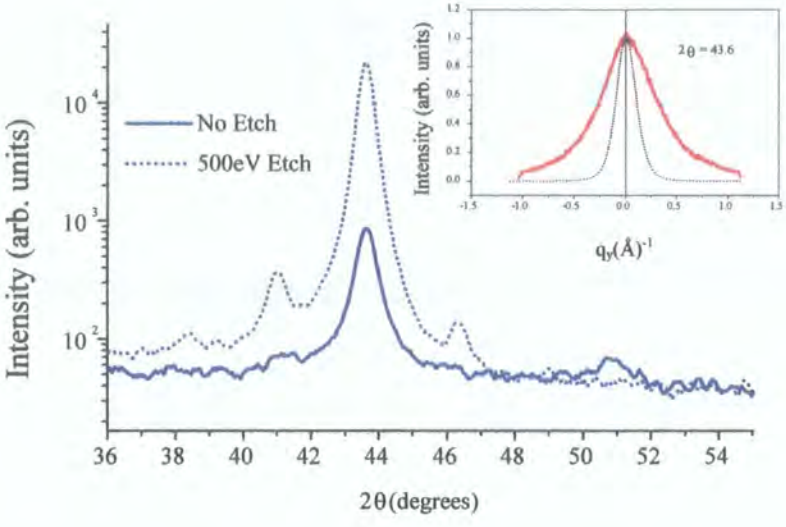


*Figure 5.19. HXRD data from an etched and an unetched type B multilayer. The inset shows rocking curves taken about the compromise 111 Co/Cu peak [36].*

For the etched sample there is a clear increase in the intensity of the compromise {111} Co/Cu peak in comparison to the unetched sample by a factor of around 20 to 30. There is also a simultaneous disappearance of the small {200} peak at $2\theta \approx 51°$. The presence of multilayer satellite maxima, which are clearly visible around the stronger {111} reflection, are a further indication that the layer integrity is largely maintained in the heavily etched sample.

The inset to figure 5.17 shows rocking curves taken at the compromise {111} Co/Cu peak for the same two samples and show the FWHM to decrease with increasing etching energy. This sharp reduction in half width, which corresponds to a reduced mosaic spread out of the film plane as the etching voltage increases, further supports the argument that the etching process encourages the formation of a strongly textured <111> axis in the multilayers.

## 5.8 Summary and Conclusions

The aim of the work reported in this chapter has been to study the effect of substrate etching on the measured GMR for a series of sputter deposited Co/Cu multilayers through extensive structural characterisation. By combining high resolution x-ray scattering measurements with several other complementary techniques it has been possible to characterise extensively the structural and magneto-transport properties of these multilayers. It has been shown that ion beam etching of the substrate has a major effect on the magnitude of the GMR.

X-ray reflectivity measurements combined with careful and detailed modelling calculations show that there is no significant change in interface roughness with etching. The main point of note in this structural characterisation is that the uniformity of interface structure across the range of samples suggests that changes in interface roughness, conformality and layer thickness across the series of samples cannot be driving the observed changes in the GMR to any appreciable extent. Transmission electron microscopy observations are in excellent agreement with the multilayer structure deduced from the reflectivity study.

Transmission Electron Diffraction and High Angle X-ray Diffraction measurements have allowed the crystallinity of the multilayers to be studied. It has been shown that the loss of AF coupling, observed in the PNR and magnetic measurements is associated with a transformation of the crystalline texture of the Co/Cu thin films. It is also clear that as the etching energy is increased the texture is transformed from a randomly oriented polycrystalline film into a well oriented <111> polycrystalline film. This is accompanied by a decrease in the volume fraction of grains otherwise oriented, particularly the <100> orientation. The presence of this relatively small fraction of <100> oriented crystal grains may be crucial for the appearance of a significant GMR. The presence of these grains can easily be missed if careful experiments are not performed [40].

It would appear, therefore that the loss of GMR in the samples is related principally to changes in the crystallographic texture and bulk scattering, in terms of spin-dependent scattering into the split d band in the ferromagnetic layers, rather than

changes in interfacial roughness and associated spin-independent scattering. Similar conclusions with regard to the importance of spin-dependent scattering in the Co/Cu system have also been published [41]. Many earlier investigations [42] have shown an enhancement in the GMR for Co/Cu grown on Fe underlayers. This is known to promote a <200/220> texture and a large GMR, whereas f.c.c underlayers encourage <111> growth and a low GMR. The substrate etching experiments reported in this chapter clearly provide the required interface energy match for the growth of a very strong <111> texture.

Clearly, it is not possible from this work to comment on any effect that variations in the interface roughness would have on the GMR as the interface roughness and morphology in these samples has been shown to remain constant across the series. However, GMR measurements made on Co/Cu multilayers in which the interfaces have been roughened by sputtering at different argon pressures [18] show a correlation with the roughness determined in this study, estimated from the broadening of the first Bragg multilayer diffraction maximum. In this case a minimum average roughness of 16Å corresponds to a maximum in the GMR. There is also an inferred dependence on a <200/220> texture, from studying the variation of GMR with sputtering pressure, with this orientation giving the best GMR. Measurements on sputter deposited and relatively randomly oriented Co/Cu multilayers with extremely flat interfaces, average roughness 1Å, show dramatically large GMR [43].

In summary these results indicate that the loss of AF coupling and associated reduction in the GMR observed as the etching energy is increased is a consequence of the formation of an increasingly strong <111> multilayer texture and a reduction in the volume fraction of <100> oriented grains. The lack of variation in the interface roughness across the series of samples indicates that in this case the observed changes in the GMR are not driven by interfacial effects and are predominantly controlled by the crystalline orientation of the multilayer.

## References for Chapter 5


1. S.S.P.Parkin, R.Bhadra, K.P.Roche,. Phys. Rev. Lett. (66) 2152 (1992)

2. S.S.P.Parkin, Z.G.Li, D.J.Smith, Appl. Phys. Lett. 58, 2710 (1991)

3. G.Binasch, P.Grunberg, F.Saurenbach, W.Zinn. Phys. Rev. B. Vol 39, No. 7 (1989)

4. M N.Baibich, J M.Broto, A.Fert, F.Nguyen Van Dau, F.Petroff, P.Etienne, G.Creuzet, A.Friederich, & J.Chazelas, Phys. Rev. Lett. 61, p2472 (1988)

5. S.S.P.Parkin, R.Bhadra and K.P.Roche, Phys. Rev. Lett., 66, p2152 (1991)

6. R.J.Pollard, M.J.Wilson and P.J.Grundy, J. Magn. Magn. Mater., 151 p139 (1995)

7. A.K.Schmid, D.Atlan, H.Itoh, B.Heinrich, T.Ichinokawa, J.Kirshner PRB Vol 48 No 4 (1993) Rapid comm

8. A.K.Schmid, J.Kirschner. Ultramicroscopy 42-44 483 (1992)

9. Hong. Li, B.P.Tonner. Surface science 237, p141-152 (1990)

10. W.A.Jesser, J.W.Matthews Philos Mag 17 461 (1968)

11. P.J.Grundy. Thin Films -Sputter Deposition. IOP Conference Seminar (1998)

12. D.E.Joyce, Ph.D Thesis, University of Salford, (1998)

13. N.D.Telling, S.J.Guilfoyle, D.R Lovett, C.C.Tang, M.D.Crapper, M.Petty. J. Phys. D: Appl Phys. 31, p472-481 (1998)

14. E.E.Fullerton, D.M.Kelly, J.Guimpel, I.K.Schuller Phys Rev Letters 68, p859 (1992)

15. K.Takanashi, Y.Obi, Y.Mitani, H.Fujimori. J Phys Soc Jpn 61, 1169 (1992)

16. E.E.Fullerton, I.K.Schuller, H.Vanderstraeten, Y.Bruynseraede. Phys Rev B 16, 9292 (1992).

17. E.E.Fullerton, J.Pearson, C.H.Sowers, S.D.Bader, X.Z.Wu , S.K.Sinha. Phys Rev. B 48, 17432 (1993)

18. J.Ben Youssef, K.Bouziane, O.Koshkina, H.Le Gall, M.El Harfaoui, M.el Yamani, J.M.Desvignes and A.Fert, J. Magn. Magn. Mater., 165, 288 (1997)

19. Haruhisa.Ueda, Osamu Jpn J Appl Physics Vol 33. 7173-6178 (1994)

20. S.Honda, S.Ohmoto, R.Imada, M.Nawate. JMMM 126, 419-421 (1993)

21. A.M.Shukh, D.H.Shin, H.Hoffman. J Appl Phys 76 (10) (1994)

22. M.J.Hall, B.J.Hickey, M.A.Howson, M.J.Walker, J.Xu, D.Greig, N.Wiser, Phys. Rev. B 47, 12785 (1993)

23. H.Ueda, O.Litakami, Y.Shimada, Y.Gota, M.Yamamoto. Jpn. J. Appl. Phys. 33 6173 (1994)

24. K.Bouzianne JMMM 165 284-287 (1997)

25. K.P.Wellock. J Appl. Phys. 75 (10) Pt 2B 7055 (1994)

26. J.Barnas, Y.Bruynseraede Europhys Lett 32,176 (1995)

27. S.K.J Lenczowski, M.A.M.Gijs, J.B.Giesbers, R.J.M van de Veerdonk, W.J.M de Jonge, Phys. Rev B 50, p9982 (1994)

28. D.Greig, M.J.Hall, C.Hammond, B.J.Hickey, H.P.Ho, M.A.Howson, M.J.Walker, N.Wiser and D.G.Wright, J. Magn. Magn. Mater., 110, L239 (1992)

29. T.Gu, A.J.Goldman, M.Mao. Phys Rev. B 56, 11 (1997)

30. P.Bruno & C.Chappert, Phys. Rev. Lett. 67, p1602 (1991)

31. W.F.Egelhoff, M.T.Kief, IEEE Trans. Magn., 28, p2742 (1992)

32. J.J.de Miguel, A.Cebollada, J.M.Gallego, R.Miranda, C.M.Schneider, P.Schuster, J.Kirschner. J. Magn. Magn. Mater. 93 1 (1991)

33. J.Penfold, Physica B 173, p1 (1991)

34. C.F.Majkrzak, Physica B 173, p75 (1991)

35. http//ndafleetwood.nd.rl.ac.uk/largescale/crisp/CRISP.htm .

36. D.E.Joyce, B.D.Fulthorpe, C.A.Faunce, T.P.A.Hase, I.Pape, P.J.Grundy. Phys. Rev. B. Vol. 58. No. 9 (1998)

37. V.Holy, T.Baumbach Phys Rev B 49 (15) p10668 (1994)

38. M.Wormington., I.Pape, T.P.A.Hase. B.K.Tanner, and D.K.Bowen, Phil.Mag. Letts. (1996)

39. M.Wormington, K.Sakurai, D.K.Bowen and B.K.Tanner, Mater. Res. Soc Symp. Proc 332, 525 (1994)

40. J.Langer, R.Mattheis, S.Schmidt, St. Senz and T.Zimmermann, J. Magn. Magn. Mater., 156, 19 (1996)

41. M.J.Hall, D.B.Jardine, J.E.Evetts, J.A Leake, R.E. Somekh, JMMM 173,253 (1997)

42. P.J.Grundy, R.J.Pollard, M.E.Tomlinson, JMMM 126, 516 (1993)

43. C.H.Marrows, N.Wiser, B.J.Hickey, T.P.A.Hase, B.K.Tanner, C.W.Lehmann. J. Phys. C. 11, p81-88 (1999)

# Chapter 6

# The Propagation of Interface Structure in Co/Cu and Co/Pt Multilayers.

## 6.1 Introduction

In the previous chapter, x-ray scattering techniques were used to characterise extensively the Co/Cu multilayer system with regard to interface and multilayer structure. The interface roughness in such systems was shown to be highly correlated in nature and of uniform magnitude throughout the multilayer stack. However, in all cases, the bilayer number, and hence the total multilayer stack thickness, remained constant. It was, therefore, not possible to draw any conclusions as to whether this conformal growth would continue indefinitely or have a limiting out-of-plane length scale as the multilayer grows in thickness. Multilayer growth can be complicated by the fact that it is possible for modulations to occur in the surface energy conditions as the layers are deposited and this may in turn lead to variations in the progression of the interfaces through the stack.

The key question therefore, that the work discussed in this chapter aims to address, is how the interface morphology propagates from the substrate to the surface as the number of bilayers in the structure is increased. The first section of this chapter relates to the Co/Cu system, the intention being to discover whether there is a finite out-of-plane length scale over which the conformal growth, already observed in chapter 5, propagates. Observations from the Co/Cu system are then compared and contrasted with a similar set of Co/Pt samples. The formation of a columnar growth mode in Co/Pt has been observed, through cross sectional TEM micrographs, in other studies. Zeper *et al.* [1] found the grains, in sputtered Co/Pt, to grow in a columnar manner, in a close packed arrangement, throughout the entire stack whilst still retaining the individual layer definition. A fine columnar structure was also observed by Hashimoto *et al.* [2] in the sputtered Co/Pt system. Other high resolution TEM measurements [3] have

indicated the interfaces to be semi-coherent in nature, consistent with a columnar growth mode.

However, microscopy techniques, by definition, provide only a localised picture of interface morphology, and require additional sample preparation. Grazing Incidence X-ray Scattering techniques are ideally suited to following the propagation of interface morphology through a multilayer. Further to this, x-ray measurements provide a global method by which to average laterally over micron length scales in the plane of the film with an additional sensitivity to out-of-plane correlations between the many buried interfaces in a multilayer.

Interface structures within multilayer systems can have a profound effect on their physical and magnetic properties. In the Co/Pt system surface anisotropy due to the interfaces, critical in the production of perpendicular magnetisation, contrives to pull the magnetisation out of the plane. Co/Pt multilayers are known to exhibit a high degree of perpendicular anisotropy [4] which is lost when the interface structure becomes less well defined, indicating the strong interface dependence of this type of anisotropy. This perpendicular magnetisation is of great importance with regard to the microstructural properties of Co/Pt multilayers and may be advantageous in the field of high density recording media. There are also applications in the field of magneto-optics [5,6] where Co/Pt produces strong signals at the blue wavelength [6,7] and possesses thermo-magneto optic stability [8,9] as interface induced anisotropy tends to increase the coercivity and reduce the Curie temperature [10].

## 6.2 The Samples

A series of Co/Cu multilayer films were grown on etched silicon using the same magnetron sputtering technique discussed in chapter 4.

All samples were nominally:

$$N * \{10\text{Å Co} / 10\text{Å Cu}\} + 10\text{Å Pt} \quad \text{where } N = 1,3,6,9,12,16$$

The deposition rates at ambient temperature and under an Argon partial pressure of 0.4 Pa were 0.4, 0.5 and 0.9Å per second for Co, Cu and Pt respectively. The base pressure in the sputtering chamber was better than $10^{-5}$ Pa.

The series of Co/Pt samples that will be discussed towards the end of this chapter were grown using the same apparatus with a 50Å Pt buffer on glass substrates, with nominal structure:

$$N * \{4\text{Å Co} / 20\text{Å Pt}\} \qquad \text{where } N = 1,5,10,15,22$$

Greaves *et al.* [10] found that the perpendicular anisotropy in Co/Pt peaked for a Co thickness of around 4Å. The samples in this study were therefore grown at such a nominal thickness, which conveniently corresponds to a sensible thickness for recording media. At greater thicknesses a smaller proportion of the Co atoms are at the interfaces and the surface anisotropy contribution decreases. The same effect also occurs for discontinuous films thinner than 3Å. All of the Co/Pt multilayers exhibited a single diffraction peak matching that of (111) oriented f.c.c platinum.

## 6.3 The Co/Cu System

The structural analysis of the Co/Cu system can be divided into three main sections of interest. Firstly the progression of interface structure with increasing bilayer number is discussed qualitatively by studying a series of off-specular, grazing incidence, reflectivity scans. In the second section this low angle reflectivity data is extended to specular and transverse diffuse measurements which are then combined with extensive modelling in order to be able to quantify and support the previous qualitative observations. Finally these structural data are studied in conjunction with magnetic measurements to establish an overall picture of the progression of interface structure and the effect this has on the magnetic properties of the system.

### 6.3.1 High Angle X-ray Diffraction (HXRD)

High angle diffraction measurements, undertaken by D.E. Joyce, taken through the compromise (111) peak show the bilayer progression sequence, figure 6.1.

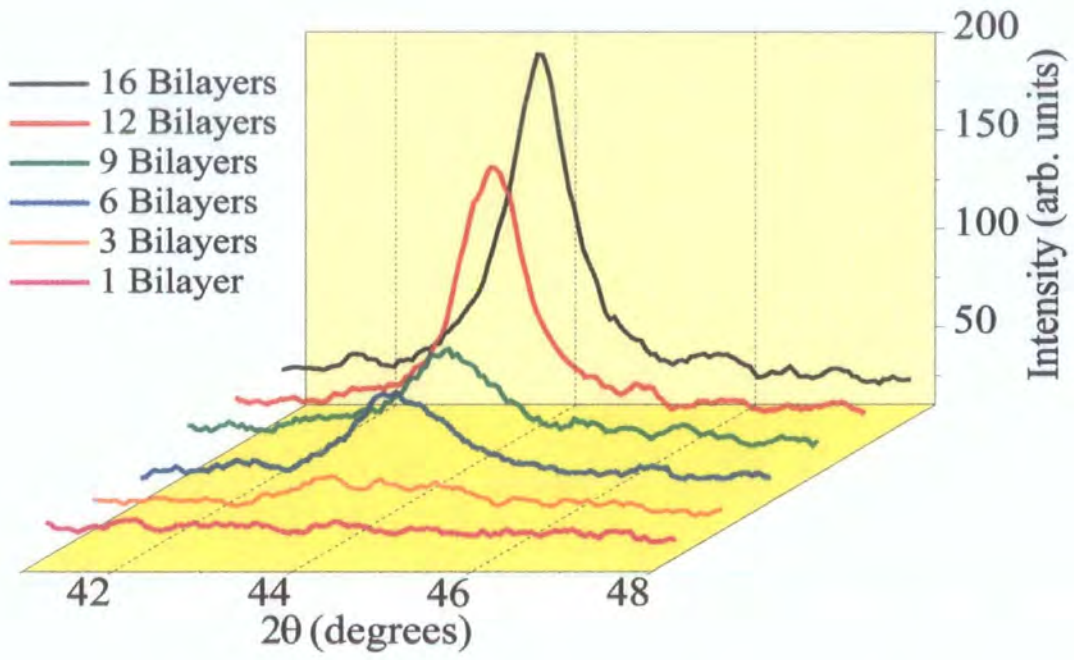


*Figure 6.1. High angle diffraction scan taken through the compromise (111) peak for varying bilayer number, N.*

The intensity of this peak can clearly be seen to increase with increasing bilayer number. This increase in intensity as a function of bilayer number is of course entirely expected with an increase in the volume of material in the sample. It is more difficult to study the uniformity of the crystallinity in the stack. However, TEM measurements performed elsewhere [11] show the texture establishes itself as a f.c.c type structure within 10 to 20Å of the substrate surface, the upper limit of which corresponds to a maximum of one bilayer repeat in this case.

### 6.3.2 Longitudinal Diffuse (off-specular) Scans

An immediate qualitative estimate as to the degree of conformal growth within a multilayer stack can be made by looking at the grazing incidence off-specular scan. In section 2.6 the way in which roughness which is highly correlated in nature effects the modulations in the off-specular scan was discussed. Without any need for modelling

initially, the off-specular features can qualitatively reveal a great deal of information about interface propagation and conformality.

Figure 6.2 shows a series of off-specular scans taken for each of the samples with the bilayer number varying from $N$=1 to $N$=16. In all cases the off specular scan (red) exhibits the same periodic features, namely the Kiessig fringes and the Bragg peak, as the respective specular scan (blue).

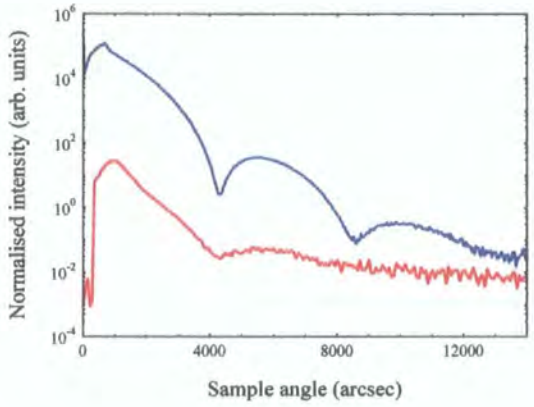


a) $N = 1$

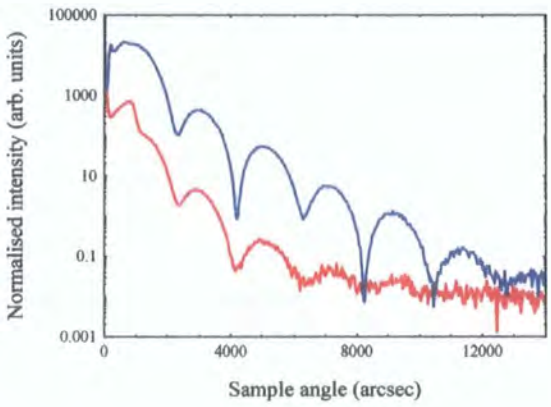


b) $N = 3$

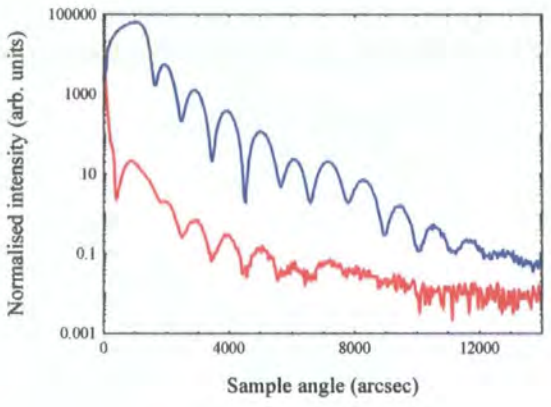


c) $N = 6$

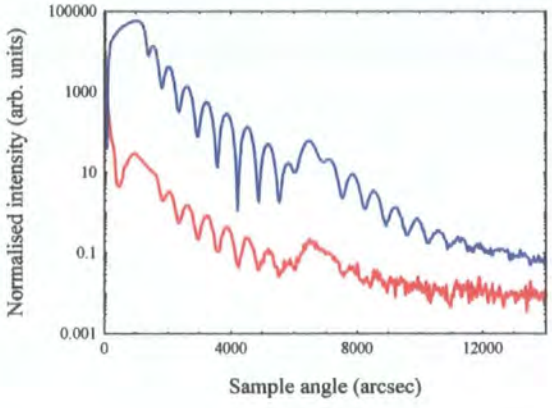


d) $N = 9$

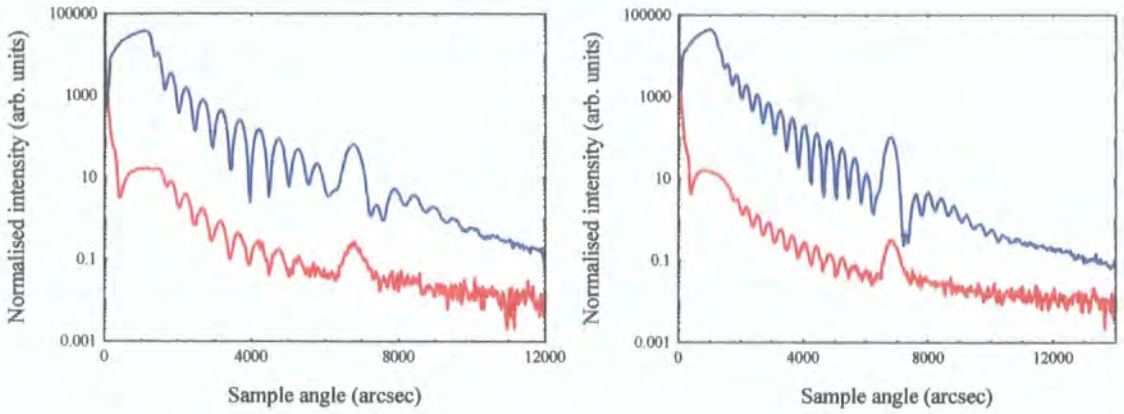


e) $N = 12$ f) $N = 16$

*Figure 6.2. Co/Cu off-specular scans for varying bilayer number, N. Taken at the Cu absorption edge, λ=1.3798Å.*

It is clear from these scans that as the bilayer number increases the off-specular Bragg peak and the high frequency Kiessig fringes remain. This indicates that as the stack thickness increases the interface roughness is not only correlated within each bilayer repeat but across the entire stack thickness from the substrate upwards to the cap. Off-specular measurements, therefore, indicate that the growth of this system is highly conformal in nature. In order to support this quantitatively, specular and transverse diffuse measurements were modelled in order to attempt to verify the nature of this roughness at the interface and what proportion is indeed correlated between successive layers.

## 6.3.3 Specular and Transverse Diffuse Measurements

Across the series of 6 samples extensive specular and transverse diffuse measurements were made. Through a combination of these scans all aspects of the interface morphology in the multilayer structures could be characterised. Two x-ray wavelengths were used, one at the Cu absorption edge, 1.3798Å, to make use of the anomalous dispersion enhancement to the Cu scattering factor, and one away from the edge. This allows the scatter that originates solely from the multilayer to be distinguished from that arising from the cap, as well as providing a second data set for modelling.

For each sample, at each wavelength, 3 transverse diffuse scans were taken, one at and two away from the Bragg condition. These scans are primarily sensitive to correlated and uncorrelated roughness respectively. Due to the large amount of experimental data only a representative selection of best fit simulations for each of the samples are shown here.

In all cases it is possible to obtain simulated fits in very good agreement with the experimental data. It can be seen in some cases that the problem of simulating the region of the specular just beyond the Bragg peak, already discussed in chapter 5, occurs once again.

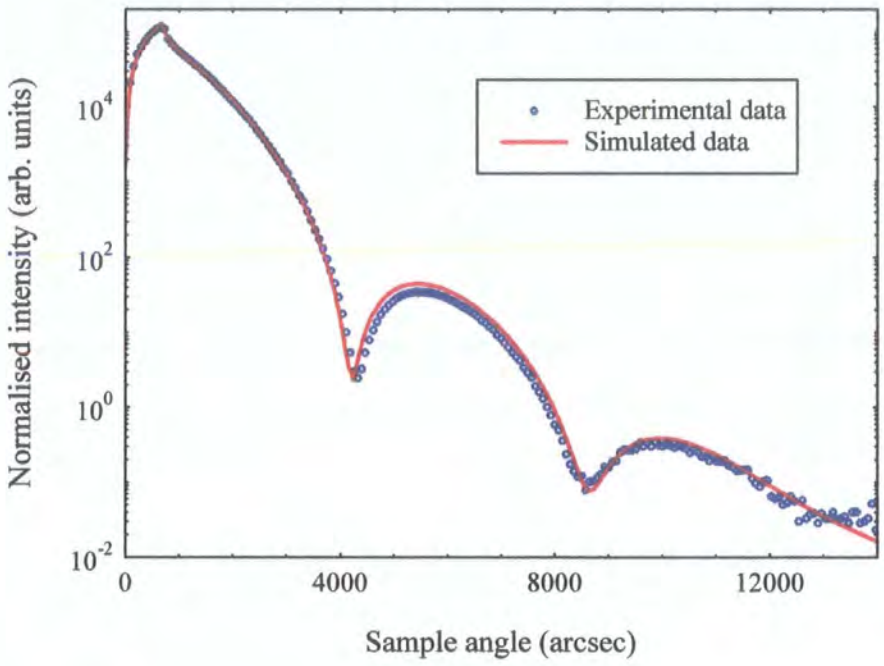


*Figure 6.3 a). Specular data (dots) and fit (line) for N = 1, λ=1.3798Å.*

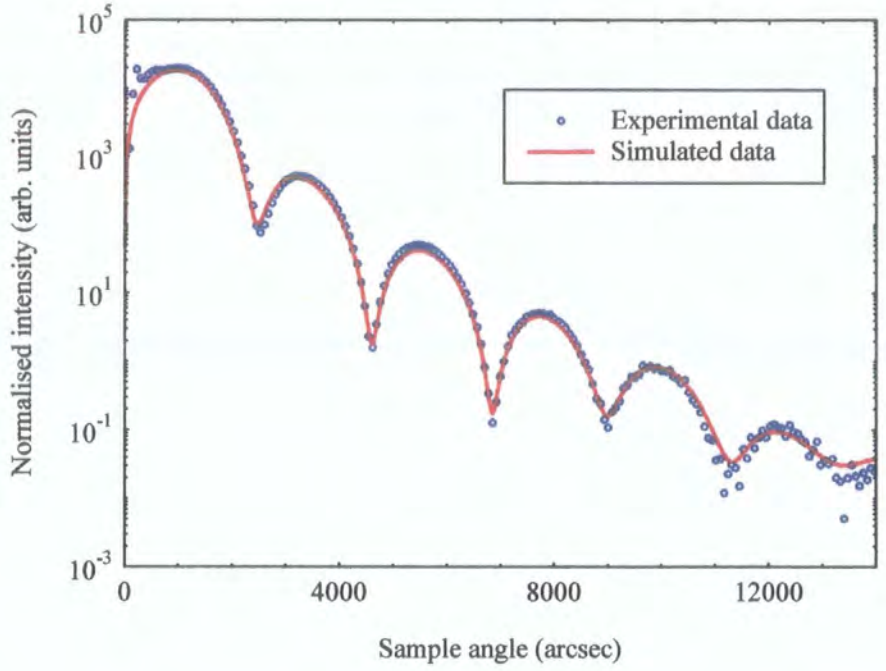


*Figure 6.3 b). Specular data (dots) and fit (line) for N = 3, λ=1.48Å.*

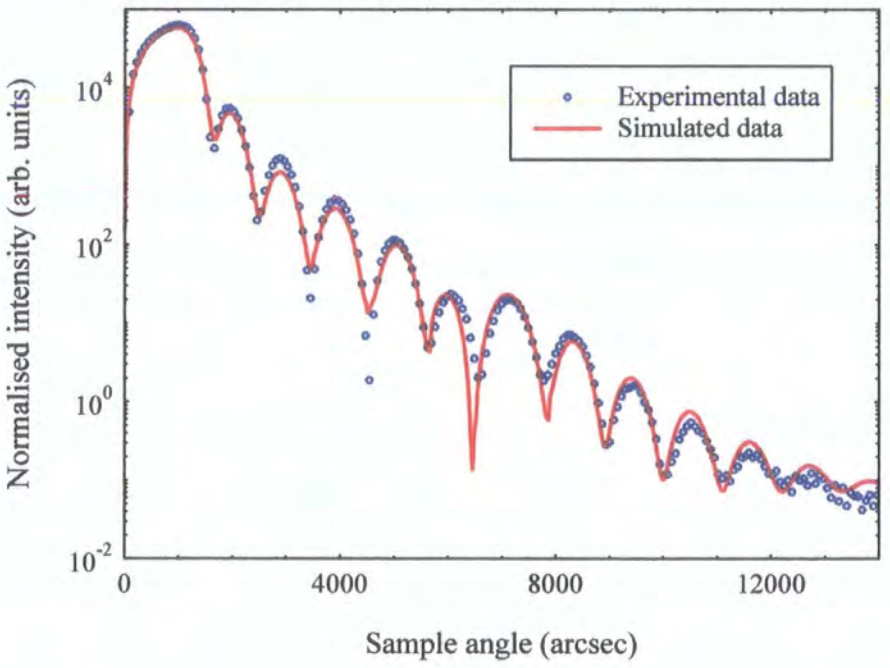


*Figure 6.3 c). Specular data (dots) and fit (line) for N = 6, λ=1.3798Å.*

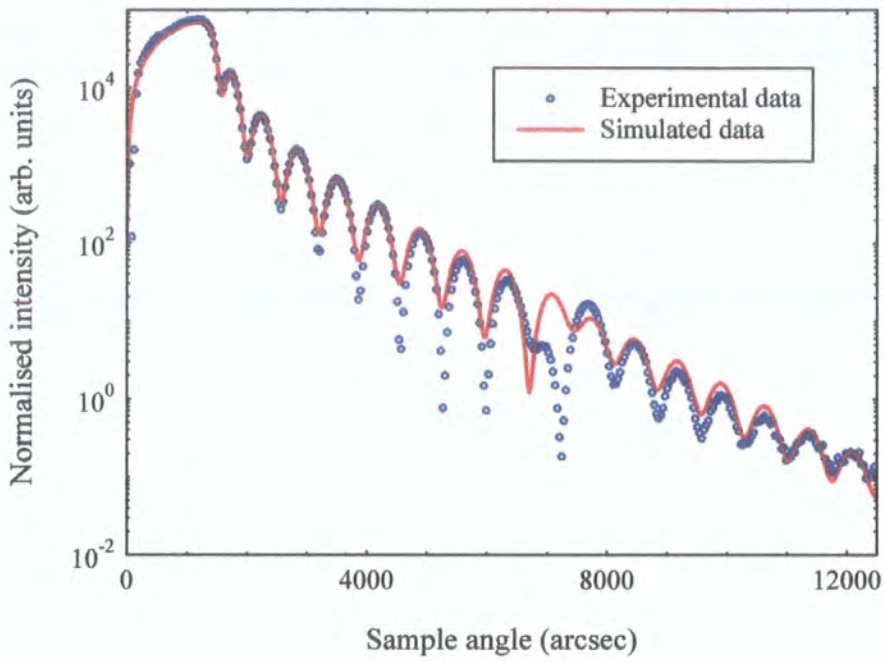


*Figure 6.3 d). Specular data (dots) and fit (line) for N = 9, λ=1.48Å.*

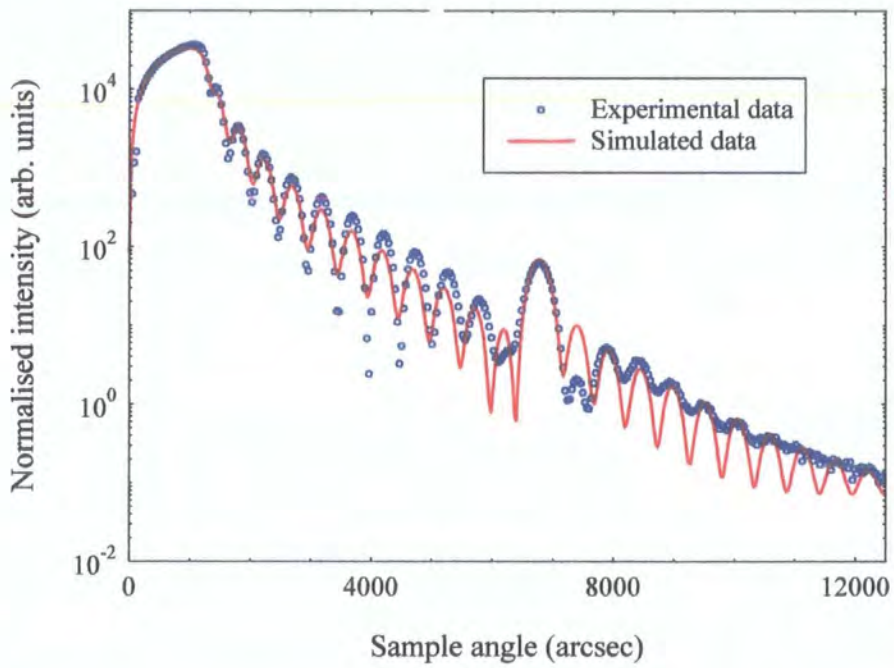


*Figure 6.3 e). Specular data (dots) and fit (line) for N = 12, λ=1.3798Å.*

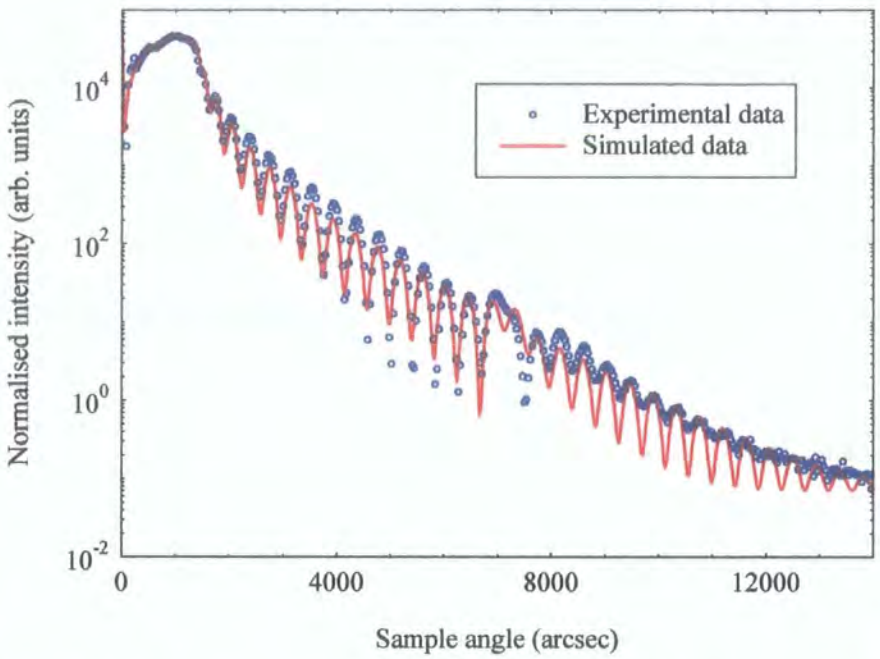


*Figure 6.3 f). Specular data (dots) and fit (line) for N = 16, λ=1.48Å.*

As the number of coherently scattering interfaces in the multilayer increases the specular Bragg peak becomes more intense and is more well defined as the amount of coherent interface scattering increases. For a system in which the vertical, out-of-plane, length scale for conformal growth is in excess of the total stack thickness a similar increase in intensity with bilayer number should be observed for the off-specular Bragg peak also.

For each value of *N*, the ratio of the specular and off-specular Bragg peak intensity should remain constant if the conformal growth, inferred from the off-specular scans, is indeed representative of the sample structure. The measured ratios in table 6.1 do indeed show this to be the case. One caveat to this however, is that great care must be taken in systems possessing a capping layer due to the fact that small variations in the cap thickness may cause considerable changes in the reflectivity profile [12].

| $N$ | Specular, $I_{Bragg1}$ | Off-specular, $I_{Bragg2}$ | $(I_{Bragg1}/ I_{Bragg2})$ |
|---|---|---|---|
| 6 | 19.2 | 0.07 | 274 |
| 9 | 59.6 | 0.22 | 271 |
| 12 | 59.8 | 0.22 | 272 |
| 16 | 105.0 | 0.39 | 270 |

*Table 6.1. The ratio of specular and off-specular Bragg peak intensities for varying N.*

However, it is the simulation of transverse diffuse measurements that yields the most important information about the in-plane structure and the degree of conformality both within the bilayer and across the total stack thickness. Transverse diffuse data from several different scattering vectors was measured and simulated for each sample data set.

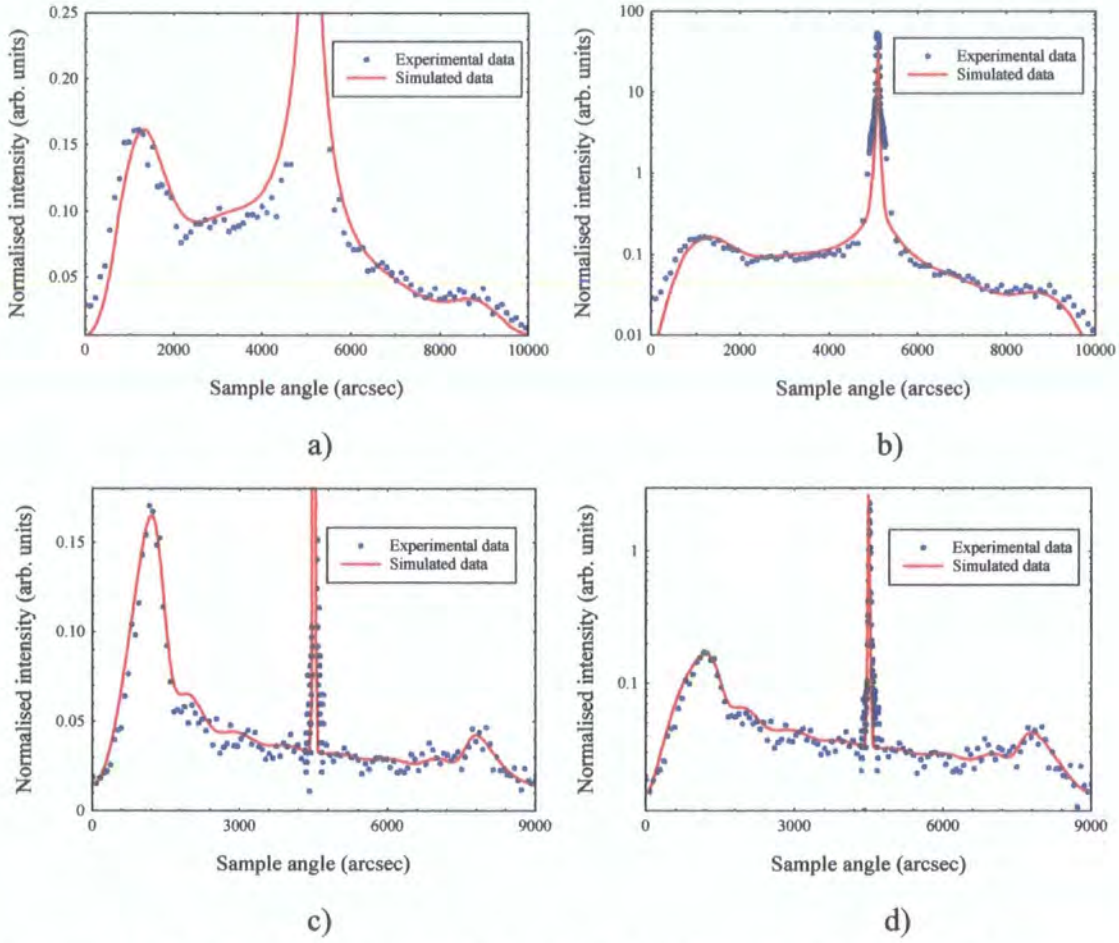


*Figure 6.4 a) N = 3,Bragg peak, λ=1.3798Å. b) log scale c) N = 3,Kiessig minimum, λ=1.3798Å d) log scale.*

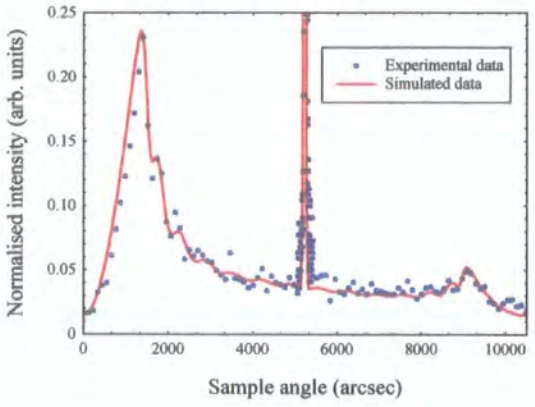


e)

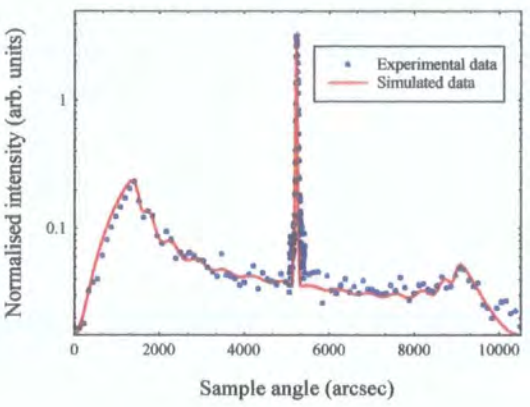


f)

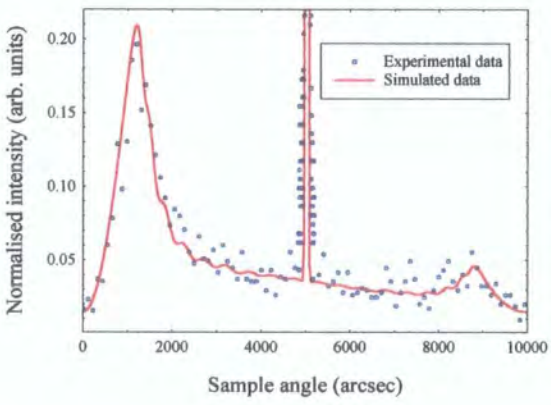


g)

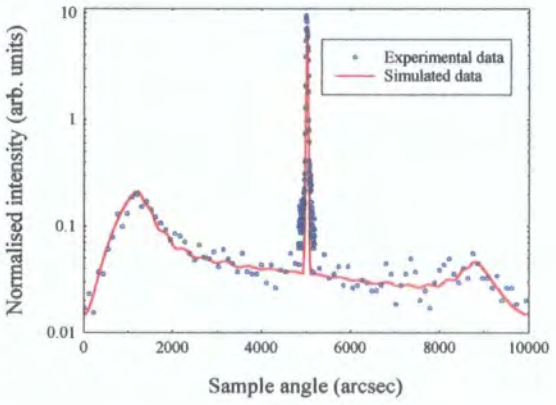


h)

*Figure 6.4 e) N = 9, Kiessig minimum, λ=1.48Å. f) log scale g) N = 12, Kiessig minimum, λ=1.3798Å h) log scale.*

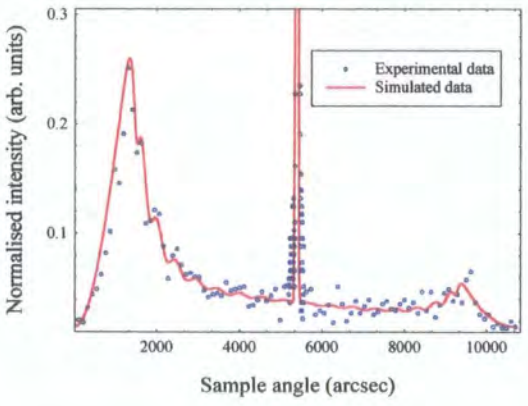


i)

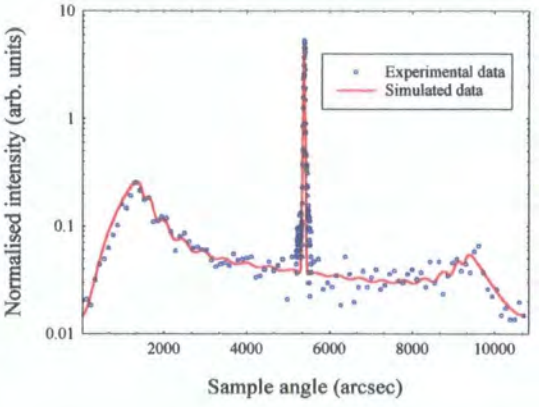


j)

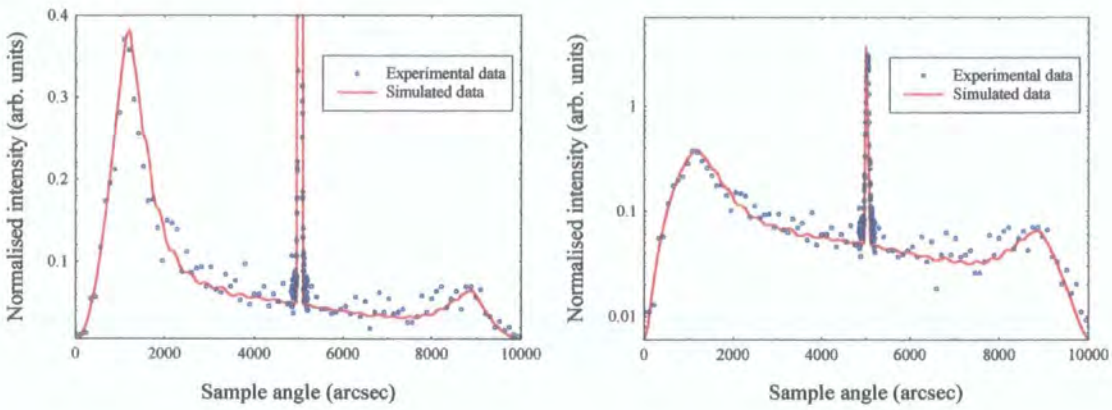


*Figure 6.4 i) N = 12, Kiessig maximum, λ=1.48Å. j) log scale k) N = 16, Kiessig minumum, λ=1.3798Å l) log scale.*

From the modelling it is also possible to determine the lateral correlation length, any variations in which across the series may indicate a loss of conformality. A selection of best fit transverse diffuse simulations are shown in figure 6.4. All aspects of the structure of the multilayer film are summarised in table 6.2.

| Bilayer No. | Co thickness (Å) | Cu thickness (Å) | Pt thickness (Å) | $\sigma_{correlated}$ (Å) | $\sigma_{uncorrelated}$ (Å) | $\xi$ (Å) | h |
|---|---|---|---|---|---|---|---|
| 1 | 10.4±0.3 | 10.4±0.3 | 4.3±0.3 | 3.3±0.3 | 1.8±0.3 | 135±5 | 0.50±0.05 |
| 3 | 10.5±0.3 | 10.6±0.3 | 4.2±0.3 | 3.4±0.3 | 1.8±0.3 | 135±5 | 0.50±0.05 |
| 6 | 10.3±0.3 | 10.5±0.3 | 4.4±0.3 | 3.3±0.3 | 1.8±0.3 | 135±5 | 0.50±0.05 |
| 9 | 11.2±0.3 | 11.3±0.3 | 4.4±0.3 | 3.3±0.3 | 1.8±0.3 | 135±5 | 0.50±0.05 |
| 12 | 10.7±0.3 | 10.9±0.3 | 4.1±0.3 | 3.5±0.3 | 1.8±0.3 | 135±5 | 0.50±0.05 |
| 16 | 10.7±0.3 | 10.9±0.3 | 4.1±0.3 | 3.5±0.3 | 1.8±0.3 | 135±5 | 0.50±0.05 |

*Table 6.2. Multilayer structure parameters determined from x-ray scattering simulations.*

As indicated in the off-specular data, the interface roughness is predominantly correlated in nature in each of the 6 samples with no evidence of compositional grading. Further to this, the lateral correlation length, $\xi$, and fractal parameter, $h$, are constant across the range of samples. One exception to the general uniformity of all aspects of the structure across the series is that in the case of the 9 bilayer sample the layer thickness for the Co and Cu is slightly larger, although this thickness variation has no effect on the interface morphology in this sample, which is the primary concern. The consistency in the Pt capping layer thickness, shown in the simulations, suggests that the high degree of conformality, inferred from the similar specular and off-specular Bragg peak intensity ratios of table 6.1 is valid. It is now possible to say that the apparent high degree of conformality observed in the off-specular data would indeed appear to represent the correct growth mode, however the modelling serves to give further weight to this argument.

Over the range of $N$ studied in this experiment, corresponding to a variation in stack thickness from approximately 24Å to 300Å, there is no observed loss of growth conformality, with the ratio of correlated to uncorrelated roughness, and the lateral correlation length remaining constant across the series. This means that if an out-of-plane length scale for conformal growth does exist it must be considerably greater that 300Å.

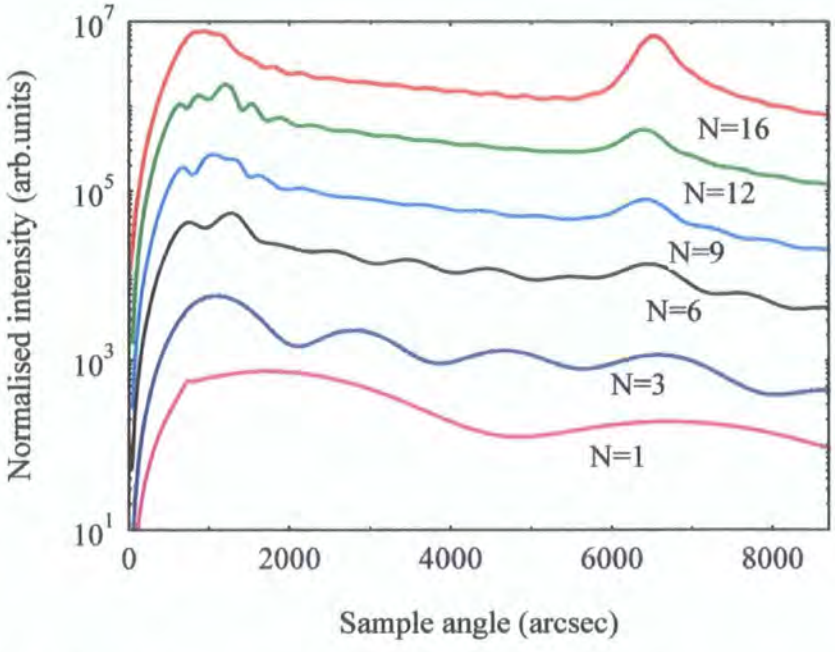


*Figure 6.5. Co/Cu Off-specular simulations with a fixed vertical correlation length of 150Å.*

In order to study the effect that a fixed vertical correlation length, perpendicular to the plane of the film, would have on the shape of the off-specular scatter, simulations were performed for a Co/Cu system in which the vertical correlation length was set at a nominal value of 150Å. The results are shown in figure 6.5.

For small values of $N$ for which the total stack thickness is less than that of the vertical correlation length there are interference fringes in the off-specular scan. As the value of $N$ increases to the point where the total stack thickness is greater than that of the vertical correlation length these fringes disappear rapidly, although the off-specular Bragg peak remains. This indicates that as the bilayer number increases the conformality between adjacent bilayers is largely retained but is lost across the entire stack thickness.

These simulations are in sharp contrast to the actual data in figure 6.2 in which the off-specular Bragg peak and Kiessig fringes are retained for all bilayer numbers. Once again, this indicates no out-of-plane length scale limit for conformal growth in the Co/Cu system for stack thicknesses up to at least 300Å. This is in good agreement with TEM studies, discussed in Chapter 5, in which TEM images, defocused to enhance the layer contrast, indicate a high degree of conformal growth within the Co/Cu stack and show no evidence of a change in lateral interface structure as $N$ increases.

### 6.3.4 Magnetic Measurements

The magnetic data in this section was taken by D.E.Joyce at the University of Salford on a laboratory Vibrating Sample Magnetometer (VSM). Magnetisation data normalised to sample area is shown in figure 6.6 a). When the curves are normalised, by estimating the magnetically active volume of a Co-Cu-Co trilayer to be two thirds of the bulk volume, the values for the magnetisation are in agreement with that of bulk Cobalt. It should be noted that the magnetic moment of the single bilayer system is below the sensitivity threshold of the VSM.

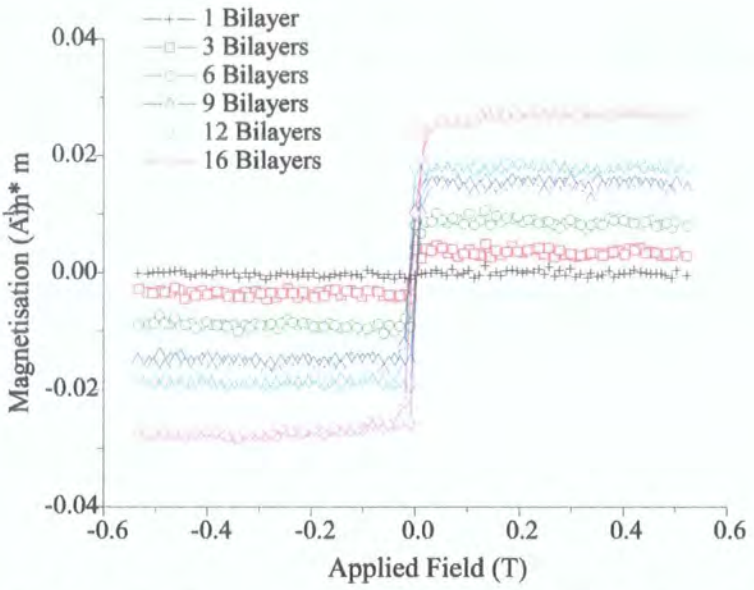


*Figure 6.6 a). Magnetisation normalised to sample area. Courtesy of D.E. Joyce.*

The curve for the 9 bilayer sample is offset in position away from the 6 bilayer curve towards the 12 bilayer curve, when, it should in fact lie midway between the two if the sample structures were nominally identical. This would suggest that the magnetic volume of this sample is disproportionally larger than in the other samples. This observation is supported by the x-ray measurements summarised in table 6.2 indicating that for the 9 bilayer sample the cobalt layer is indeed slightly thicker than in all of the other samples, thereby increasing the magnetic bulk of that system.

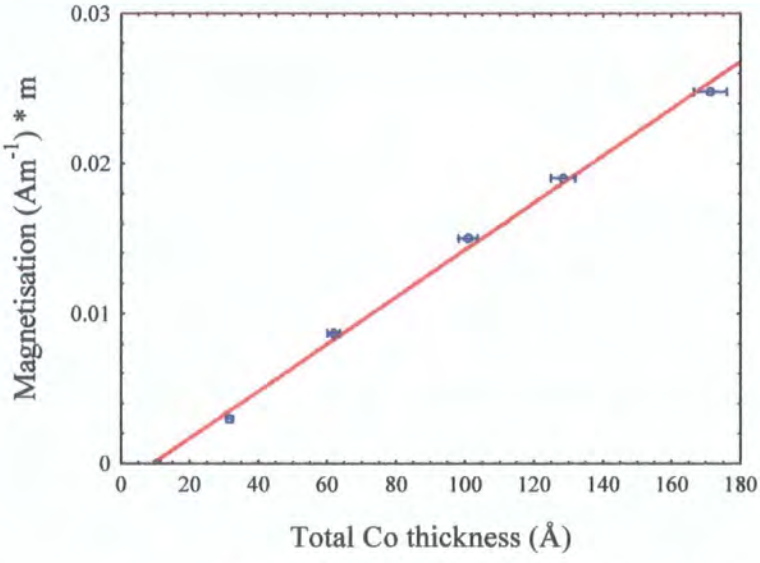


*Figure 6.6 b) Magnetisation as a function of total cobalt thickness as measured from the x-ray simulations.*

The linear relationship between the magnetisation and the total cobalt thickness is shown in figure 6.6 b). Although the x-ray reflectivity simulations show the total cobalt thickness in the 3 bilayer sample to be approximately 32Å, much better agreement is obtained between the measured and expected values of the saturation magnetisation if the magnetic layers in the 3 bilayer system are assumed to be 25Å thick in total. This 'missing' Co layer, from the point of view of the magnetisation measurements, can be attributed to the Co layer immediately adjacent to the substrate being rendered magnetically 'dead' due to the mixing of the cobalt with silicon and oxygen species at the substrate interface, and results in the non-zero intercept of figure 6.6 b). This phenomenon has been observed in other studies [13] and is of great importance with regard to sensor and data storage applications as the magnetically active volume of such systems can be reduced appreciably. This intermixing of the substrate and lower layers was also evident in the specular modelling, discussed earlier, in which there was difficulty fitting the region just beyond the first Bragg peak in some scans.

## 6.4 The Co/Pt System

In the process of sputter deposition, one of the most important factors influencing the growth morphology of the system is the ratio of deposition temperature to melting point ($T/T_m$) for each of the deposited species. There are notable differences in this ratio between the Co/Cu and Co/Pt systems due to the high melting point of Pt compared to Co and Cu. In this section specular and off-specular reflectivity data for the series of Co/Pt mutilayers is compared and contrasted, at a predominantly qualitative level, to that already discussed for the Co/Cu system and notable differences are observed.

### 6.4.1 Longitudinal Diffuse (off-specular) Scans

Once again the propagation of interface structure within the increasingly thick multilayers has been studied by means of a series of off-specular measurements. A series of off-specular scans, along with the respective specular scans, are shown in figure 6.7.

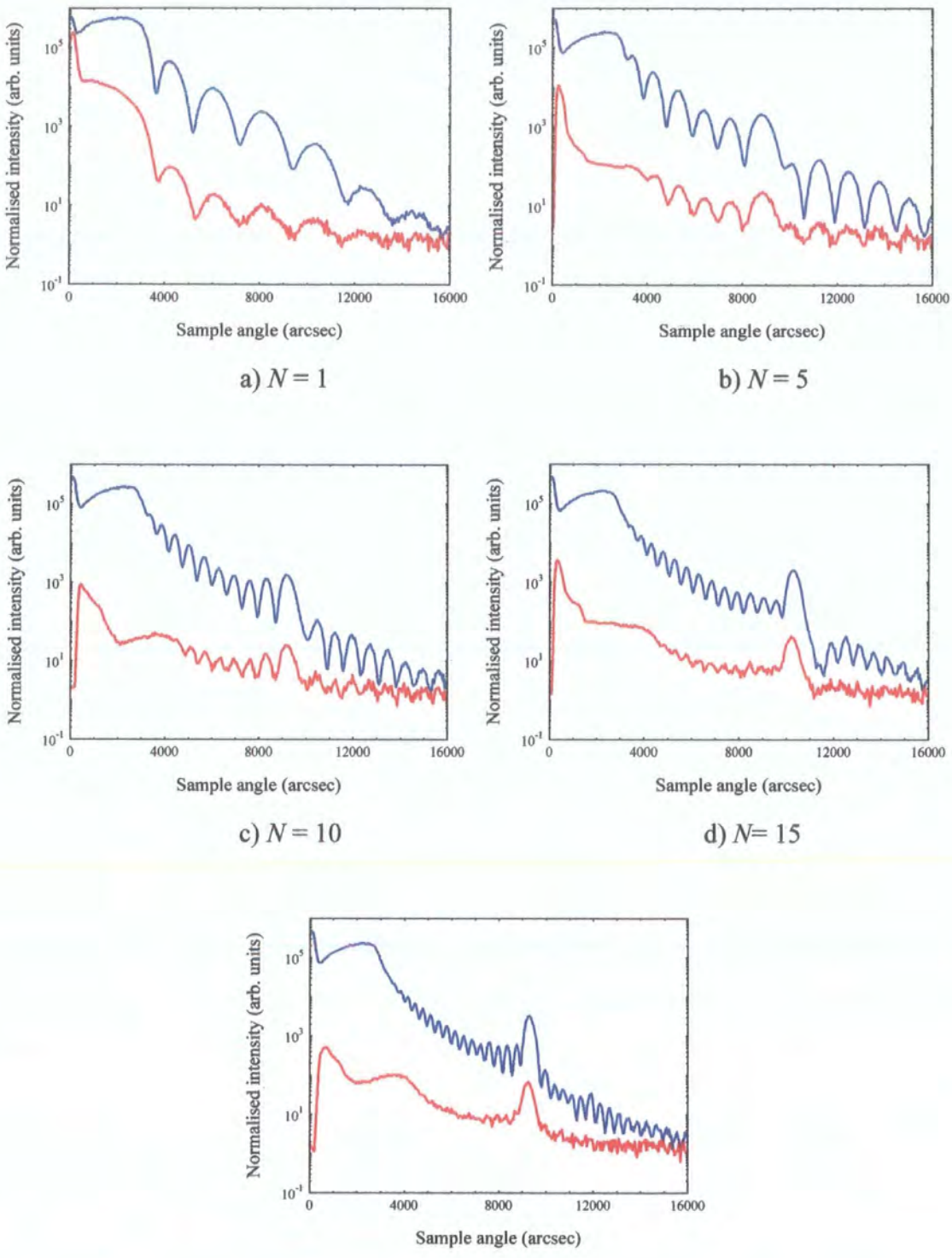


*Figure 6.7. Co/Pt off-specular scans for varying bilayer number, N. λ=1.3798Å.*

In the Co/Cu system the presence of the same periodic features in both the specular and off-specular scans was observed for all bilayer numbers. However, there is a marked difference in the case of Co/Pt. Initially for small bilayer number, $N$, the periodic features exist in both the specular and off-specular data. This, as discussed earlier, means that a high degree of conformality exists not only between each successive bilayer repeat but also across the entire multilayer stack thickness. The interface roughness is highly correlated in nature with a uniform lateral correlation length at the interface. In the Co/Cu system this was found to be the case up to and beyond a total stack thickness of 300Å. However, in the Co/Pt system as the bilayer number reaches $N$=15 the off-specular Kiessig fringes start to become less well defined and by $N$=22 they are lost completely, although the off-specular Bragg peaks do remain indicating that conformality between successive repeats is retained. Loss of the Kiessig fringes and, by definition, the loss of correlation between interfaces at the top and bottom of the multilayer, allows an out-of-plane length scale over which conformal growth occurs in the stack to be estimated to be of the order of 360Å. This places the critical bilayer number for conformal growth in this system at around $N$=15.

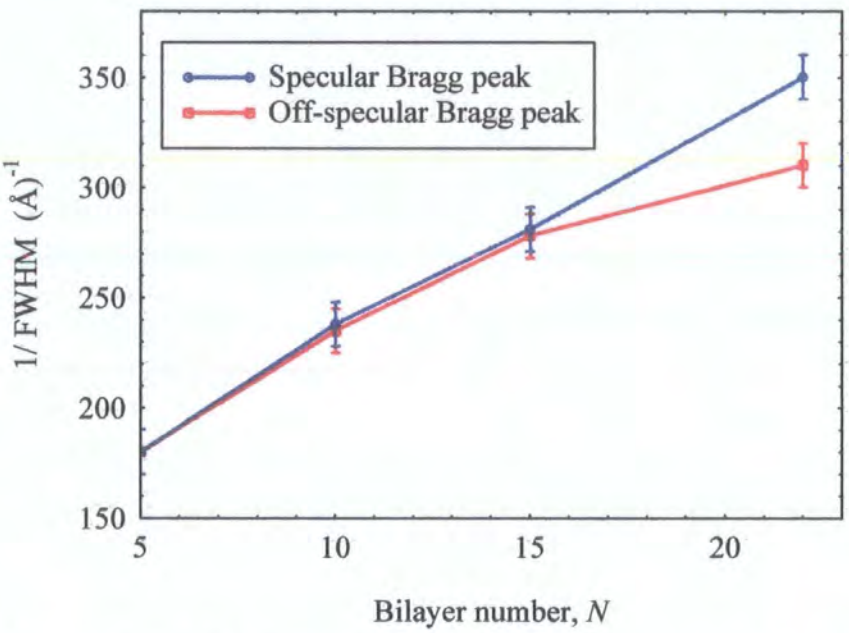


*Figure 6.8. Inverse FWHM of the specular and off-specular Bragg peak as a function of bilayer number, N.*

The inverse FWHM of the specular and off-specular Bragg peak, as a function of $N$, are shown in figure 6.8. The specular Bragg peak becomes sharper and more

intense as the bilayer number increases, as expected due to the increase in the number of coherently scattering interfaces. The off-specular Bragg peak follows the same trend up to $N$=15 but then deviates, marking the point at which out-of-plane correlation is lost. From this point onwards the rate of increase of the inverse FWHM of the off-specular Bragg peak is reduced and would eventually saturate for larger $N$, with additional bilayers no longer contributing to further coherent off-specular scatter at the Bragg condition.

In figure 6.9 a series of off-specular simulations for Co/Pt show the effect of varying the number of bilayers form $N$=5 to $N$=25 for a system in which the interface roughness is highly correlated in nature. Both off-specular Kiessig fringes and Bragg peaks remain as $N$ increases although this clearly contrasts with the actual data in figure 6.7. The effect of fixing the bilayer number and varying the relative fraction of the roughness which is correlated is shown in figure 6.10 in which $N$ is kept constant at 15 bilayers.

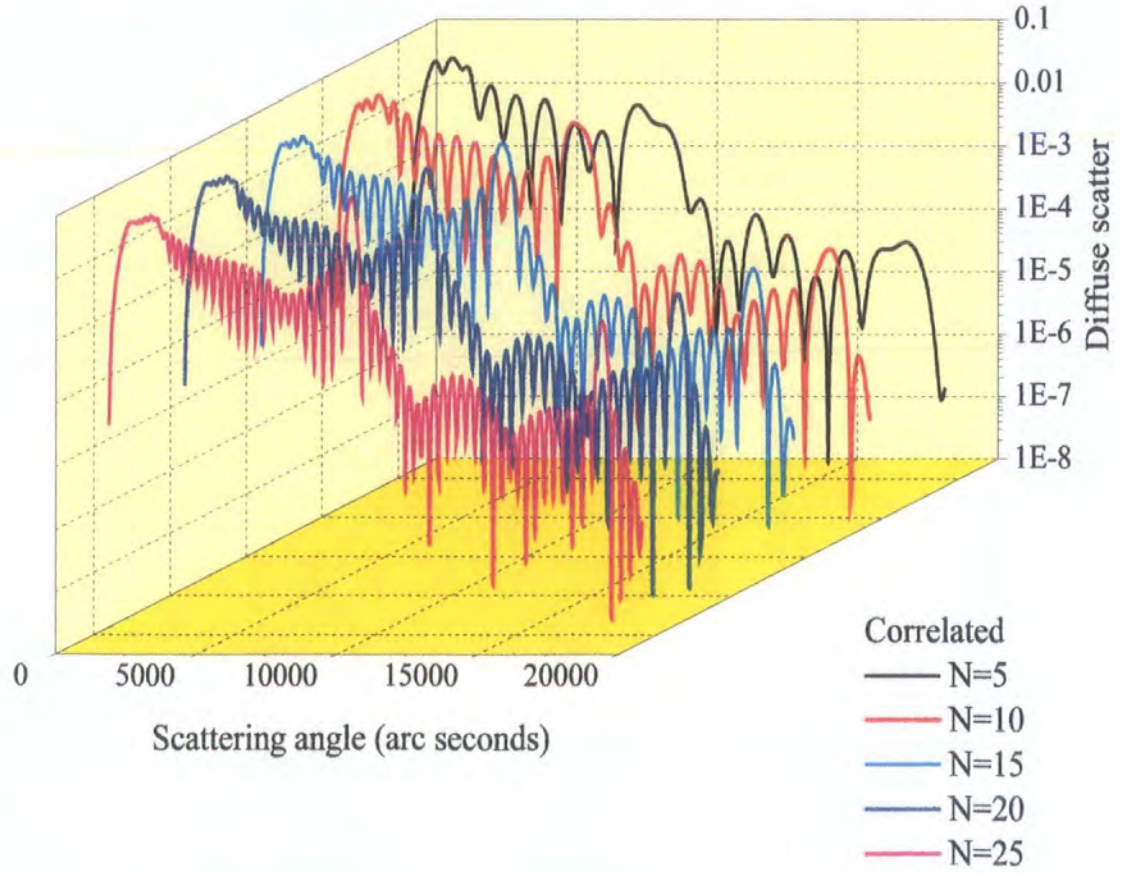


*Figure 6.9. Off-specular simulations for highly correlated Co/Pt.*

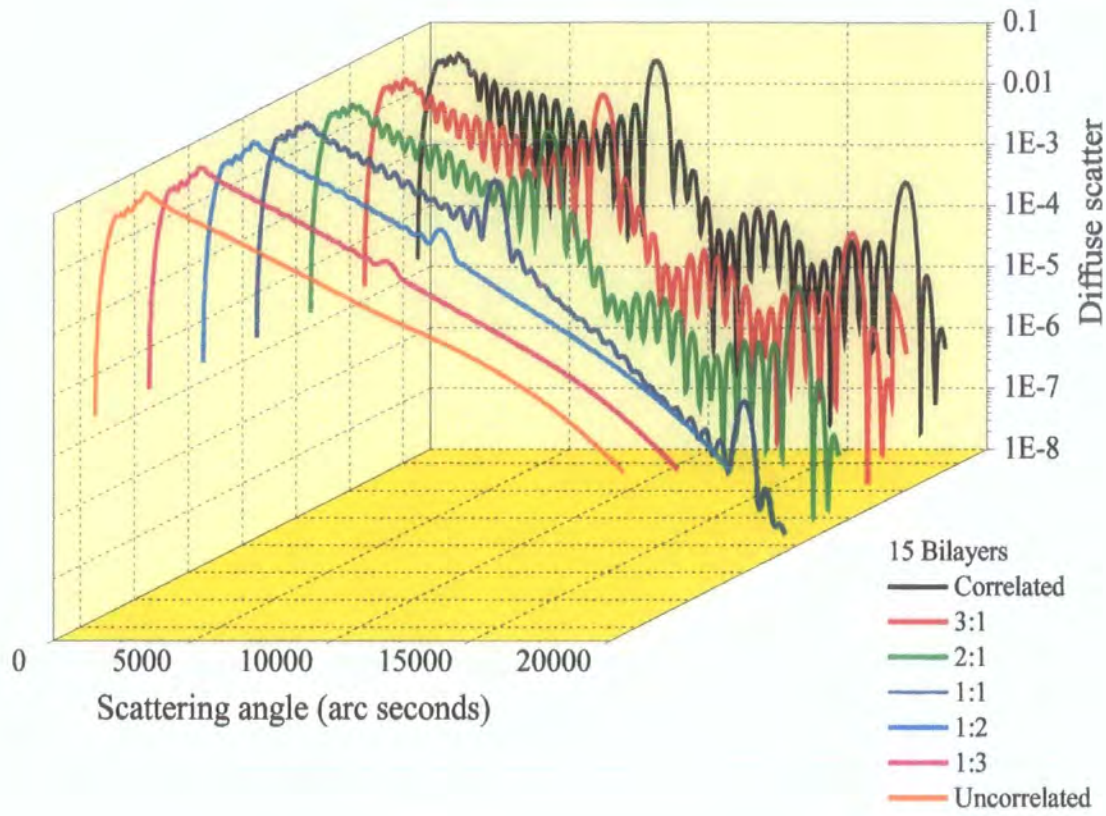


*Figure 6.10. Off-specular simulations for Co/Pt, N=15.*

The actual experimental data both exhibits and lacks some of the features in figures 6.9 and 6.10. The way in which the off-specular Bragg peak remains, as $N$ increases, in figure 6.9 matches the experimental data although the way in which the Kiessig fringes are retained does not. In figure 6.10 the Kiessig fringes are lost as the roughness becomes less correlated but the Bragg peak is also lost, something which is not observed in the actual data. By combining the observations from the off-specular simulations with the true data it is possible to visualise the processes occurring as the stack thickness increases.

Initially for small $N$ there is a high degree of conformality between the top and bottom of the multilayer stack as a consequence of the high proportion of correlated roughness and a uniform average lateral correlation length. As the stack thickness increases, with increasing bilayer number, the highly correlated roughness at the interfaces remains, thereby retaining the conformality between adjacent bilayers, indicated by the persistent off-specular Bragg peak. However, conformality across the

entire stack thickness is lost, most probably due to a small change in the lateral correlation length between successive layers. This small change has a negligible effect over one or two bilayer periods, hence the off-specular Bragg peak is not affected, but over the entire stack thickness the effect is more noticeable.

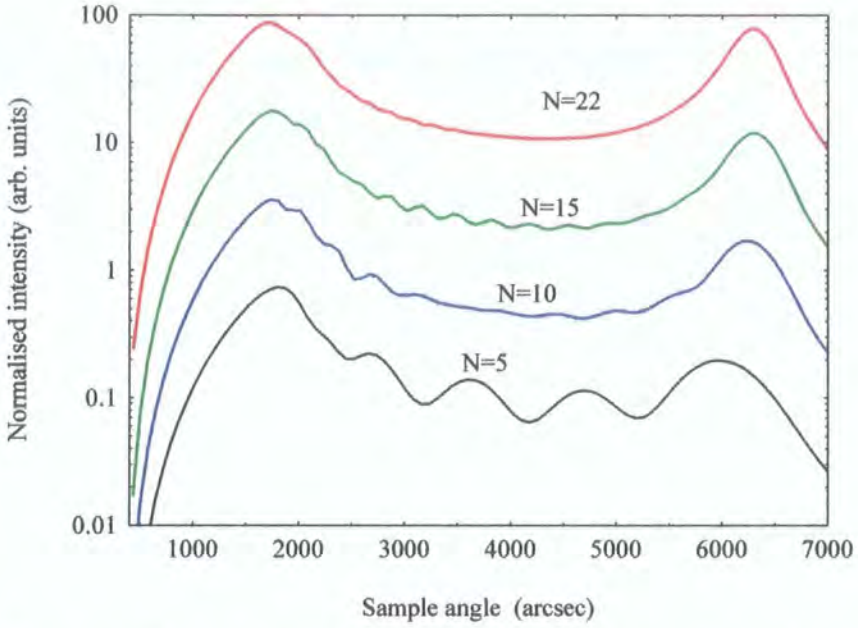


*Figure 6.11. Co/Pt Off-specular simulations with a fixed vertical correlation length of 350Å.*

A series of off-specular simulations for the nominal Co/Pt structure is shown in figure 6.11. In these simulations the vertical correlation length within the multilayer stack is set at 350Å, corresponding to the length scale suggested by the off-specular data. The loss of off-specular Kiessig fringes for a bilayer number between $N$=15 and $N$=22 is in good agreement with the trend observed in the actual experimental data shown in figure 6.7.

## 6.5 The Columnar Type Growth Model.

The next stage is to attempt to visualise, and explain the cause of, a growth mode that would lead to this loss in conformality between the top and bottom surface of a multilayer stack whilst at the same time retaining the correlation between neighbouring bilayers in the stack. One possible structural explanation for this loss of conformal growth in the stack is a columnar type growth mode in the Co/Pt system

which, as discussed in the introduction to this chapter, has been observed, through cross sectional TEM in other studies. This growth mode has been observed previously by Tatnall *et al.* [14] in which a columnar type microstructure was seen to develop with increasing bilayer number.

A representation of this type of structure is shown in figure 6.12. As the number of bilayers increases there is a noticeable change in the lateral correlation length. Over one or two bilayer repeats the effect is small but over the entire stack the effect is large. In this type of growth mode it is possible to define an out-of-plane correlation length over which the top and bottom surface become noticeably different in profile, as a consequence of the variation in correlation length, triggering the loss of the off-specular fringes.

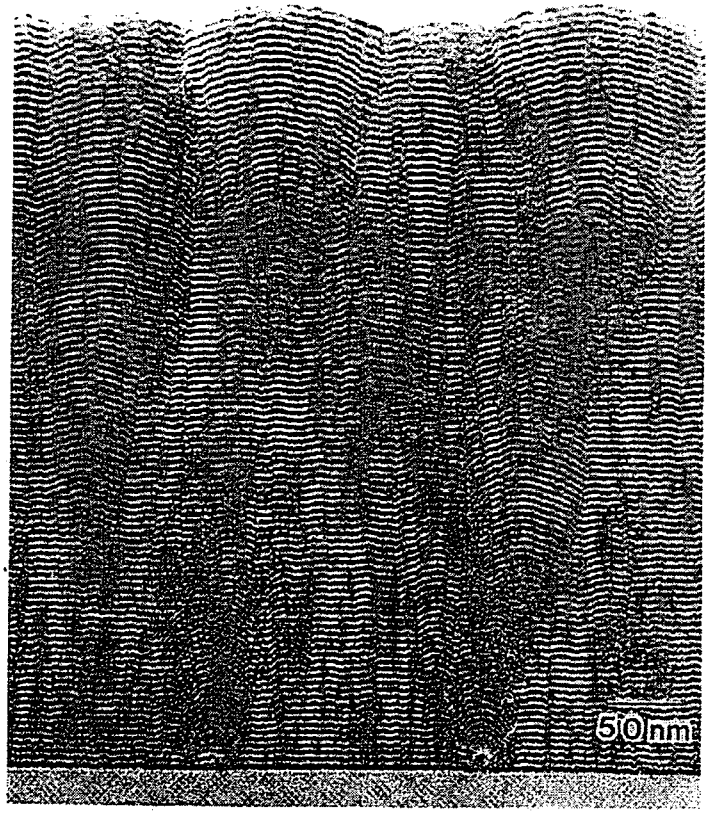


*Figure 6.12. TEM image of a columnar growth structure* [16].

The reason for the existence of this columnar type growth mode in Co/Pt and not in Co/Cu relates to the ratio of the deposition temperature to the melting point temperature ($T/T_m$) for the separate atomic species. A decrease in this $T/T_m$ ratio leads to a reduction in the surface mobility of the deposited element. The melting point for platinum is greater than that for both cobalt and copper, and therefore the ratio of $T/T_m$ is smaller. This leads to a lower surface temperature during deposition and hence a lower surface mobility for platinum. Although the sputtering yield for Pt is lower than that for Co, at similar sputtering energies, the deposition rate for Pt is almost twice that of Co, again indicating the reduced surface mobility for platinum. As a consequence of this reduced mobility a columnar type growth mode should exist in the Co/Pt but not in the Co/Cu system [5,15].

## 6.6 The Effect of Columnar Type Growth

In structures which show a high degree of columnar growth it has been observed that the convex interface structures and column boundaries can cause the pinning of domain wall motion which, in turn, can lead to an increase in the coercivity in such systems [1,2,17,19]. A more rigourous discussion of the magnetic behaviour of these sample can be found elsewhere [11] however, a clear increase in the coercivity with bilayer number has been observed in these Co/Pt samples. This increase in the coercivity is a consequence of the more pronounced grain boundaries in a columnar structure acting as pinning centres. These observations are consistent with other studies by Zeper and Greaves [1,10]. Further to this, torque magnetometry measurements performed by T. Moore at Durham [18] to study the variation of the anisotropy with bilayer number indicate a maximum in the perpendicular anisotropy in these Co/Pt multilayers for a value of approximately $N$=18. This is in good agreement with the columnar model and vertical length scale for conformal growth deduced from the off-specular measurements, suggesting that perpendicular anisotropy peaks in the Co/Pt systems at the last point at which there is good conformal growth throughout the entire multilayer stack. Other studies are in reasonable agreement with these observations, with an enhancement of the orbital moment and effective anisotropy for $10<N<14$ bilayers [14,20,21].

## 6.7 Summary and Conclusions

The highly correlated nature of the interfaces in the sputtered Co/Cu system has already been discussed in Chapter 5 although in all of the samples the multilayer thickness remained constant. Transverse diffuse measurements show that once again the interfaces in these Co/Cu samples possess a roughness which is highly correlated in nature. As the multilayer grows in size this high degree of correlated roughness at the interface and conformal growth is retained. It has been possible to conclude that there is no evidence for a limiting out-of-plane length scale for this conformal growth and that if one does exist it must be considerably greater than 300Å, the maximum stack thickness in this study. Indeed, other studies [22] have shown that sputtered Co/Cu multilayers with total stack thicknesses of the order of 500Å exhibit off-specular Kiessig fringes, indicating a high degree of conformality in the system. When the stack thickness is increased to 1000Å however, the off-specular fringes are lost and the off-specular Bragg peak is noticeably broader than that of the specular, suggesting that this stack thickness is in excess of the vertical length scale for conformal growth.

By consolidating structural and magnetic data it has also been possible to observe the cobalt layer immediately adjacent to the substrate to be magnetically 'dead'. This can most likely be attributed to mixing of the cobalt with silicon and oxygen species at the substrate interface.

The Co/Pt system exhibits a noticeably different behaviour as the bilayer number is increased. While the growth conformality between neighbouring bilayers is retained the conformality across the entire stack thickness is lost beyond a certain out-of-plane length scale. It has been possible to estimate this length scale to be of the order of 360Å, which in turn places the critical bilayer number for conformal growth at around 15. The most likely explanation for this loss of conformality across the stack is a columnar type growth mode in Co/Pt that is clearly not present in Co/Cu. The predominance of columnar growth in Co/Pt has been observed in cross sectional TEM based investigations and can be understood as a consequence of the lower surface temperature and hence lower surface mobility of Pt upon deposition when compared to Co and Cu. This growth mode can have a profound effect on the magnetic properties of the Co/Pt samples. The coercivity, measured on an Alternating Gradient Field

Magnetometer by D.E. Joyce, of the multilayers increases with bilayer number due to the pinning of domain walls at column boundaries. In turn the orbital moment and anisotropy energy peaks for a stack thickness corresponding to that defined for the limit of conformal growth. The correlation of roughness between successive layers would appear necessary in maintaining the magnetostaic coupling that gives rise to the anisotropy. This can be seen an initial linear increase in the anisotropy with bilayer number. Beyond a critical thickness it would then appear that the uncorrelated roughness component serves to destabilise the perpendicular anisotropy, possibly due to some form of magneto-static interaction This has important consequences for magnetic recording media, in which perpendicular anisotropy is favoured, as the degree of perpendicular anisotropy in the Co/Pt system decreases rapidly when the stack thickness exceeds this critical thickness for conformal growth.

The sensitivity of x-ray reflectivity techniques to both the in-plane and out-of-plane structural correlation of the buried interfaces within a multilayer is also clear from this work. Such measurements reveal much of the detail that could be obtained from time consuming and destructive high resolution TEM measurements with the added benefit of globally averaging over much larger length scales.

# References for Chapter 6

1.W.B.Zeper, H.W. van Kesteren, B.A.J.Jacobs, J.H.M.Spruit. J. Appl. Phys 70 (1991) p2264

2. S.Hashimoto, Y.Ochiai, K.Aso. J.Appl. Phys 66 (10), p4909 (1989)

3. C.J.Chien, R.F.C.Farrow, C.H.Lee, C.J.Lin, E.E.Marinero. J.Magn. Magn. Mater 93, p47-52 (1991) p47-52

4. P.F.Garcia, A.D.Meinhaldt, A.Suna, Appl. Phys Lett, 47, 178 (1985)

5. S.J.Greaves, A.K.Petford-Long, Y-H.Kim, R.J.Pollard, P.J.Grundy, J.P.Jakubovics. J. Magn. Magn. Mater. 113, 63 (1992)

6. W.B.Zeper, F.J.A.M. Greidanus, P.F.Garcia, C.R.Fincher. J. Appl. Phys. 65, 4791 (1989)

7. R.Atkinson, S.J.Greaves,, P.J.Grundy, R.J.Pollard, I.W.Salter. J. Magn. Soc. Japan 17, 60 (1993)

8. S.Hashimoto, Y.Ochiai. J. Magn. Magn. Mater. 88, p211 (1990)

9.S.Honda, N.Morit, M.Nawate, T.Kusuda. J. Magn. Soc. Jpn 15, 45 (1991)

10. S.J.Greaves, P.J.Grundy, R.J.Pollard, J. Magn. Magn. Mater. 121, p532 (1993)

11. D.E. Joyce, Ph.D Thesis, University of Salford, (1998)

12. M.Safa, B.K.Tanner. J. Magn. Magn. Mater. 150, L 290, (1995)

13. C.Zhou, D.M.Newns. Superlattices and Microstructures. Vol 23. No. 3 p 539 (1998)

14. C.J.Tatnall, D.E.Joyce, P.J.Grundy, J-P. Schille, G. van der Laan. J. Magn. Magn. Mater. 177-181, p1181 (1998)

15 J.A.Thornton. Ann. Rev .Mater. Sci 7, p239 (1977)

16. Fractal Concepts in Surface Growth. A.L.Barabassi, H.E.Stanley. Cambridge Press. (1995)

17. M.Kitada, N. Shimizu. J. Appl. Phys 54 (12) p7089

18. Thomas Moore, M.Sci project. University of Durham (1997)

19. S.Honda, H. Tanimoto, J.Ago, M.Namate, T. Kusuda. J. Appl. Phys. 70, p6047 (1991)

20. G.H.O.Daalderop, P.J.Kelly, F.J.A. den Broeder. Phys. Rev. Lett. 68, p6822 (1992)

21. D.Weller, Y.Wu, J.Stohr, M.G.Samant, B.D.Hermsmeier, C.Chappert. Phys. Rev. B 49.p 1288 (1994)

22. T.P.A.Hase, Ph.D Thesis, University of Durham (1998)

# Chapter 7

# The Fe/Au Multilayer System

## 7.1 Introduction

This chapter relates to the comparison of (100) and (111) oriented Fe/Au multilayers grown, by Molecular Beam Epitaxy (MBE), on (001) MgO and $(1\bar{1}20)$ sapphire substrates respectively. An extensive structural study will be presented to explain the remarkable differences observed in both the GMR and saturation conductivity between the two orientations. Grazing Incidence Reflectivity measurements have been performed in order to study the interface morphology and conformality within these multilayers, with High Angle Double Axis (HXRD) and Grazing Incidence Diffraction (GIXD) giving an insight into the out-of-plane and in-plane crystallographic orientation, layer quality and defect density. Through this work it is possible to describe the observed differences in the GMR and conductivity by an electron channeling model, present only in the (100) oriented system, resulting from differences in the spin asymmetry in the reflection coefficients for this orientation. Such an asymmetry, and subsequent electron channeling effect, has been predicted theoretically but has, until now, never been observed experimentally.

Discussion then proceeds, via Grazing Incidence Fluorescence (GIXF) measurements, to the apparent mobility of the Nb buffer material within the multilayer in the system grown on sapphire. Finally, the defect model proposed by Holý *et al.* [1], enabling mosaic defects and roughness effects to be distinguished, is examined in relation to the Fe/Au (100) system.

## 7.2 The Samples

Although in recent years there have been many studies of systems comprising of single or multilayered Fe and Au, there is little in the literature with regard to the specific electron transport properties. This may be due to the assumption that, in order

to grow a high quality multilayer structure it is necessary to deposit the multilayer onto a thick Au buffer. For current-in-plane (CIP) measurements, this thick buffer acts as a low resistance shunt, thereby allowing the majority of the current to bypass the multilayer. A maximum low temperature GMR of 2.3% was observed in a study by Shintaku *et al.* [2] in (100) multilayers grown on a 470Å Au buffer. In several notable studies the Au buffer layer was of the order of thousands of angstroms [3-5]. The magneto-transport and saturation conductivity measurements presented here relate to (100) and (111) oriented multilayers grown on a 60Å Au buffer layer. This buffer thickness was found to give a respectable GMR while still retaining good structural definition in the multilayer, although a possible increase in the interface roughness was expected as a consequence of the thinner buffer layer.

The multilayers were grown by MBE by Dr P.A. Ryan and Mr D.T. Dekadjevi at the University of Leeds in the form of wedges of increasing Au thickness. A wedge type growth method allows all other layer thicknesses to be kept constant across the series of samples.

The (100) oriented (type A) samples were grown on polished MgO (100) with a nominal structure:

$$\text{MgO (100) / 10Å Fe / 60Å Au / \{ 10Å Fe / } X\text{Å Au \}*20} \quad \text{with } 0\text{Å} < X < 60\text{Å}$$

It is possible to achieve excellent epitaxial growth in this system due to the very small lattice mismatch, only 0.6%, between Au (110) and Fe (100) with good growth being achieved with a rotation of the Au lattice through 45°. Other studies have shown that Fe deposits layer by layer on Au (100) with no observable island growth [6]. The multilayer was deposited at 70 °C at a rate of 0.2 $Å s^{-1}$ for all layers. Reflection High Energy Electron Diffraction (RHEED) measurements from the top surface of the multilayer, performed at the University of Leeds, show sharp streaks, indicating good quality epitaxial layers.

The (111) oriented (type B) samples were grown on sapphire $(11\bar{2}0)$ using a growth procedure developed by J. Xu at Leeds. Xu had also postulated that the Fe

would grow f.c.c on Au (111) for the first three monolayers before switching to b.c.c growth [7]. Fe has been reported to grow epitaxially in the (110) orientation on Au (111) [8]. The samples were grown with nominal structure:

sapphire/ 30Å Nb / 60Å Au / { 10Å Fe / *X*Å Au }*20 again with 0Å<*X*<60Å

with a 30Å Nb (110) seed layer prior to the 60Å Au buffer. RHEED measurements confirmed the Au layer to be (111) oriented.

The Grazing Incidence Diffraction measurements presented in section 7.5.3. relate to type C (100) and type D (111) samples, grown on MgO and sapphire, of nominal structure:

MgO / 10Å Fe / 500Å Au / { 7.2Å Fe / 10.2Å Au }*20

sapphire/ 350Å Nb / 350Å Au / { *X*Å Fe / 20Å Au}*20 with $X = 6,12,18$Å

The in-situ RHEED measurements of D.T. Dekadjevi have shown that the growth of Fe (110) in the type D samples is pseudomorphic with respect to the Au (111) layer for the first 8Å, with perfect registration between the Au and the Fe. For Fe thicknesses in excess of 8Å there is a progressive splitting of the RHEED streaks to either side of the specular streak. The specular streak itself does not split, indicating relaxation of the Fe into two differing epitaxial structures. This relaxation is discussed further in section 7.5.2 with regard to surface diffraction measurements.

## 7.3 GMR Measurements

The GMR, measured by P.A. Ryan at 4.2 K, as a function of Au spacer thickness for each orientation is shown in figure 7.1. The (100) oriented samples grown on MgO exhibit strong oscillations in the GMR as a function of Au thickness. The period of this oscillation is in good agreement with that predicted theoretically [9,10]. Magneto-Optic Kerr effect (MOKE) measurements show that this oscillation in the GMR arises due to an oscillation in the coupling between ferro and antiferromagnetic.

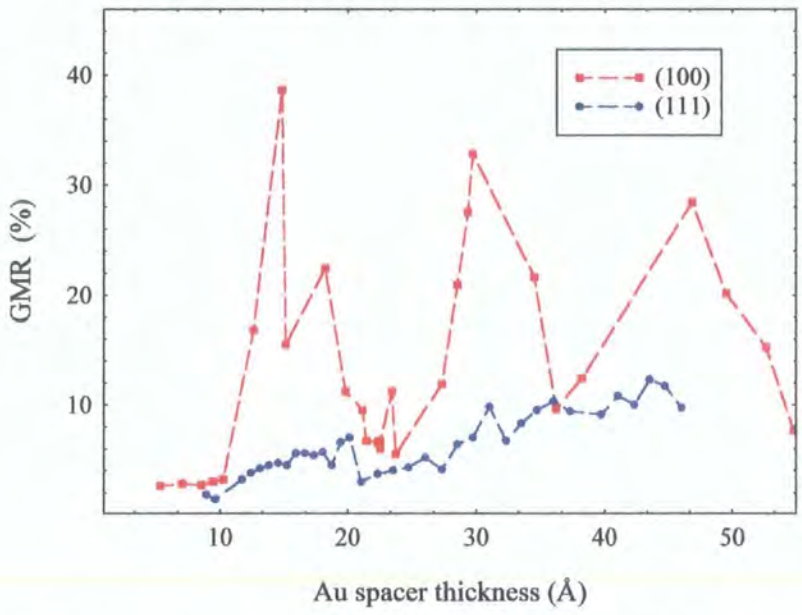


*Figure 7.1. GMR as a function of Au spacer thickness for the (100) and (111) oriented Fe/Au multilayers.*

A peak value of 38% in the GMR is achieved at the first AF coupling peak, indicating that the thin Au buffer layer still promotes a sufficiently good growth structure to observe high GMR. Shunting in the buffer layer is reduced using the thinner Au layer, the value here comparing well with the 2.3% obtained by Shintaku [2] with a 470Å buffer layer. The (111) oriented system grown on sapphire shows no oscillations in the GMR, only a slow increase with increasing Au layer thickness.

Comparison of samples with an equal AF coupled volume fraction, corresponding to a 15Å spacer and 30% remanence, gives a GMR of 38% and 6% for the (100) and (111) oriented samples respectively indicating that the difference in the GMR is indeed related to the sample orientation.

## 7.4 Saturation Conductivity

Clear differences exist in P.A. Ryan's measurements of the saturation conductivity, as a function of spacer thickness, between the two orientations, figure 7.2.

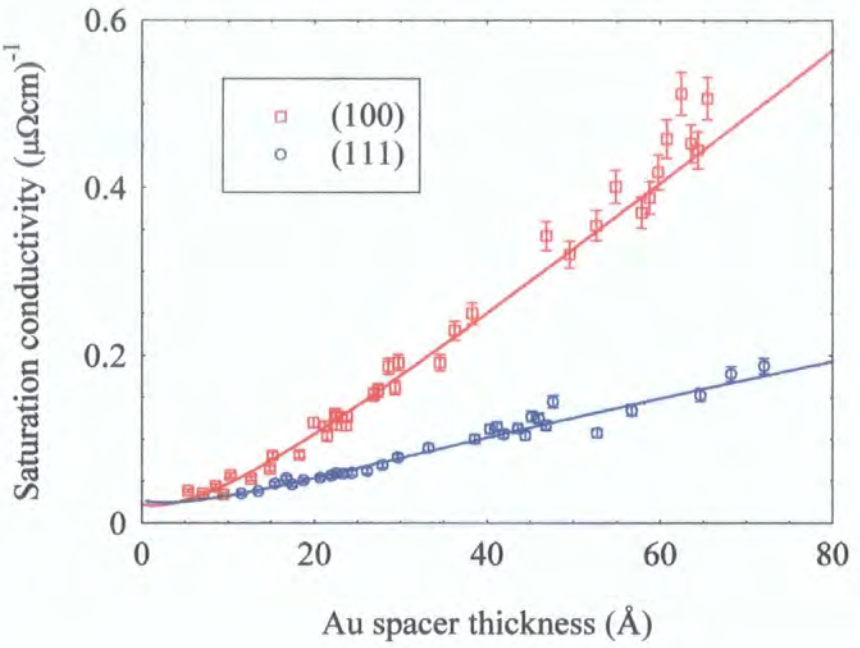


*Figure 7.2. Saturation conductivity as a function of Au spacer thickness, 4.2 K.*

The rate of increase in the saturation conductivity with increasing spacer thickness is 3 times greater in the (100) oriented multilayer. The non zero intercept for zero spacer thickness indicates the relatively small contribution of the Fe layers to the total conductivity. The solid line shows a fit to the data, modelled by P.A. Ryan, and will be discussed later with regard to the presence of an electron channeling mechanism.

## 7.5 Structural Characterisation

The distinct differences in the GMR and saturation conductivity between the two orientations could be attributed to any one of several possible differences in the multilayer structures. A larger interface roughness in the (111) oriented system would lead to an increase in the spin-independent electron scattering at the interfaces and reduction in the electron mean free path. This would result in a reduction in the conductivity and the GMR. Likewise, a larger bulk defect density in the layers of the

(111) oriented system would have the same effect. It is also possible that there may be distinct differences in the in-plane and out-of-plane layer quality and strain between the two systems. Through a combination of Grazing Incidence Reflectivity and in-plane and out-of-plane X-ray Diffraction it has been possible to address these issues.

### 7.5.1 Grazing Incidence Reflectivity

Specular and diffuse measurements and simulations were performed for (100) and (111) oriented multilayers grown with a spacer thickness of 30Å, corresponding to the second AF coupling maximum in the (100) system. Specular and off-specular scans for each orientation are shown in figure 7.3 a) and b). In both cases the off-specular scan exhibits the same periodic features as the specular scan indicating that a high proportion of the interface roughness is correlated in nature.

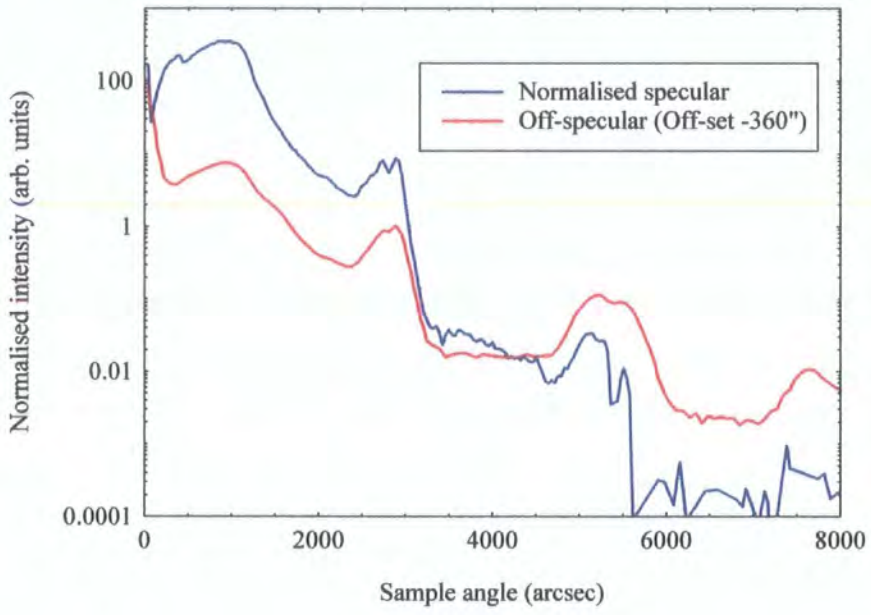


*Figure 7.3 a). Specular and off-specular scan for Fe/Au (100), λ=1Å.*

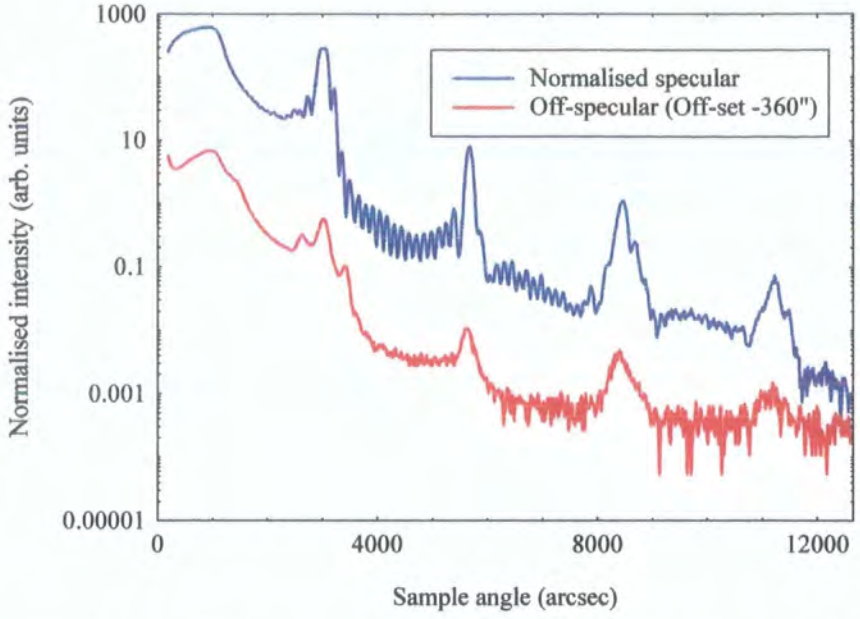


*Figure 7.3 b). Specular and off-specular scan for Fe/Au (111), λ=1Å.*

Figure 7.4 shows the excellent agreement between simulated and experimental data, which allows an accurate determination of the layer thickness and average interface width to be obtained.

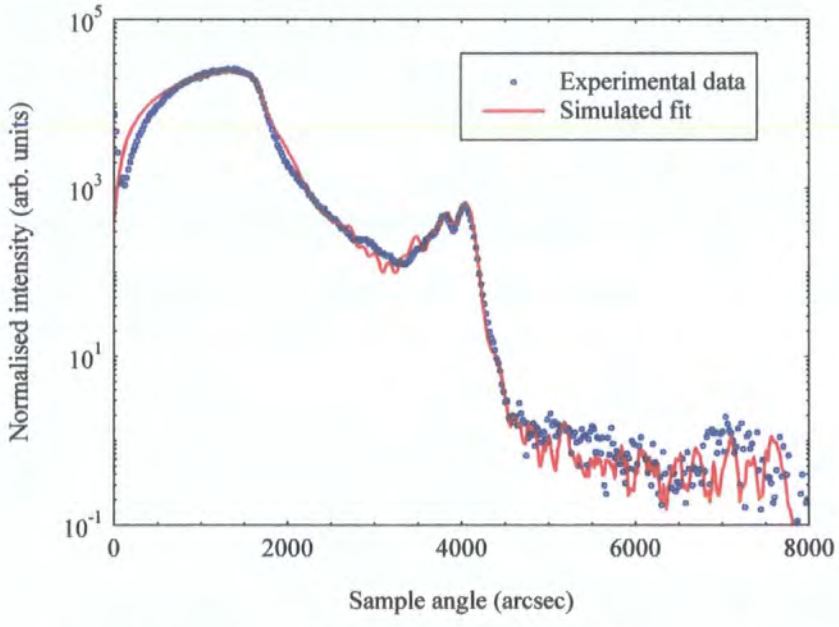


*Figure 7.4 a). Specular data and best fit simulation for Fe/Au (100) grown on MgO, λ=1.3926Å.*

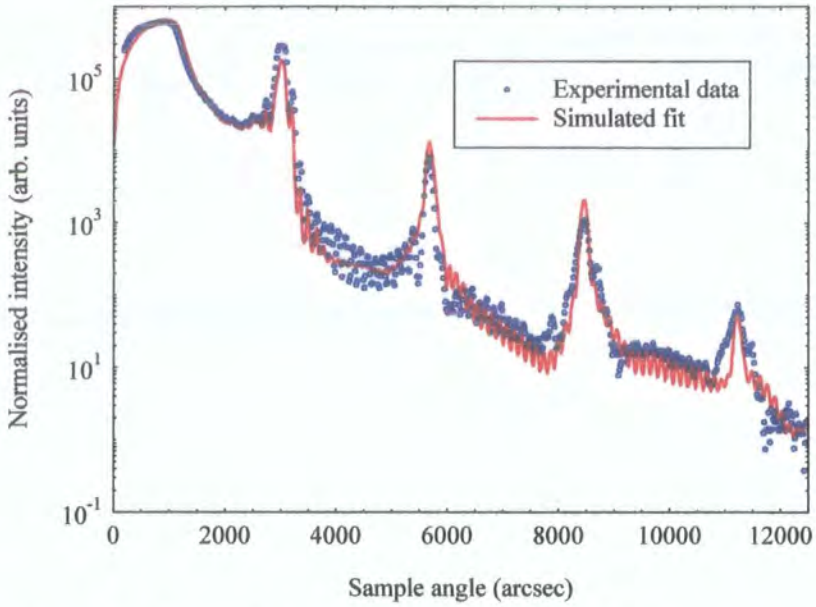


*Figure 7.4 b). Specular data and best fit simulation for Fe/Au (111) grown on sapphire, $\lambda$=1.0Å.*

The exact nature of the interface roughness and lateral interface morphology can be determined from fitting simulated data from model structures to transverse diffuse data. Typically for each sample, transverse diffuse data at several scattering vectors is modelled simultaneously. While time consuming, such a method is essential in locating the true global minimum for the simulation [11]. A series of best fit simulations are shown in figures 7.5 and 7.6.

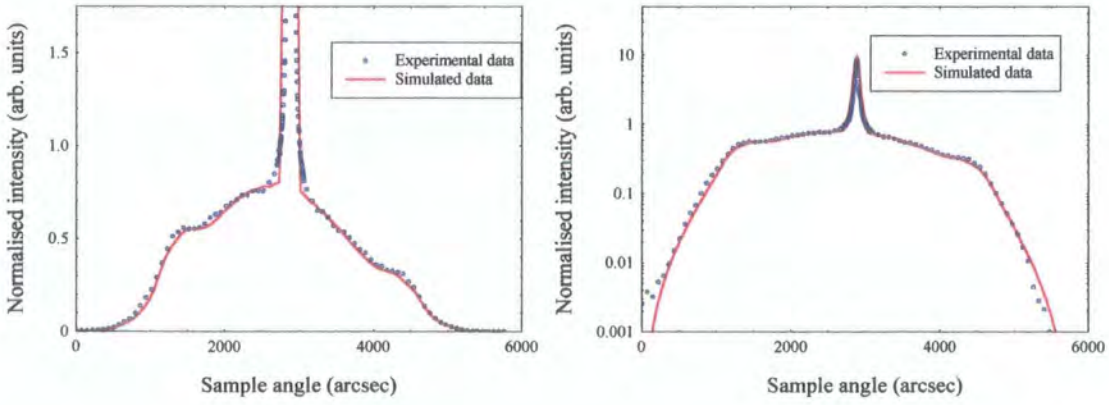

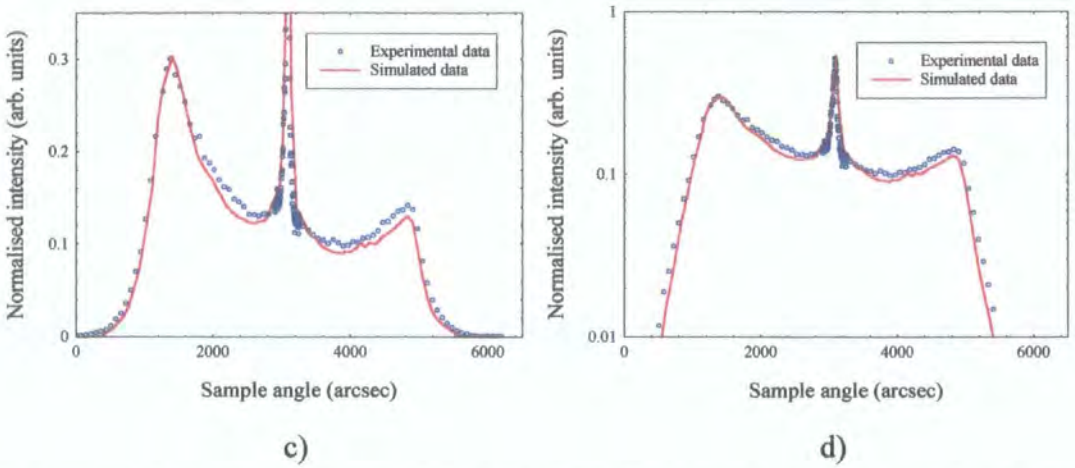


*Figure 7.5. Fe/Au (100) grown on MgO. a) diffuse scan through Bragg peak, b) log scale, c) diffuse scan away from Bragg peak, d) log scale, λ=1Å.*

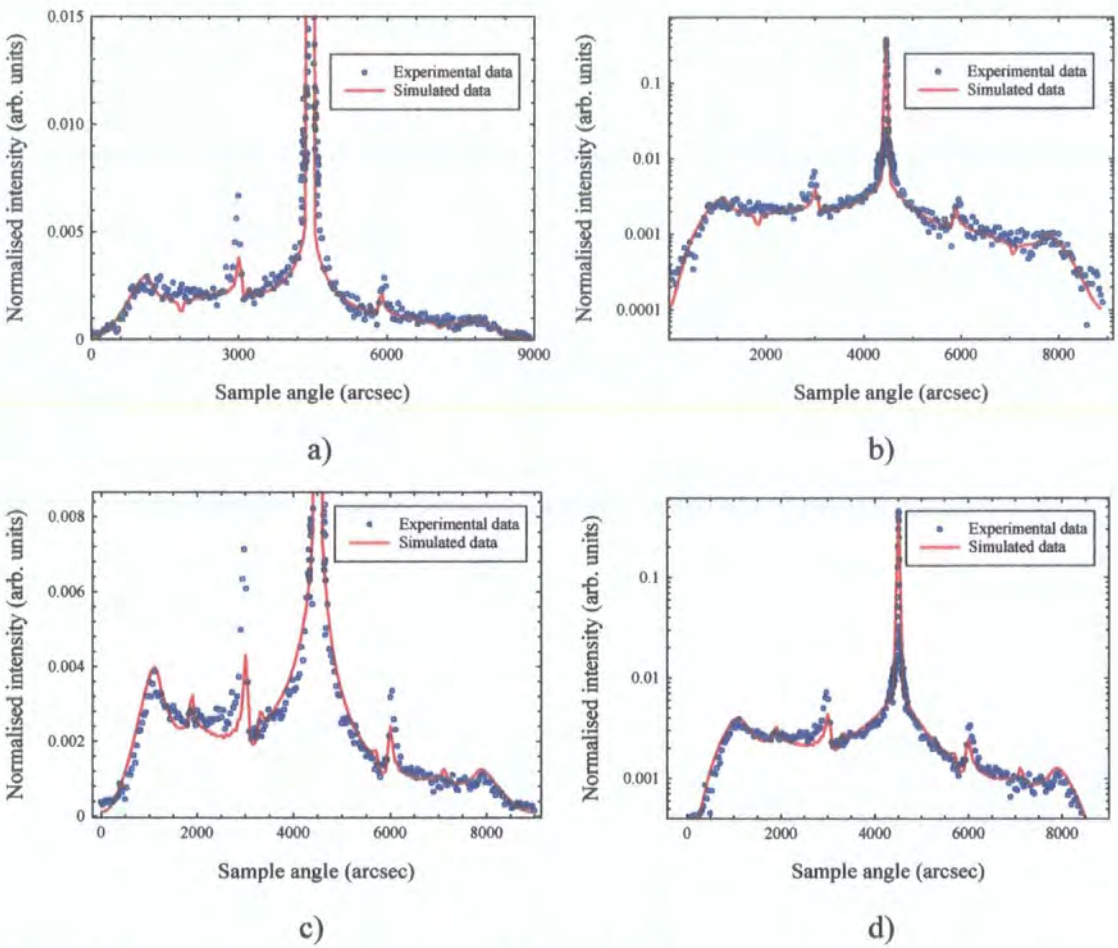


*Figure 7.6. Fe/Au (111) grown on sapphire. a) Diffuse scan through Kiessig maximum, b) log scale, c) diffuse scan through Kiessig minimum, d) log scale, λ=1Å.*

Excellent agreement was achieved between the experimental and simulated data, especially given the constraint of fitting several different scattering vectors with one parameter set. The sharp peaks between the Yoneda wing and specular ridge in figure 7.6 arise from multiple scattering corresponding to higher order Bragg reflections that are observable due to the scattering vectors, corresponding to the Kiessig maximum and minimum, being larger than that of the primary Bragg peak. Such peaks are not visible in the diffuse scan of figure 7.5 c), taken at a lower scattering vector than the Bragg peak. Multilayer interface structure and layer thickness parameters determined from these measurements are summarised in table 7.1:

| Fe/Au | Fe thickness (Å) | Au thickness (Å) | Correlated roughness (Å) | Uncorrelated roughness (Å) | Correlation length, $\xi$ (Å) | Fractal parameter, $h$ |
|---|---|---|---|---|---|---|
| (100) | 7.8±0.3 | 31.0±0.5 | 9.3±0.3 | 0.9±0.1 | 250±10 | 0.28±0.02 |
| (111) | 8.0±0.3 | 29.0±0.3 | 3.3±0.3 | 0.2±0.1 | 250±10 | 0.20±0.02 |

*Table 7.1. Multilayer structure parameters determined from x-ray scattering simulation.*

In both systems the Au spacer thickness matches the intended growth thickness to within 0.5Å, corresponding to the second AF coupling peak observed in the GMR oscillation. Differences in the GMR cannot, therefore be attributed to differences in the AF coupling fraction between the two systems. Within error limits, determined from the observed change in the accuracy of the simulation with small variations to the respective fit parameter, the bilayer thickness is the same for each orientation. The respective buffer and seed layers were also found to match the nominal thickness. There is also no significant difference in the lateral correlation length and fractal parameter between the two orientations. As indicated in the off-specular data, the interfaces in both systems possess a roughness which is predominantly correlated in nature with a correlated to uncorrelated ratio of 10:1 and 15:1 in the (100) and (111) oriented multilayers respectively. There was no observable compositional grading in either the (100) or (111) oriented system. The important point to note is that the roughness in the (100) oriented system is a factor of 3 greater than in the (111) orientation. Thus, the

differences in the GMR and saturation conductivity can not be explained by differences in the magnitude of the interface roughness and associated spin-independent electron scattering as it is the system possessing the rougher interfaces that exhibits the larger GMR and conductivity.

In order to determine whether there was an increase in the average interface roughness as a consequence of depositing on thin Au buffer layers, reflectivity measurements were performed on Fe/Au multilayers of both orientation in which the buffer layer was 200Å. The associated transverse diffuse data and simulations are shown in figures 7.7 and 7.8.

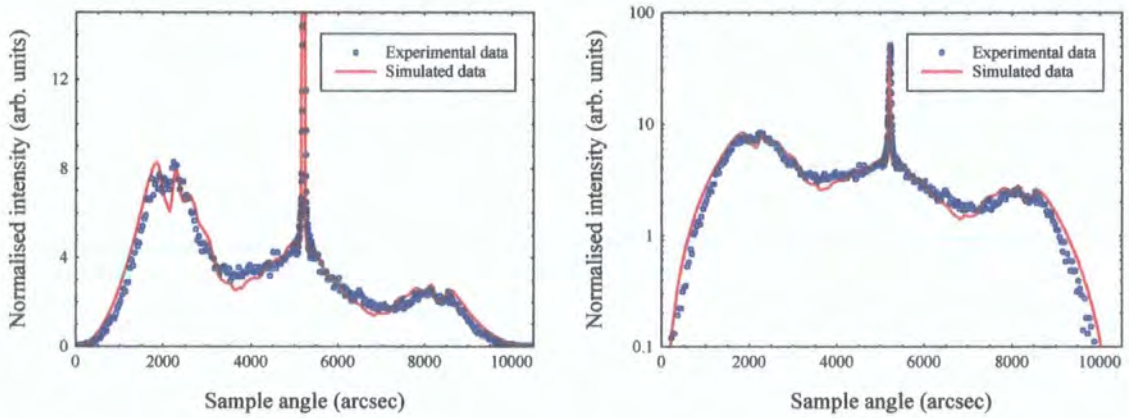


*Figure 7.7. Fe/Au (100) grown on MgO, thick buffer, a) diffuse scan through Kiessig minimum, b) log scale, λ= 1.7435Å.*

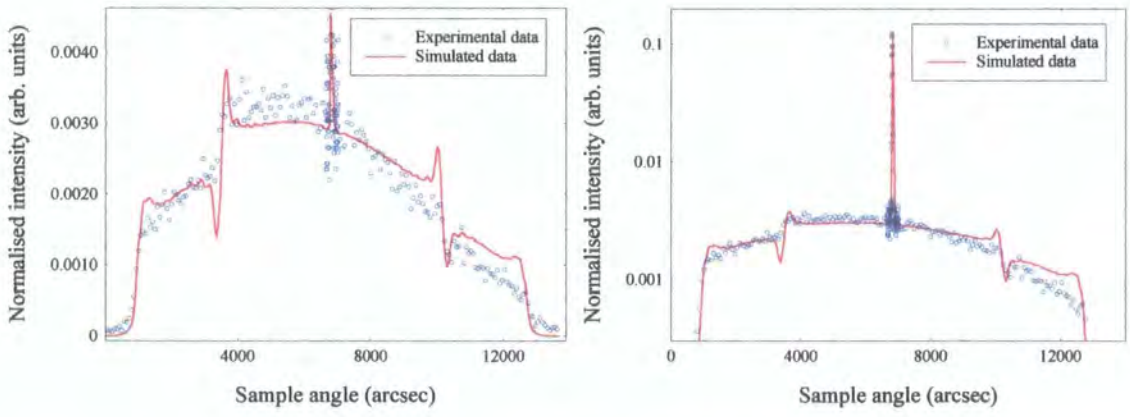


*Figure 7.8. Fe/Au (111) grown on sapphire, thick buffer, a) diffuse scan through Kiessig minimum, b) log scale, λ= 0.8 Å.*

The structural parameters for these multilayers are summarised in table 7.2.

| Fe/Au | Fe thickness (Å) | Au thickness (Å) | Correlated roughness (Å) | Uncorrelated roughness (Å) | Correlation length $\xi$(Å) | Fractal parameter, $h$ |
|---|---|---|---|---|---|---|
| (100) | 6.2±0.3 | 9.2±0.5 | 4.8±0.3 | 0.4±0.1 | 200±10 | 0.25±0.02 |
| (111) | 14.4±0.3 | 10.4±0.3 | 2.5±0.3 | 0.3±0.1 | 195±10 | 0.22±0.02 |

*Table 7.2. Multilayer structure parameters determined from x-ray scattering simulation for (100) and (111) Fe/Au grown on 200Å Au buffer.*

The average interface roughness was found to be generally slightly lower for the multilayers grown on thicker buffers. However, it is also worth noting that the roughness follows the same trend as in the type A and B samples with a higher average roughness in the (100) oriented system which is predominantly correlated in nature, with a correlated to uncorrelated ratio of 12:1 and 8:1 in the (100) and (111) oriented systems respectively. There is no evidence of any compositional grading and the lateral correlation length and fractal parameter are comparable for each orientation.

From these measurements, we see that the observed differences in the GMR and saturation conductivity cannot be explained by the differences in the interface roughness and morphology as in all cases the interface roughness is smallest for the (111) multilayers grown on sapphire.

### 7.5.2 High Angle X-ray Diffraction (HXRD)

As the differences in the magneto-transport behaviour between the two systems do not originate from differences in the magnitude of the interface roughness and associated scattering, the next stage is to consider possible differences in the bulk scattering between the two orientations. High Resolution Double Axis Diffraction measurements provide a method by which to study the out-of-plane layer structure with regard to crystalline orientation, layer perfection and strain.

High Angle, coupled θ/2θ, Diffraction scans running longitudinally down the reciprocal lattice vector for the (100) and (111) oriented samples with a nominal Au spacer thickness of 30Å, the same samples used in the reflectivity measurements, are shown in figure 7.9.

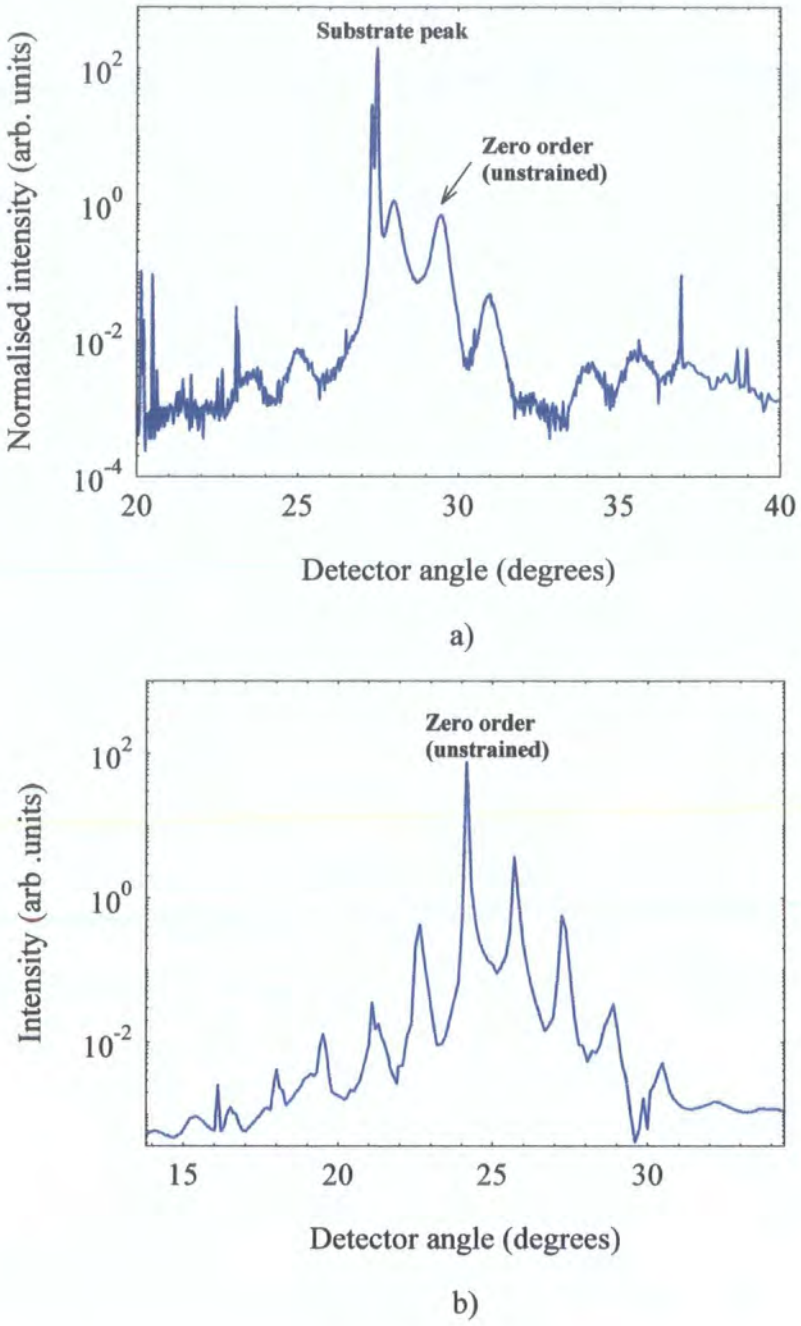


*Figure 7.9. High resolution double axis diffraction scans for a) Fe/Au (200) and b) Fe/Au (111) reflections, λ=1Å.*

In both systems there is a well defined zero order multilayer peak with several satellite diffraction orders, equally spaced about the this zero order peak. The scattering is dominated by the Au layers and is largely insensitive to imperfections within the Fe layers. The peak positions are within 0.3% agreement of those calculated from the bulk lattice parameters, weighted by relative layer thickness, in both systems. This confirms the Au in the multilayers to be (100) and (111) oriented for the MgO and sapphire substrates respectively, with no other orientations present and minimal out-of-plane strain. The sharp, well defined peaks, visible out to high order, indicate the interfaces to be crystallographically abrupt with well defined, epitaxial layers and little interdiffusion. This is illustrated in the diffraction scan shown in figure 7.10 where prolonged exposure to the focused beam caused a significant degree of interdiffusion within the multilayer. The integrated intensity under the peak, normalised to that of the main diffraction maximum, is shown above each peak and it is clear that in the damaged sample the integrated intensity does indeed diminish with increasing satellite order due to the loss of abrupt interfaces.

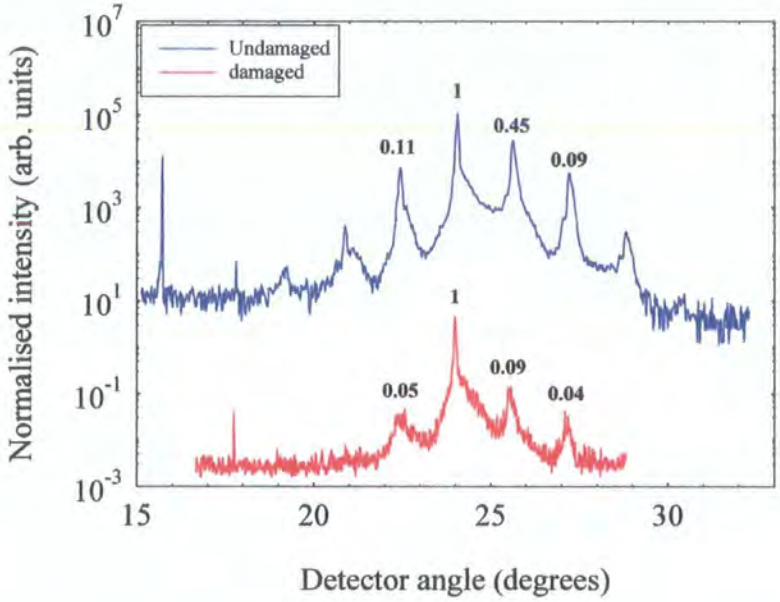


*Figure 7.10 High angle diffraction scans, off-set for clarity, for a type B sample before (blue line) and after (red line) prolonged exposure to, and subsequent damage by, the focused beam at XMaS.*

The effect of interdiffusion on the satellite intensity can be understood from considering the Fourier transform of the structural periodicity. For a non-interdiffused structure of period $d$, the Fourier transform yields a series of delta functions, separated by a distance $d$. If interdiffusion then causes a change in the structural periodicity, say $d + \Delta d$, then the delta functions of the Fourier transform reduce in intensity and broaden.

Scherrer analysis [12] based on the full width at half height maximum (FWHM) of the zero order peak in the coupled $\theta/2\theta$ scan gives a measure of the out-of-plane sub-grain size to be 145±10Å and 590±30Å, compared to a total stack thickness of 740Å, in the (100) and (111) systems respectively. Lateral grain sizes, determined from the FWHM of the high angle rocking curves fitted to the Lorentzian squared function introduced by Gibaud *et al.* [13] were found to be 165±10Å and 540±30Å, showing that the sub-grains in each system are equiaxial in nature (figure 7.11). Similar measurements on other Fe/Au systems with differing layer and buffer thicknesses also reveal sub-grain dimensions of the same order.

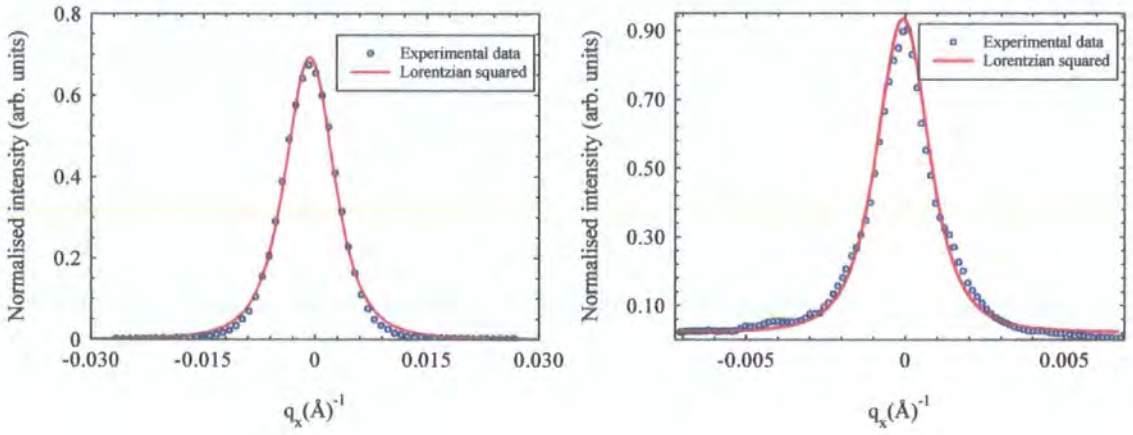


*Figure 7.11a). Transverse diffuse scan (rocking curve) through the zero order multilayer peak for Fe/Au (100) a) and (111) b) with Lorentzian squared fit.*

The High Angle measurements show that the layers are of high epitaxial quality for both orientations with minimal strain and sharp interfaces. However, there is a notable difference in the sub-grain size between the (100) and (111) oriented multilayers. The (100) oriented multilayer consists of sub-grains of average dimension four times smaller than those in the (111) multilayer. This means that the defect density

and, in turn, the number of sub-grain boundaries in the (100) oriented multilayer will be considerably larger. At low temperatures, defect scattering is dominated by scattering at these boundaries [14-17], which subsequently determines the mean free path of electrons within the multilayer. Yet it is this system, with the lowest mean free path, that exhibits the higher GMR and saturation conductivity. Again the explanation for the differences in the magneto-transport between the two orientations of Fe/Au can not originate in differences in the layer quality, indicating some type of novel conducting mechanism, specific to the (100) oriented multilayers which is leading to an enhanced conductivity, despite the larger defect scattering density.

### 7.5.3 Grazing Incidence Surface Diffraction (GIXD)

In order to study the in-plane structure and disorder within (100) and (111) oriented, type C and D, multilayers, Grazing Incidence Surface Diffraction measurements were performed, on the recently commissioned XMaS beamline at the ESRF. A grazing angle of 0.2° was selected, below the critical angle for total external reflection, limiting the depth penetration of the evanescent wave to approximately 50Å.

A sample rotation scan, in which the detector was fixed at the position of the Au (022) reflection and the sample rotated in the plane of the film, is shown in figure 7.12.

Well defined 4- and 6- fold symmetries indicate the Au layer to be deposited as epitaxial single crystals of (100) and (111) orientation in the MgO and sapphire systems. The sharp, high intensity peaks indicate little in-plane crystalline disorder, the mosaic spread being approximately 0.5° and 3° in the (100) and (111) systems respectively.

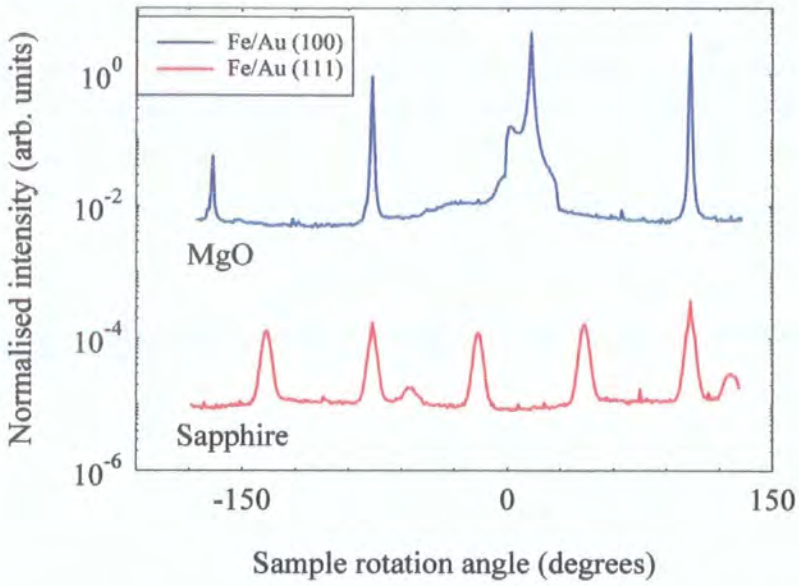


*Figure 7.12 Sample rotation scan at the Au (022) reflection position for Fe/Au on MgO and sapphire, λ=1.033Å.*

In contrast, the Fe layers, are of very poor crystalline quality in both systems, as illustrated in figure 7.13.

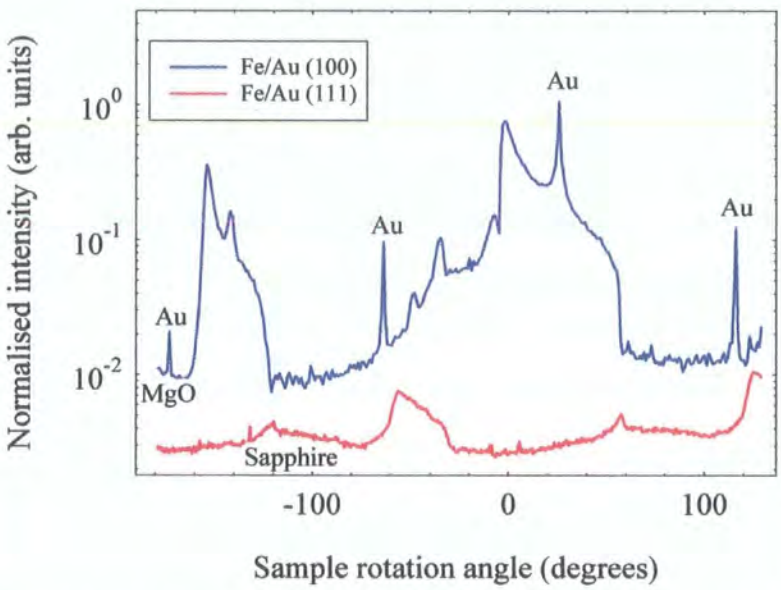


*Figure 7.13. Sample rotation scan at the Fe (022) reflection position for Fe/Au on MgO and sapphire, λ=1.033Å.*

The sharp peaks observed in the scan of the MgO substrate sample arise due to overlapping Au reflections at this particular diffraction condition. The peak symmetry is consistent with (110) oriented Fe, as seen in the RHEED data. Alignment of the Fe

(100) direction with the Au (110) direction was observed in the sapphire based system, the small peaks in figure 7.12 at approximately -55° and 125°, corresponding to this lattice condition. The lattice matching is also indicated in the coupled detector/sample scan in figure 7.14 in which the underlying Fe (100) reflection is responsible for the shoulder on the right of the Au (220) peak.

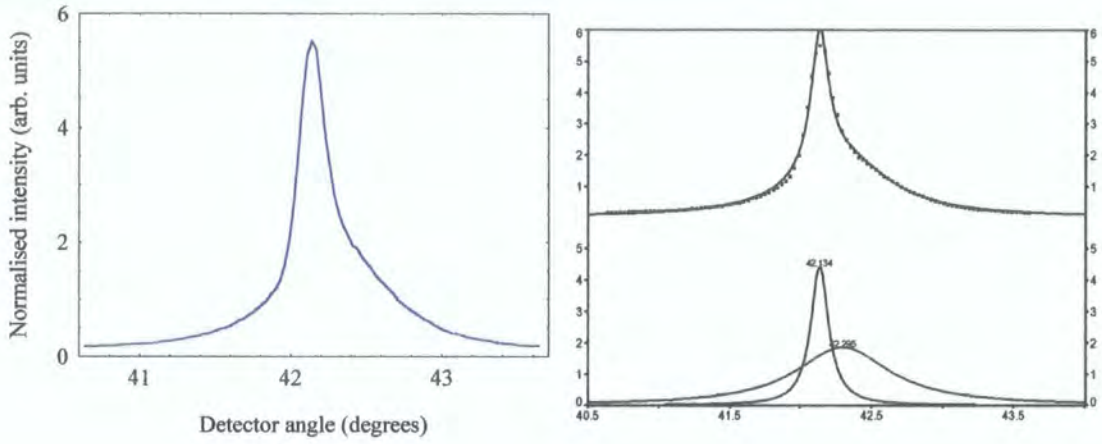


*Figure 7.14. Coupled detector / sample rotation scan taken at the Au (220) reflection position. The asymmetry in the peak is due to the underlying Fe (100) reflection, $\lambda$=1.033Å.*

The in-plane lattice parameters, determined from the peak position in coupled detector/sample scans of the type shown in figure 7.15, were found to be 4.06 ± 0.01Å and 2.86±0.01Å for Au and Fe respectively in both sample types.

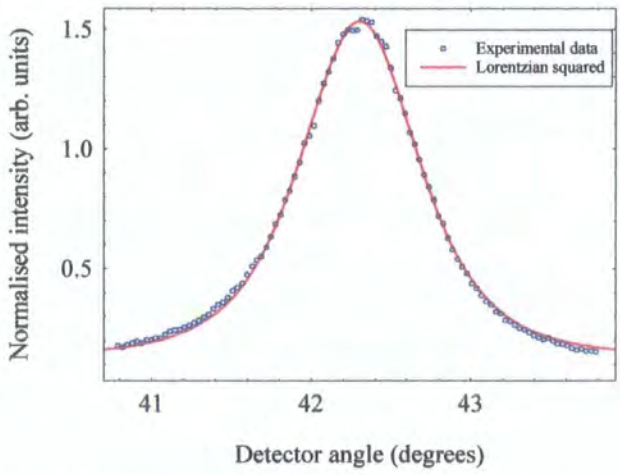


*Figure 7.15. Coupled detector / sample scan at the Au (220) reflection used to determine lattice parameter, $\lambda$=1.033Å.*

The excellent agreement between these values and standard bulk values indicates that there is very little in-plane strain in either the (100) or (111) oriented system. From analysis of allowed reflections, a mixture of both f.c.c and b.c.c Fe was observed in the Fe/Au (111) multilayers, see figure 7.16, consistent with the growth model proposed by Xu *et al.* [7] discussed earlier.

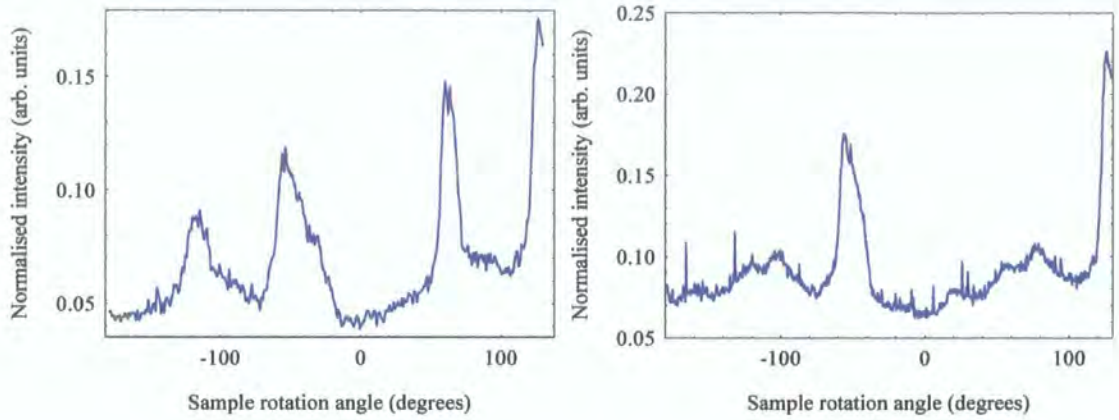


*Figure 7.16. Sample rotation scan at the a) Fe (113) f.c.c only and b) Fe (112) b.c.c only reflection positions, $\lambda$=1.033Å*

The relaxation of the Fe layer into two different epitaxial structures, observed in the RHEED data discussed earlier, was studied, by D.T.Dekadjevi at Leeds, by measuring the lattice spacing along different azimuthal angles. Such measurements [18] indicate that the Fe deposits initially in a domain of strained f.c.c material, pseudomorphic to the Au. The Fe then partially relaxes into two differing b.c.c epitaxial structures with a surface consisting of two rectangular surface nets with differing centres. A surface diffraction scan taken for a detector angle of 25.7° is shown in figure 7.17. The well defined 6- fold symmetry of the Fe (110) is clear and is consistent with one of the lattice spacings of 2.36Å measured from the RHEED analysis. When the Au (022) scan is overlayed the Fe plane is found to be rotated by approximately 22° with respect to the underlying Au, consistent with the strained rectangular net. For sample rotation angles of approximately -55° and 125° the strained Fe (110) peaks are seen to be indexed to the partially strained Fe (200) peaks present in the Au (022) scan.

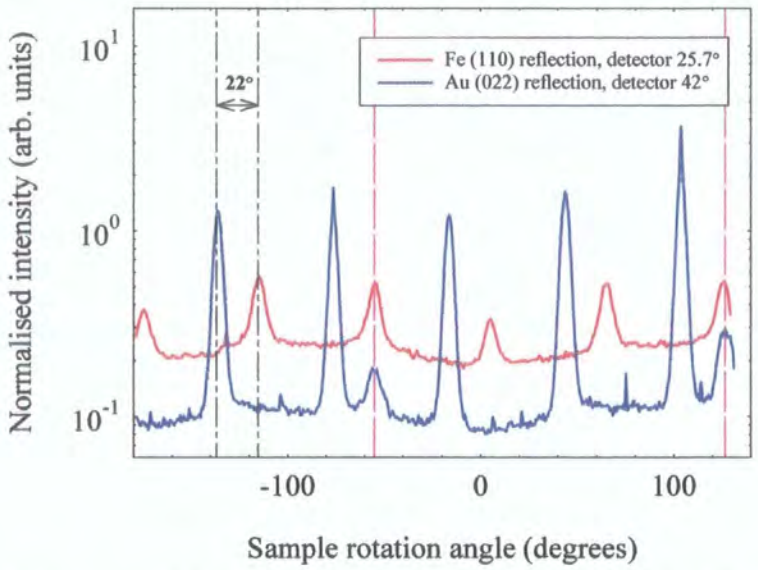


*Figure 7.17. GIXD scan taken at the Fe (110), red, and Au (022) reflection, blue, for Fe/Au (111) grown on sapphire, Fe thickness =18Å, λ =1.033Å.*

The surface diffraction scan taken at the Fe (110) reflection for a sample in which the Fe layers are only 6Å thick, figure 7.18, exhibits no well defined symmetry, in contrast to the sample with the thicker Fe layer, as the Fe is still in a strained pseudomorphic phase with respect to the Au at this thickness.

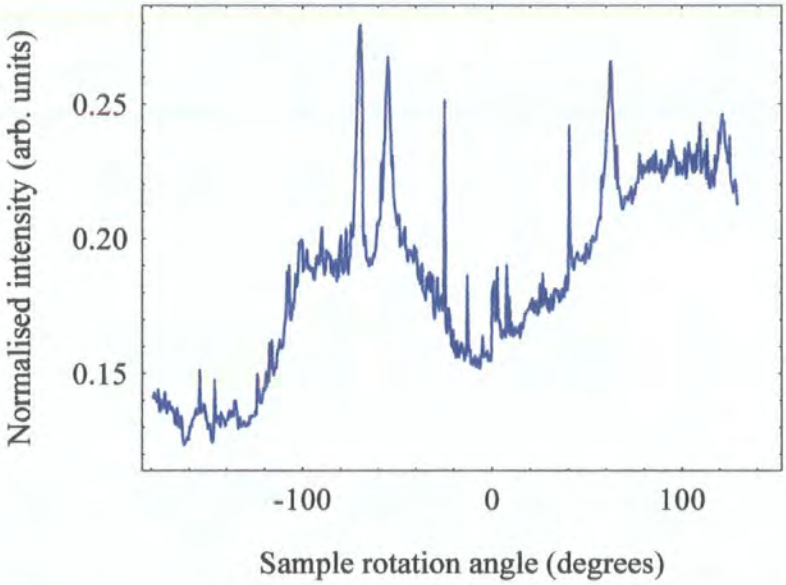


*Figure 7.18. GIXD scan taken at the Fe (110) for Fe/Au (111) grown on sapphire, Fe thickness = 6Å, λ=1.033Å.*

In summary the GIXD data shows there to be good in-plane order and minimal strain in the Au layers of both orientations with well defined crystalline symmetries. In contrast to this the Fe layers are of poor crystalline quality in both systems, even with the thicker buffer layers used in these samples. There are no significant differences in the in-plane structural quality between the (100) and (111) oriented multilayers to which the large differences in the magneto-transport behaviour can be readily attributed.

## 7.6 Electron Channelling

The absence of any structural explanation for the differences in the magneto-transport in (100) and (111) oriented Fe/Au suggests that the differences stem from a fundamentally different conducting mechanism in the (100) system. A channelling mechanism has been proposed by Stiles *et al.* [19] which is dependent upon differences in the reflection coefficients for electrons of different spin orientation incident on a multilayer interface. Other studies [20,21] have demonstrated that specular reflection from the top surface of a spin valve structure can enhance the GMR. If, as in channelling, one of the electron spins has a high reflection probability compared to the other spin then, in the case of a saturated sample in which the magnetic moments are parallel, one spin channel has a high reflection coefficient at both interfaces and the electron is confined within the layer due to the lack of free states into which it can scatter. If the spacer layer in which the electron becomes confined has a much lower resistivity than the magnetic layer, as in the case of Fe/Au, then the spacer will act as low resistance shunt leading to an enhancement in both the saturation conductivity and the GMR. The orientational dependence of this effect is due to the fact that although the reflection probability for an electron travelling from the magnetic layer to the spacer layer in the (100) system is similar for each spin, the reflection probability for a electron moving from the spacer to the magnetic layer is five times greater for the minority electrons than for the majority carriers. The asymmetry for the (111) oriented system is much less, therefore the (100) system should be a good candidate for electron channelling whereas the (111) system should not be.

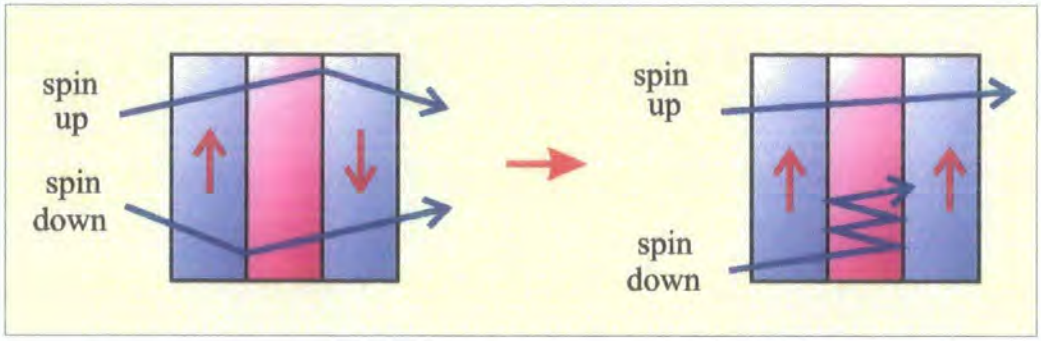


*Figure 7.19. Schematic representation of an electron channeling mode in which one spin channel is confined within the low resistance spacer layer.*

Fits to the saturation conductivity data in figure 7.2, by P.A. Ryan at the University of Leeds, also support the channeling hypothesis. The intercept on this figure 7.2 indicates the small contribution to the conductivity from the Fe layers. For this reason, differences in the disorder and poor layer quality of the Fe observed in the GIXD measurements are not crucial as only a small fraction of the current is carried in these layers. Further, variations in the Fe layer resistance will simply alter the off-set in the two conductivity plots, not the rate of increase as a function of Au thickness. It is in the explanation of the different conductivity gradients that the channeling model manifests itself.

If the conductivity data is modelled for a mean free path of comparable length to the bilayer thickness, with the layer conductivites simply added in parallel and weighted by thickness, the expression does not fit the data for either the (100) or the (111) system. This would suggest that either the mean free path is shorter than the thickness of a single layer, about 30Å, or much greater than the entire multilayer stack thickness. Alternatively the electrons may be confined in some way within one layer. The conductivity measured here is simply too large to allow a short mean free path. If the mean free path was of the order of the stack thickness then the multilayer conductivity should simply be the weighted sum, in series, of the individual layer conductivities. Again, this does not fit the data.

In the channeling mode, even though the mean free path may be large, the electron only samples relatively few bilayers due to the fact that it is confined within a single layer for large distances. If the data is then modeled using the parallel summation approach, with a Fuchs size effect term to account for boundary scattering [22] and an additional modification to the conductivity of the Au layer to include a term to measure the number of specular reflections of an electron incident on an interface, the fit shown in figure 7.3 is obtained, in excellent agreement with the measured conductivity. The simulations yield a mean free path in the Au layers of the order of 5000±2000Å, corresponding to a conductivity of the order of $5(\mu\Omega cm)^{-1}$, which is effectively scaled to three times this value in the channeling mode. A more detailed description of the simulations can be found in the thesis of P.A. Ryan [23]. The ratio of the specular reflections in the (100) and (111) system was found to be 2.7±0.1, in good agreement with the difference of approximately 3 in the rate of increase of the conductivity with spacer thickness for each orientation. This channelling mode means that the electron in the (100) system travels a considerably larger distance within the low resistance Au layer compared to the (111) system, leading to an enhancement in the conductivity and GMR even though the defect density and interface roughness are both larger for the (100) oriented multilayer.

## 7.7 Niobium as a Surfactant in Fe/Au (111) Growth

In order to determine the depth distribution of the elements in the Fe (111) system, Grazing Incidence Fluorescence (GIXF), measurements were undertaken on station 2.3, at the Daresbury SRS. GIXF measurements are sensitive to the elemental fluorescence yield from a sample, which in turn changes as a function of incident beam angle due to the variation in beam penetration depth inherent with a grazing incidence technique. It is therefore possible to produce an elemental profile of a sample as a function of depth by modelling the fluorescence yield as a function of incident beam angle. An example fluorescence profile is shown in figure 7.20.

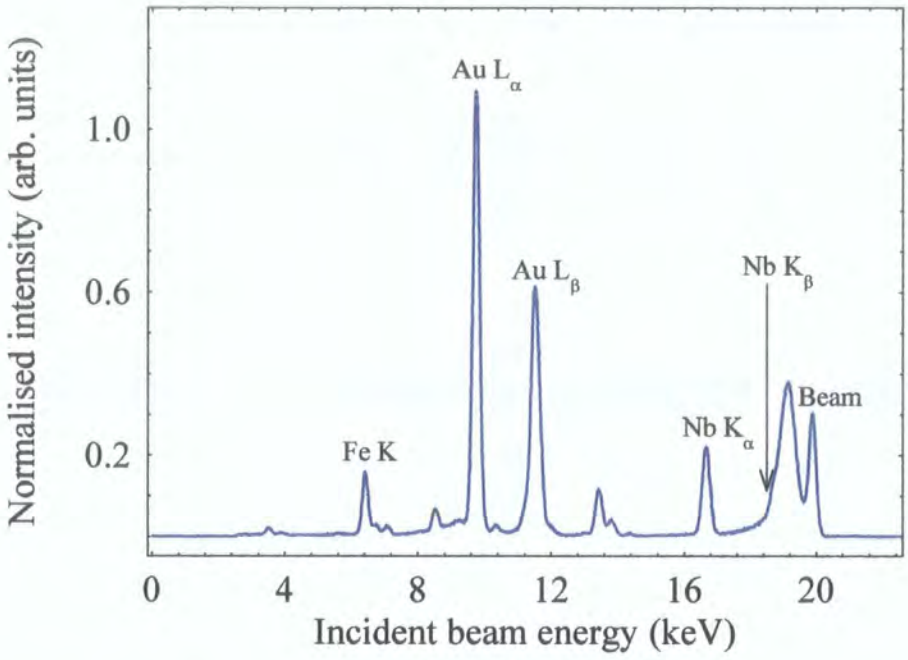


*Figure 7.20. Example Fluorescence profile with the characteristic elemental peaks marked, $\lambda = 0.63Å$.*

The Nb $K_\alpha$ and the Fe $K_\alpha$ fluorescence yields as a function of incident beam angle for a type D sample are shown in figure 7.21.

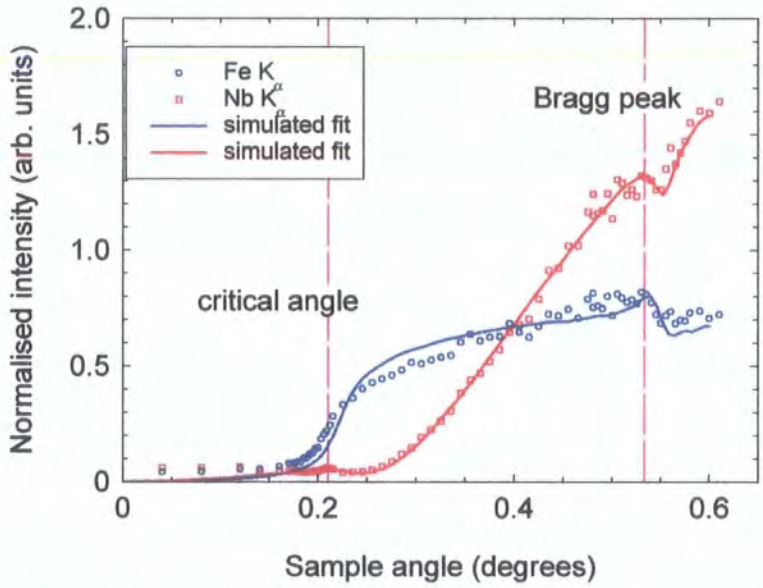


*Figure 7.21. Nb $K_\alpha$ and Fe $K_\alpha$ fluorescence yield for a type D sample with Fe thickness of 12Å, $\lambda = 0.63Å$.*

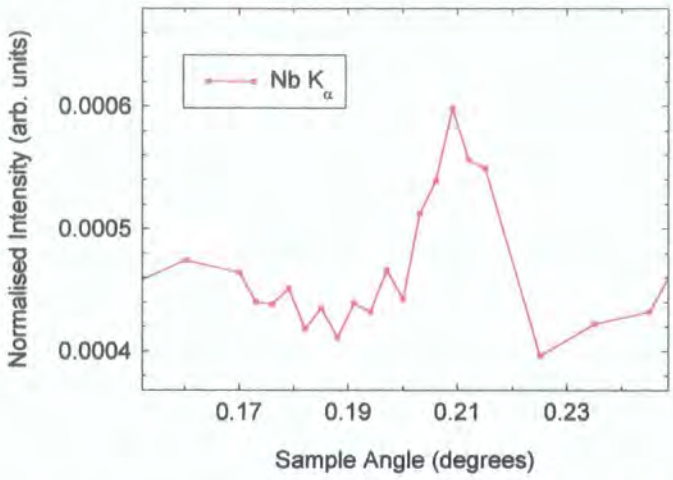


*Figure 7.22. Nb $K_\alpha$ fluorescence yield for a type D sample, with Fe thickness of 12Å, $\lambda = 0.63$Å, showing the enhancement at the critical angle.*

For incident beam angles below the critical angle the incident beam is totally externally reflected and there exists an evanescent wave which penetrates to a depth of the order of 30-50Å into the multilayer. Below this the magnitude of the electric field is negligible until the incident angle exceeds the critical angle. Prior to the critical angle there is a small Fe fluorescence yield originating from the near surface Fe layers within the depth sensitivity of this evanescent wave. What is surprising, however, is that there is also a Nb fluorescence yield in this regime, even though the Nb buffer is at a depth far in excess of the evanescent wave. Such an observation would suggest the presence of a very near surface Nb layer. Beyond the critical angle the fluorescence yield increases for the Fe and then saturates. The Nb yield increases beyond the critical angle as excitation of the buffer occurs, finally saturating at a higher level than the Fe signal due to the large quantity of Nb in the buffer. All profiles show a small modulation at the Bragg condition. The simulation of the Nb fluorescence yield, shown in figure 7.21, suggests that the Nb signal is originating from a thin surface layer of Nb of the order of 0.7Å in thickness. An enhancement in the Nb fluorescence yield occurs at the critical angle, figure 7.22, again characteristic of a surface Nb layer. Simulations in which the Nb is distributed within the bulk of the layers or at the interfaces are not in agreement with the experimental data. This would suggest that the Nb is behaving as a surfactant and is surface segregating in a thin layer. The simulated Fe $K_\alpha$ and the Au $L_\alpha$ fluorescence yields for this structure follow the same angular dependence, figure 7.23, as they share the same spatial distribution within the multilayer.

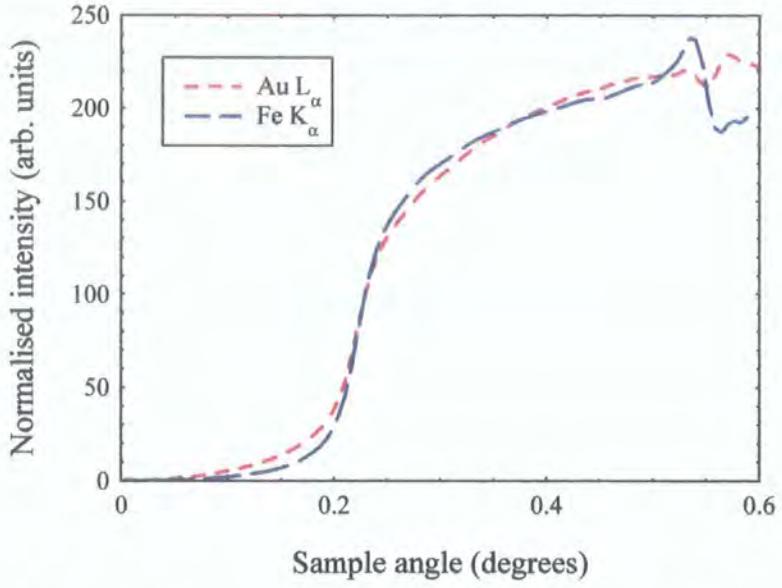


*Figure 7.23 Fe $K_\alpha$ and Au $L_\alpha$ fluorescence yield as a function of incident beam angle, $\lambda = 0.63Å$.*

An initial degree of confusion as to the apparent difference in the fluorescence yield as a function of beam angle for Nb $K_\alpha$ and Nb $L_\alpha$, with the later also following the Fe $K_\alpha$ profile, was clarified when it was found that the Nb $L_\alpha$ and Au $M_\alpha$ emission lines were overlayed and that the signal initially attributed to Nb was in fact originating from the Au.

The possible mobility of Nb within a multilayer observed here is of great importance. Sapphire substrates with Nb buffers are used as standard in the growth of a wide range of multilayer systems and yet the potential mobility of the Nb buffer material has never been documented. However, surfactant effects have been observed in other systems such as Ge/Si grown on As or Sb [24] and Co/Cu grown on Pb [25] in which the surfactant serves to smooth the interfaces and can suppress island growth. It is quite possible that the presence of Nb within the bulk of the multilayer could have a significant effect on the magneto-transport behaviour of the system. However, it is clear from the simulations that the Nb is excluded from the bulk of the Fe and Au layers and will therefore have no effect on the magneto-transport properties. The presence of Nb in the near surface regions, i.e. within the top 50Å, is indisputable from these fluorescence measurements, although the exact method of propagation the Nb through the many layers and interfaces of a multilayer film remains unclear.

## 7.8 The Defect Model for a Layered System

Interface roughness also effects the diffuse scatter around the reciprocal lattice points, the diffraction satellite width perpendicular to the $q_z$ direction depending on the roughness and not any layer thickness variation. A method of describing x-ray diffraction within thin layers and multi-layered systems, based on an optical coherence approach, was proposed by Holý *et al.* in 1993 [1]. Two specific type of defect were considered in this formalism. Firstly, volume defects, described by a mosaic defect model, in which the defects are randomly placed within the crystalline matrix of the multilayer. Secondly, interface defects were described via a roughness model. Although the mosaic structure of such systems has been extensively studied [26,27] the influence of rough interfaces, while being studied theoretically [28-30], has received little experimental treatment. It is this roughness defect model that will be examined here.

In the mosaic defect model the crystal volume is divided into an ensemble of randomly misoriented blocks. For simplicity, it is assumed the random rotation vector has a normal isotropic distribution with a zero mean and mean square dispersion. In the roughness model it is assumed that the periodicity of the structure is undisturbed and the layers have an ideal crystal structure. The random profile of any interface is then characterised in the standard manner by a mean square roughness and a lateral correlation length. Further details of the theoretical derivation of the defect models can be found in the relevant published work [1,31]. From the model it follows that the observed influence of defects within a multilayer system, and associated broadening of the rocking curves, scales as a function of the square of the satellite diffraction order, $n$.

Fe/Au multilayers provide an ideal system with which to study this model due to the large number of diffraction orders observed in a typical $\theta/2\theta$ HXRD scan, see figure 7.9 a). Numerical simulations performed by Holý *et al.* show that, in the consideration of the defect model, the mosaic structure affects all of the satellite diffraction orders in the same way and does not lead to differences in the FWHM or shape of the peaks. Therefore, the interfacial roughness within a multilayer should be observable as a parabolic dependence of the FWHM of the peak on the satellite order, $n$, with a constant contribution to the FWHM coming from the mosaic defects within the system.

An example of two high angle rocking curves for the type A sample, (100) oriented grown on MgO, are shown in figure 7.24 a) and b). The FWHM of the rocking curves were determined from fitting to the Lorentzian squared line shape introduced by Gibaud [13].

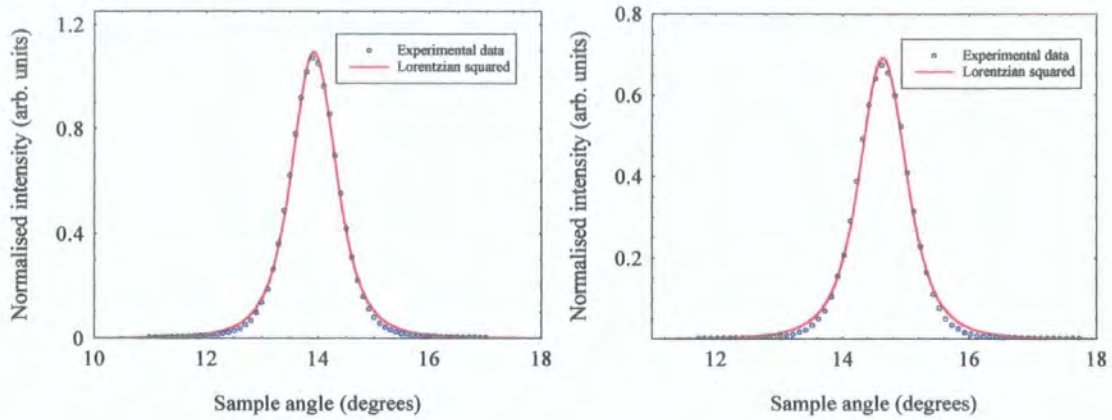


*Figure 7.24. High angle rocking curves at the a) n=-1 and b) n=0 diffraction orders with Lorentzian squared fits.*

The FWHM of the rocking curves as a function of satellite diffraction order, *n*, are shown in figure 7.25 and exhibit a clear parabolic dependence on the satellite order, as predicted by Holý's model.

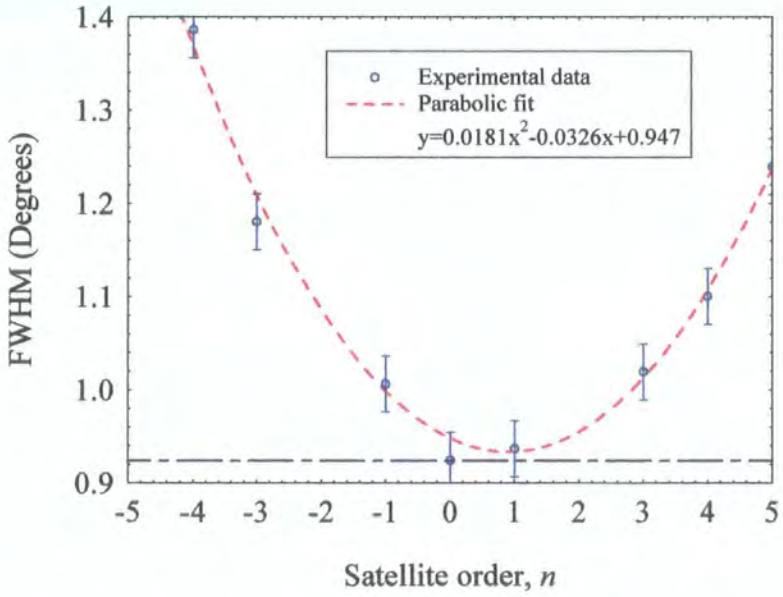


*Figure 7.25 FWHM of the satellite rocking curves as a function of satellite diffraction order, n.*

Although the minimum in the FWHM does occur at the zero order main diffraction maximum, the fit, while clearly parabolic, would appear to exhibit a $(n-1)^2$ dependence on satellite order. The origin of this slight asymmetry is unclear [32]. In the case of the main diffraction maximum, $n = 0$, the roughness has no influence on the diffraction and the multilayer would, in principal, behave as an ideal structure. The non-zero FWHM at the $n$=0 position is due to the constant contribution to the FWHM arising from the mosaic defects within this real system and is comparable with the surface diffraction peak widths. This is the first experimental verification of the ability to distinguish between different defect types in multilayers from a study of the shape of the main diffraction maximum and associated satellite orders in a typical multilayer diffraction scan. Interface roughness in Fe/Au grown on MgO produces a parabolic variation in the FWHM as a function of satellite order, as predicted in the model of Holý *et al.*, with a small, continuous contribution to the peak width from a certain degree of mosaic defects, also present in the multilayer. Even though the inclusion of defects within an ideal multilayer structure will alter the FWHM of the diffraction orders, the total integrated intensity of the diffraction orders is the same as for that of an ideal, defect free structure. The effect of interdiffusion within a multilayer is observed as a reduction in the integrated peak intensity with increasing satellite order, shown earlier in figure 7.10, again in agreement with the proposed model.

## 7.9 Summary and Conclusions

The main aim of this chapter has been to study and explain the distinct differences in the magneto-transport behaviour between (100) and (111) oriented, epitaxial Fe/Au multilayers. The enhanced GMR and saturation conductivity in the (100) oriented system cannot be explained from a structural standpoint. Grazing Incidence X-ray scattering measurements have shown the (100) multilayers to possess rougher interfaces than those in the (111) system, leading to a higher degree of spin-independent interface scattering and reduction in the electron mean free path in Fe/Au (100), not consistent with the enhanced conductivity and GMR. High Angle Diffraction measurements confirm that the sub-grain size in the (100) system is of the order of three times smaller than in the (111) multilayers, leading to a higher bulk defect density and scattering rate, again not consistent with the magneto-transport data. Grazing Incidence Surface Diffraction measurements show the Au layers to be of high crystalline

perfection in both the (100) and (111) oriented systems, with the Fe layers being of poor quality in each case. The structural evidence, when studied with the magneto-transport data, suggests the existence of a novel conducting mechanism in the (100) oriented multilayers, consistent with the electron channeling model proposed by Stiles *et al.* Within this model, one spin channel is confined within the spacer layer due to the large asymmetry in the reflection coefficients between polarisation states for electrons incident on the Au to Fe interface. Such a large asymmetry of the Fermi surface exists only in the (100) oriented system. As the spacer is of low resistance, one electron spin channel is preferentially confined within this low resistance shunt and the conductivity of the multilayer is enhanced greatly. The enhanced spin channel experiences approximately 3 times as many specular reflections at the interfaces defining the Au layer. When the multilayer conductivity is modified to include this channelling term the model is found to be in excellent agreement with the measured saturation conductivity.

Grazing Incidence Fluorescence measurements allow an elemental depth profile of a sample and provide evidence for the existence of Nb in the near surface region of the type D multilayers containing thicker Fe layers. Simulations show that the Nb is confined to a thin surface layer and may be behaving as a surfactant. There is no evidence for the presence of any Nb within the bulk of the layers. The exact mechanism by which the Nb is migrating through the multilayer is unclear and requires further investigation to establish whether the phenomenon is related to the substrate temperature or buffer thickness. However, the measurements do clearly indicate the presence of near surface Nb well away from the Nb buffer layer.

Finally, the defect model proposed by Holý *et al.* has been studied in relation to Fe/Au (100). The predicted parabolic variation in the FWHM of the satellite diffraction peaks as a function of satellite order due to roughness defects has been observed along with a mosaic defect contribution. The apparent $(n\text{-}1)^2$ dependence of the FWHM on satellite order, rather than the predicted $n^2$ variation requires further investigation. The reduction in the integrated intensity of satellite diffraction orders, compared to the ideal multilayer structure, due to interdiffusion within the multilayer has also been observed.

# References for Chapter 7


1. V.Holý, J.Kubena, E.Abramof, A.Pesek, E.Koppensteiner. J. Phys. D. 26 (1993) A146-A150

2. K. Shintaku, Y. Daitoh and T Shinjo, Phys. Rev. B 47, 14584 (1993)

3. M. Hayashi, T. Katayama, Y. Suzuki, M. Taninaka, A. Thiaville and W. Geerts, J. Magn. Magn. Mater. 126, 547 (1993)

4. N. Nakayama, T. Okuyama and T. Shinjo, J. Phys.: Cond. Matter **5**, 1173 (1993)

5. T. Okuyama, Jpn. J. Appl. Phys. 30, 2053 (1991)

6. O.S.Hernan, A.L.V. de Parga, J.M.Gallego, R.Miranda. Surface Science, Vol 415, No 1-2, p 106-121 (1998)

7. J. Xu, M.A. Howson, P. Hucknall, B.J. Hickey, R. Venkataraman, C. Hammond, M.J. Walker and D. Greig, J. Appl. Phys. 81, 3908 (1997)

8. T. Okuyama, Japn. J. Appl. Phys. 30, 2053 (1991)

9. P. Bruno and C. Chappert, Phys. Rev. Lett. 67, 1602 (1991)

10. M.D. Stiles, Phys. Rev. B 48, 7238 (1993)

11. M.Wormimgton, I.Pape, T.P.A.Hase, B.K.Tanner, D.K.Bowen. Phil. Mag. Lett. 74 211-216 (1996)

12. X-ray Diffraction in Crystals: Imperfect Crystals and Amorphous Bodies, A. Guinier, Dover Publications Ltd. New York. (1994)

13. A.Gibaud, R.A.Cowley, D.F.McMorrow, R.C.C.Ward, M.R.Wells. Phys. Rev. B. 48 (19) 14463-14471 (1993)

14. A.F. Mayadas and M. Shatzkes, Phys. Rev. B 1, 1382 (1970)

15. J.F. Bobo, B. Baylac, L. Hennet, O. Lenoble, M. Piecuch, B. Raquet and J.C. Ousset, J. Magn. Magn. Mater. 121, 291 (1993)

16. A.R. Modak, D.J. Smith and S.S.P. Parkin, Phys. Rev. B. 50, 4232 (1994)

17. W.E. Bailey, D. Guarisco and S.X. Wang, IEEE. Trans. Mag. 34, 957 (1998)

18. D.T.Dekadjevi *et al.*, in prep

19. M.D. Stiles, J. Appl. Phys. 79, 5805 (1996)

20. E.F.Egelhoff. IEEE Trans. Mag. 33, 3580 (1997)

21. H.J.M.Swagten, G.J.Strijkers, P.J.H.Bloemen, M.M.H.Willekens, W.J.M.Dejonge. Phys. Rev. B. 53, 9108 (1996)

22. Fuchs, Proc. Cambridge Phil. Soc. 34, 100 (1938)

23. P.A.Ryan, Ph.D Thesis, University of Leeds (1998)

24. M.Copel, M.C.Reuter, M.Horn von Hoegen, R.M.Tromp. Vol 42 No. 18 (1990)

25. M.Kamiko, R.Furukawa, K.Y.Kim, M.Iwanami, R.Yamamoto. J Magn. Magn. Mater. Vol199, p 716-718 (1999)

26. P.F.Fewster. J. Appl. Crystallogr. 22, 64 (1989)

27. P.F.Fewster. J. Appl. Crystallogr. 24, 178 (1991)

28. A.Appel, U.Bonce, J.L.Staudenmann. J. Phys. B. 81 371 (1990)

29. S.Koshiba, S.Nano, O.Tsuda, Y.Watanabe, Y.Sakurai, H.Kawata, M.Ando. J. Cryst. Growth. 95 51 (1989)

30. P.F.Fewster. J. Appl. Crystallogr. 21, 524 (1988)

31. E.Abramof, V.Holý, E.Koppensteiner, A.Pesek. J. Appl Phys 74 1736 (1993)

32. V. Holý, *(private communication)*

# Chapter 8

# Summary, Conclusions and Further Work

The physical processes underlying the Giant Magneto-Resistance (GMR) effect in magnetic multilayers, namely oscillatory exchange coupling, spin-dependent and spin-independent scattering, are widely believed to exhibit a strong dependence upon multilayer structure. The aim of the work presented in this thesis was to utilise x-ray scattering techniques in an attempt to determine the dominant structural factors, both interfacial and bulk, controlling the magnitude of the GMR in these systems.

The important role of the texture of a multilayer on the size of the GMR is evident in the work of chapter 5. It was found that the GMR in a series of Co/Cu multilayers, sputter deposited on etched silicon substrates, decreased dramatically with increasing etching voltage. Magnetic hysteresis and Neutron Reflectivity measurements, performed by D.E. Joyce, showed that this reduction was due to a reduction in the antiferromagnetic coupling fraction as the etching voltage increases. X-ray Reflectivity measurements show that the observed reduction in AF coupling across the series of samples can not be attributed to variations in the thickness of the non-magnetic spacer layer. The interface roughness was found to be highly correlated in nature and of the same amplitude, in-plane correlation length and fractal parameter in all samples, with no evidence of compositional grading. The variation in the GMR could not, therefore, be attributed to changes in the interfacial spin-independent scattering between the samples. Transmission Electron Microscopy measurements yield a grain size in good agreement with the lateral correlation length determined from simulation of the Transverse Diffuse Reflectivity data. X-ray Diffraction and Transmission Electron Diffraction measurements show the multilayer texture to change from a randomly oriented polycrystalline to a well oriented (111) polycrystalline texture with increasing etching voltage. It is most probable, therefore, that the loss of AF coupling is due to this change of texture and, more specifically, the reduction in the volume fraction of (100) oriented grains, with the substrate etching providing the correct interfacial energy match

to promote a strong (1 1 1) texture. The subsequent reduction in the GMR then originates from subsequent changes in the bulk spin-dependent scattering into the split *d*-band within the Co layers. Clearly, the effect of variations in the spin-independent scattering, associated with interface roughness, cannot be observed here as the interface morphology remains constant across the series of samples. The dependence of the GMR on both spin-independent scattering at the interface and texture related spin-dependent scattering within the bulk of the layers can be hard to distinguish as it is difficult to vary one without affecting the other. This difficulty in separating bulk and interface effects is also indicated by the degree of confusion in the literature as to the relative importance of interface scattering in multilayer systems. What is clear from this work is that the magnitude of the GMR is not simply dominated by roughness scattering. Appreciable differences in the GMR can arise due to a strong relationship between crystalline texture, the antiferromagnetic coupling fraction and the GMR.

The work of chapter 6 builds on the observation of the highly correlated interfaces of Co/Cu and looks at the way this conformality is retained with increasing bilayer number. Longitudinal and Transverse diffuse measurements show that the high degree of interface conformality is retained with increasing bilayer number, suggesting that if a limiting out-of-plane length scale for conformal growth does exist then it must be considerably greater that 300Å. Calculation of the magnetic bulk of the sample in conjunction with the layer thickness determined from the Specular Reflectivity suggests that the Co layer immediately adjacent to the substrate is rendered magnetically dead, most probably due to intermixing of the Co with native silicon and oxide layers. In contrast to the Co/Cu system, a noticeable reduction in the interface conformality is found in the Co/Pt system as the bilayer number is increased. A limiting out-of-plane length scale for conformal growth of approximately 360Å was found to exist, corresponding to 15 bilayer repeats. Torque magnetometry measurements show a noticeable reduction in perpendicular anisotropy for stack thicknesses in excess of this value. It would appear that the correlation of the roughness between successive layers is necessary for the magneto-static coupling that gives rise to the anisotropy, evident from an initial linear increase in anisotropy with layer number. Perpendicular anisotropy is then lost once the layer number exceeds the limit for continued conformal growth. Such a loss in conformality is consistent with a columnar type growth mode in Co/Pt, not present in Co/Cu. The origin of this growth mode lies in the different surface mobility,

upon deposition, of Co and Pt. Such observations are of importance with regard to high density magnetic recording media, in which perpendicular anisotropy is favoured.

A large proportion of the work in this thesis relates to the Fe/Au multilayer system. Fe/Au (100) and (111) multilayers grown, by MBE on thin buffer layers, were found to exhibit very different GMR and saturation conductivity characteristics. The GMR, measured by P.A. Ryan, in the Fe/Au (100) oscillates as function of the spacer thickness, due to the oscillations in the exchange coupling, with a period in good agreement with that calculated theoretically. However, the (111) oriented multilayers display no such oscillation, only a small, steady increase in GMR with increasing spacer thickness. Comparison of the GMR between the two orientations, for samples in which the antiferromagnetic coupling fraction was the same, yielded a GMR of 38% and 6% for the (100) and (111) oriented samples respectively. Further to this, the rate of increase in the saturation conductivity with Au spacer thickness was three times greater in the (100) oriented samples. X-ray scattering techniques were to prove crucial in understanding the origin of the observed differences in the magneto-transport behaviour between the two orientations. Reflectivity measurements show that the Au thickness was the same in each sample and that the GMR differences can not, therefore, be attributed to a loss of coupling due to differing spacer thickness. The thickness of the Fe layers was also found to be the same for each orientation. The interface roughness was found to be highly correlated in nature, with no compositional grading, in both systems but of considerably higher amplitude in the (100) multilayers exhibiting the enhanced GMR and conductivity. There were no measureable differences in the lateral correlation length or fractal parameter between the two systems. It was, therefore, not possible to attribute the differences in the magneto-transport behaviour to differences in the interface morphology. High Angle X-ray Diffraction measurements show the crystalline perfection of the layers to be excellent for both orientations with minimal strain and sharp, crystallographically abrupt interfaces. From measurement of the grain size, the bulk defect density and associated scattering was found to be considerably higher in the (100) oriented system, not consistent with the enhanced conductivity and GMR. Surface X-ray Diffraction measurements indicated that while the Au layers were of high in-plane quality the Fe layers were of poor quality in each case for equal thickness Fe. The absence of any structural interpretation for the difference in the magneto-transport behaviour between the two systems would suggest strongly the existence of a novel

conducting mechanism in the Fe/Au (100), consistent with electron channeling. With a channeling mechanism there is a large asymmetry in the reflection coefficients for an electron incident on the Au Fe interface between the two spin channels. One spin channel is confined within the low resistance Au spacer layer, due to the high reflection probability at the interface, which then effectively acts as a low resistance shunt, greatly enhancing the conductivity of the system. Again, the channeling effect exhibits a strong texture dependence as the asymmetry in the reflection coefficients exists only in the (100) oriented system. Simulations, performed by P.A. Ryan, of the conductivity for the two orientations are in excellent agreement with the experimental data when a channelling mode is assumed for the (100) system. This work is the first experimental observation of electron channeling in a multilayer system and is of obvious importance in terms of the enhancement to the conductivity and GMR that can be achieved with such a mechanism.

The FWHM of rocking curves taken through the zero and higher order diffraction peaks of an Fe/Au (100) High Angle Diffraction scan were found to follow a parabolic variation of rocking curve width as a function of satellite order. Such a parabolic variation is entirely consistent with that predicted from theoretical treatments of a proposed defect model. Although a minima occurs in the FWHM at the zero order position, the parabolic fit to the data is off-set towards the +1 satellite order. Further studies of more samples are required in order to clarify the whether the FWHM does indeed exhibit an $n^2$ or an $(n-1)^2$ dependence and whether a similar behaviour can be observed in Fe/Au(111). This is the first experimental observation of the proposed defect model and shows that it is possible to clearly distinguish between the effect of roughness and mosaic defect types.

Grazing Incidence X-ray Fluorescence measurements performed on Fe/Au (111) reveal a Nb yield for incident beam angles below the critical angle, with an additional enhancement at the critical angle itself. Such observations are consistent with the existence of a surface layer of Nb. Simulations show this to indeed be the case with a thin layer of Nb, of the order of 0.7Å, present at the multilayer surface. This can be understood in terms of the Nb buffer material acting as a surfactant in the growth of Fe/Au (111) on sapphire. This is an important observation as sapphire substrates with Nb buffers are standard substrates for the epitaxial growth of a wide range of

multilayers and the potential surfactant role of Nb in such systems is worthy of further investigation. The exact method by which the Nb moves through the multilayer is unclear and further work is planned to examine whether the surfactant effect is dependent on factors such as substrate temperature and buffer thickness.

In addition to the further work arising from the observations already discussed, there are other, closely related areas of interest that are ideally suited to x-ray scattering techniques.

The Co/Pd system is known to exhibit a large perpendicular anisotropy, similar to that found in Co/Pt. A study of Co/Pd, identical to that performed here for Co/Pt, will show whether the observed loss of anisotropy with increasing bilayer number in Co/Pt is unique to that system or is indeed a general feature of surface anisotropy. By preparing samples under varying sputtering conditions it should also be possible to investigate the effect of interface roughness and interdiffusion on the anisotropy.

Sputtered Co/Ru multilayers are known to exhibit strong antiferromagnetic exchange coupling, similar to that in Co/Cu. X-ray reflectivity studies could be used to probe the interface morphology in these systems in order to see how the interface roughness and conformality compares with that found for the Co/Cu system, with X-ray diffraction techniques being used to compare the texture between these two systems.

One of the most rapidly growing area of GMR research relates to spin valve systems. Hard X-ray Scattering techniques could be used to study the effect of the interface parameters on factors such as the exchange and switching fields in these systems. The developing field of Soft X-ray Scattering would then also provide a method with which to probe the magnetic roughness which could then be related to the structure. It has proved problematic in the past to study the NiFe/Cu layers and interfaces within often complex spin valve structures, through Specular and Diffuse reflectivity alone due to the poor scattering contrast. However, Fluorescence methods have proved a powerful technique with which to probe these structures by way of elemental depth profiling. Through continued synchrotron work and on-going development of the laboratory fluorescence equipment in Durham it should be possible to perform measurements to reveal the precision with which the Cu layer thickness can

be measured and whether it is possible to also study the interface width in these systems.

The ability to grow high quality, thin magnetic films on semiconductor substrates is becoming essential in the development of new technology. RHEED measurements performed recently by J.A.C. Bland's group at Cambridge suggests that under certain growth conditions it is possible to switch between b.c.c and f.c.c structures in Co layers of the order of nanometre thickness. Grazing Incidence Surface Diffraction measurements, similar to those performed on Fe/Au, should be able to follow and independently validate this structural change. Reflectivity measurements would also allow the effect of substrate roughness on this phase transition to be studied.

be measured and whether it is possible to also study the interface width in these systems.

The ability to grow high quality, thin magnetic films on semiconductor substrates is becoming essential in the development of new technology. RHEED measurements performed recently by J.A.C. Bland's group at Cambridge suggests that under certain growth conditions it is possible to switch between b.c.c and f.c.c structures in Co layers of the order of nanometre thickness. Grazing Incidence Surface Diffraction measurements, similar to those performed on Fe/Au, should be able to follow and independently validate this structural change. Reflectivity measurements would also allow the effect of substrate roughness on this phase transition to be studied.

# Appendix A

## Conversion between real and reciprocal space

The majority of the experimental data presented in this thesis is expressed in real space (arcseconds) with respect to sample and detector axes. This scan geometry can be converted to an equivalent reciprocal space notation via the following procedure:

$$\theta' = \frac{\theta}{3600} \qquad \phi' = \frac{\phi}{3600}$$

where $\theta$ and $\phi$, are the sample and detector angle in arcseconds, and $\theta'$ and $\phi'$ are the equivalent angles in degrees.

The reciprocal lattice vectors are then defined as:

$$q_x = \left(\frac{2}{\lambda}\right)\sin\left(\frac{\phi'}{2}\right)\sin\gamma \qquad \text{and} \qquad q_z = \left(\frac{2}{\lambda}\right)\sin\left(\frac{\phi'}{2}\right)\cos\gamma$$

where $\gamma = \theta' - \left(\frac{\phi'}{2}\right)$